POLITECNICO
MILANO 1863

SCUOLA DI INGEGNERIA INDUSTRIALE
E DELL'INFORMAZIONE

# Magneto-optical investigation of HZO/Co capacitors for electrical control of the magnetic state

Tesi di Laurea Magistrale in
Physics Engineering - Ingegneria Fisica

Author: **Edoardo Mugnano**

Student ID: 977163
Advisor: Prof. Matteo Cantoni
Co-advisors: Christian Rinaldi, Giovanni Gandini
Academic Year: 2023-24

# Abstract

This thesis work concerns the development, characterization, and optimization of a high sensitivity spatial micro-MOKE detection system, which allows performing magnetic characterizations of thin films and micro devices, and its application to a particular case, the magneto-electric coupling in capacitor-like devices based on the multiferroic composite heterostructure Co/HZO. The working operation of this setup is based on magneto-optical Kerr effect, which allows to map the magnetization of materials using polarized light. In research areas such as spintronics and magnetism, the study of magnetic properties is frequent in composite materials, either in the form of single layers or multilayers, whose properties manifest themselves near the surfaces or interfaces. In this context, this system makes it possible to carry out measurements with high surface sensitivity and high spatial resolution, such as to allow the study of magnetic phenomena at a microscopic level. The ability to focus the light with an objective allows the system to obtain a spatial resolution to 5 $\mu$m. The setup has a high versatility in characterizing magnetic samples with longitudinal and polar configurations, through the objective lens, whose axis can be shifted regarding the light beam direction. Furthermore, the use of a detector, whose signal acquisition method is based on an amplified differential system, gives to the system high sensitivity, such as to allow it to measure signals with a good signal-to-noise ratio without modulation of the light signal. Given the low invasiveness of light-based detection schemes, this system is well suited to being integrated with other characterization systems, for example electrical, to allow the study of magnetic phenomena coupled to other physical effects. This system was therefore used to study the magnetoelectric coupling effects between the magnetization and the electrical polarization of an artificial multiferroic heterostructure based on the composition of a ferroelectric material ($Hf_{0.5}Zr_{0.5}O_2$, HZO) and a ferromagnetic one (Co). HZO is a ferroelectric material that has attracted interest in the scientific community due to its compatibility with silicon-based device systems. The experiment was aimed at evaluating if and how the polarization of the HZO layer can influence the magnetic properties of the Co layer in micro-sized capacitor devices based on the Co/HZO heterostuctrure. The relevance of this experiment finds its motivations in a broader field of research on alternative systems to traditional CMOS-based

electronics, in particular in the field of memory devices, pointing to a low-dissipation and energy-saving new generation of devices, in the framework of so-called "green electronics".

**Keywords:** magneto-optical Kerr effect (MOKE), multiferroic, magneto-electric coupling, capacitor, device

# Abstract in lingua italiana

Questo lavoro di tesi riguarda lo sviluppo, la caratterizzazione e l'ottimizzazione di un sistema di rilevamento micro-MOKE ad elevata sensibilità spaziale, che consente di effettuare caratterizzazioni magnetiche di film sottili e dispositivi micrometrici, e la sua applicazione a un caso particolare, l'accoppiamento magneto-elettrico in capacitori di dimensioni micrometriche basati sull'eterostruttura composita multiferroica Co/HZO. Il funzionamento di questo setup si basa sull'effetto Kerr magneto-ottico, che consente di mappare la magnetizzazione dei materiali utilizzando la luce polarizzata. In ambiti di ricerca come la spintronica e il magnetismo, lo studio delle proprietà magnetiche è frequente nei materiali compositi, sia sotto forma di singoli strati e di multistrati, le cui proprietà si manifestano vicino alle superfici o alle interfacce. In questo contesto, questo sistema consente di effettuare misurazioni con elevata sensibilità superficiale e alta risoluzione spaziale, tale da permettere lo studio dei fenomeni magnetici a livello microscopico. La capacità di focalizzare la luce con un obiettivo consente al sistema di ottenere un risoluzione spaziale fino a 5 $\mu$m. Il setup ha una grande versatilità nella caratterizzazione di campioni magnetici con configurazioni longitudinali e polari, attraverso l'obiettivo, il cui asse può essere spostato rispetto alla direzione del fascio luminoso. Inoltre, l'uso di un fotodiodo, in grado di misurare ed amplificare un segnale differenziale, garantisce al sistema un'elevata sensibilità, tale da consentire di misurare segnali con un buon rapporto segnale-rumore senza modulazione del segnale luminoso. Data la bassa invasività dei sistemi di rilevamento basati sulla luce, questo sistema è ben adatto ad essere integrato con altri sistemi di misurazione, ad esempio elettrici, per consentire lo studio di fenomeni magnetici accoppiati ad altri fenomeni fisici. Questo sistema è stato quindi utilizzato per studiare gli effetti di accoppiamento magnetoelettrico tra la magnetizzazione e la polarizzazione elettrica di un'eterostruttura multiferroica artificiale all'interfacia tra un materiale ferroelettrico ($Hf_{0.5}Zr_{0.5}O_2$, HZO) e uno ferromagnetico (Co). HZO è un materiale ferroelettrico che ha attirato l'interesse della comunità scientifica per la sua compatibilità con i dispositivi basati su silicio. L'esperimento aveva lo scopo di valutare se e come la polarizzazione dello strato di HZO può influenzare le proprietà magnetiche dello strato di Co in dei capacitori di dimensioni micrometriche basati sull'eterostruttura Co/HZO. La rilevanza di

questo esperimento trova le sue motivazioni in un campo più ampio di ricerca su sistemi alternativi all'elettronica tradizionale basata su CMOS, in particolare nel campo dei dispositivi di memoria, puntando a una nuova generazione di dispositivi a bassa dissipazione e risparmio energetico, nell'ambito della cosiddetta "elettronica verde".

**Parole chiave:** effetto Kerr magneto-ottico, multiferroici, accoppiamento magneto-elettrico, capacitori, dispositivi

# Contents

# 1 | Introduction

## 1.1. Spintronics

Integrated circuits, which are at the heart of the computational revolution of the last century, have assumed a pervasive role in our modern every day's life, being the core of any electronic device ranging from vehicles, mobile smartphones to household applications. As a result, this industry has tremendously developed in one of the most economically relevant and competitive global markets. Since the 1960s, the core of these circuit devices was based on metal-oxide-semiconductor (MOS) transistor [45]. Over the decades, one of the most important parameters to benchmark the progresses of computing capability is the transistors produced per unit area. In 1965, Gordon Moore stated that the number of transistors on a chip was expected to double annually for at least ten years [54]. In fact, over the years, the chip transistor number has continued to increase, thanks to a continuous decrease of each transistor size and Gordon Moore's postulate became known as Moore's Law. Moreover, dimensional scaling of the transistor saw a parallel favorable scaling of the voltages and currents used, allowing the overall decrease in the power used [16]. However, already in the 90s, it became evident that transistor scaling was encountering several barriers such as power supply and threshold voltage, short-channel effect high-field effects, and interconnect delay [73]. As transistors and other components with nanoscale dimensions are built, though, processors and memories are becoming so dense that even their infinitesimal individual currents cause non-negligible overheat constraints [24]. As a result, the intrinsic limitations of CMOS stimulated the search for feasible alternatives, paving the way for the study of beyond-CMOS technologies [33, 57]. Among these, a particularly promising role is played by spintronics. Spintronics allows broadening the horizons of classical electronics, introducing the degree of freedom of the spin of electrons and its associated magnetic moment. This requires the ability to generate and manipulate spins through proper interactions with non-magnetic and ferromagnetic materials, as to inject or detect spin currents. In particular, nowadays, spin-based technologies have already been successfully commercialized in the field of magnetic memory storage, in which the order parameter of a magnetic region is used as a bit to store information.

Current spintronic applications, centered around magnetic storage and sensing, can be attributed to key advances in exploiting effects such as Anisotropic Magnetoresistance (AMR) [69], Giant Magnetoresistance (GMR) [12] and Tunneling Magnetoresistance (TMR) [53]. Historically, toggling the resistance states required a classical magnetic field, generated via currents through Biot Savart's law [50], as an intermediary. Writing data via magnetic field requires a significant level of current, which causes large power consumption in addition to complicated cell architecture [8]. The discoveries of the spin-transfer torque (STT) [68] and spin-orbital torque (SOT) [51] effects, which are based on the manipulation of magnetization through spin currents attributed to the exchange of angular momentum between the spins of the magnetic moment in a material and the free electrons passing through it, advanced spintronics-based memory devices over the past two decades, in terms of density, energy dissipation, and scalability, over the magnetic-assisted writing [10]. However, they still suffer in terms of energy efficiency, since the lowest switching energy via STT or SOT is limited to 10 fJ–100 fJ [6, 7], which is two orders of magnitude larger than each switch in complementary CMOS transistor (<1 fJ). Regarding CMOS, the quest for lower-power writing candidate using voltage rather than current to control magnetic properties [78] was spurred. A promising and attractive subfield in the framework of memory technology is the Magnetoelecric Coupling (ME) in multiferroic systems, where the ferromagnetism and the ferroelectricy phases are both present and can influence each other.

## 1.2. Magnetoelectric devices opportunities

The research on magnetoelectric coupling effects was revived by the renaissance of the multiferroic system in 2003 [70, 71], in which several ferroic orders, for instance, the ferroelectric (FE) and magnetic orders, coexist and couple together, thus generating the expectation of voltage of MRAM. People initially paid attention to the single-phase multiferroics in which electric field could modify magnetic properties via ME coupling in the same material. Unfortunately, most of these compounds show multiferroicity at cryogenic temperature [67], like Nickel-Iodine Boracite ($Ni_3B_7O_{13}I$) [11]. Some compounds show single-phase multiferroicity at room temperature, like BFO ($BiFeO_3$) [23], but their weak magnetization and polarization, causing a weak ME coupling, made them unusable for applications [43, 46, 67]. To overcome the limitations of these single-phase multiferroics, composite multiferroic materials have been developed [9]. So far, it has been recognized that artificial FM/FE composite multiferroic heterostructures are promising for applications due to the significant ME coupling at room temperature, as the AlN/FeCoSiB composite heterostructure studied by Ma *et al.* [46]. Several previous works demon-

strated the possibility of the magnetization control via an external applied voltage in artificial composite multiferroic systems [14, 79], e.g. $BaTiO_3$/CoFeB studied by Baldrati *et al* [13] at PoliFab at Politecnico di Milano. The use of composite multiferroics in modern computing devices offers the advantages of high storage density, low power consumption and large operation frequency [48]. Furthermore, the magnetic control of electrical properties through the ME effect is considered as the most energy efficiency avenue in nanoscale manipulation at room temperature with ultralow heat dissipation expected down to aJ [32]. For these reasons, ME memories based on composite multiferroic materials are one of the most probable candidates to achieve the voltage control of magnetization, which would allow obtaining the same advantages of non-volatility and the high processing speed of MRAMs based on STT or SOT, with a further significative reduction of power consumption and heat dissipation.

## 1.3. Hafnium zirconium oxide (HZO)

In this thesis work, we are interested investigating the presence of ME coupling in a composite multiferroic heterostructure made of Hafnium Zirconium Oxide $Hf_{0.5}Zr_{0.5}O_2$ (HZO) and Cobalt. Cobalt was chosen as a magnetic material due to its high magnetocrystalline anisotropy [52], at the core of many spintronics-memory devices [42, 60]. The ferroelectric material HZO is interesting for several reasons. The idea of using the ME effect in MF composite systems to electrically control the magnetization of a thin layer dates back some decades. Ferroelectric materials, in particular, perovskites ferroelectrics such as $Pb(Zr,Ti)O_3$ (PZT), $BaTiO_3$ (BTO), and $SrBi_2Ta_2O_9$ have been widely studied in the past for such a scope. The measurements made by Baldrati *et al* [13] at Politecnico di Milano showed in a $BaTiO_3$/CoFeB composite multiferroic system the possibility of controlling the CoFeB coercivity by an external applied voltage to BTO. However, perovskite-base memory devices never materialized due to the challenges with modern complementary metal oxide semiconductor (CMOS) technology, having to face complex issues such as etching, hydrogen sensitivity, thickness, and scaling beyond the 100 nm technology node [39], leaving them as a research topic only [20, 40]. HZO, which is a $HfO_2$-based material, aroused great interest because of its good compatibility with silicon CMOS technology and its robust ferroelectricity even at extremely thin ($< 10$ nm) thicknesses. Furthermore, by showing lower leakage currents and larger breakdown electric fields, HZO resistance can be improved to the performance of more traditional perovskite oxides [22]. These reasons justify the growing interest in HZO, which has already become one of the most attractive ferroelectric materials in a wide range of applications such as ferroelectric random-access memory, ferroelectric field-effect transistors and ferroelectric

tunneling junctions [20, 40].

## 1.4. Magnetic characterizations

The system studied in this thesis is a composite multiferroic heterostructure based on two interfaced Co and HZO layers. The Co/HZO systems object of investigation of this thesis are based on the material stacks shown in the table 1.1. The stacks of the samples were fabricated in collaboration with the Fraunhofer-Gesellschaft Institute in Germany. Like the study *et al* [13] for the $BaTiO_3$/CoFeB system, we are again interested in evaluating the magnetoelectric coupling effects between the cobalt magnetization and the HZO electrical polarization. These investigations will contribute to the characterization of HZO and this multiferroic system to develop memory devices based on magnetoelectric coupling, which have attracted high interest from the scientific community.

| Sample | Stack |
|---|---|
| **C10** | Pt(5)/TiN(10)/HZO(10)/Co(10)/p-Si |
| **C3** | Pt(5)/TiN(10)/HZO(10)/Co(3)/p-Si |
| **C1** | Pt(5)/TiN(10)/HZO(10)/Co(1)/p-Si |

Table 1.1: Fraunhofer-Gesellschaft Institute samples.

### 1.4.1. MOKE

To study magnetoelectric coupling effects in the Co/HZO system, it is necessary to perform electrical and magnetic characterizations simultaneously. This thesis work concerned the development, characterization, and optimization of a highly sensitive micro-MOKE (which will be called from now $\mu$MOKE, where $\mu$ is the Greek letter used to refer to the order of magnitude of the micrometer) spatial sensing system, which can be used for this purpose. This detection system has been realized at the NaBiS (NanoBiotechnology and Spintronics) group of PoliFab center of Politecnico di Milano.

There are different measurement techniques to characterize a magnetic material. Among the most common, we mention:

- vibrating sample magnetometers (VSM) [30], based on the Faraday induction law. VSM measurements are often done to evaluate the magnetic moment of materials;
- superconducting quantum interference devices (SQUID) [66], based on the Joseph-

son effect. SQUID devices are also used to evaluate the magnetic moment of materials. As regards VSM techniques, SQUID allows measurements to be carried out with greater sensitivity.

However, those techniques have two drawbacks:

- they are sensitive to the whole volume of the sample and do not allow for a local investigation of micro devices;
- their sensibility to external stimuli (voltage, current, heat, strain...) does not allow characterizations on samples which require the application of voltages and currents.

For these reasons, VSM and SQUID detection systems are not suitable to study ME effects in the Co/HZO system and devices, which would require the application of voltages to control the HZO polarization state.

These limitations can be resolved using a magnetic optical sensing system based on the magneto-optical Kerr effect (MOKE), which magnetic characterization by light is not affected by the voltages applied on the sample. Moreover, MOKE systems, with respect to VSM and SQUID systems, present the following advantages:

- MOKE systems are characterized by high surface sensitivity, which is well suited to the characterization of the Co/HZO system, whose properties manifest themselves near the surfaces;
- exploiting the ability to focus light through an objective, it is possible to increase the spatial resolution of the measurement, regarding the magnetic region size, giving the possibility to perform local magnetic characterizations, which is important for us to characterize microdevices;

In the context of measurements on the magnetoelectric coupling of Co/HZO, the $\mu$MOKE system we developed presents the following characteristics:

- **High magnetic sensitivity**: to improve the quality of the magnetic signal, the laser light is detected by a balanced photodiode, which operation is based on a differential light acquisition system, capable to reject most of the noise and disturbances affecting the light signal;
- **High spatial resolution**: when working with a 100x objective, the setup spatial resolution can be improved down to 5 $\mu$m;
- **Magnetic characterizations versability**: exploiting the ability to focus light through an objective, the setup is able to perform both longitudinal and polar

magnetic characterizations. That is an important feature because micromagnetic systems, due to their reduced size and/or due to interfaces effects, could present at the same time in-plane and out-of-plane magnetization components.

## 1.5. Thesis outlook

A primary experimental work was devoted to the development of a $\mu$MOKE system able to perform magnetic characterizations of the samples and devices. Finally, this MOKE setup was applied to the study of the ME coupling in the Co/HZO system. To study the ME coupling effects, the experimental work has been divided into the three following activities:

- **Thin film magnetic characterizations**: as a starting point, the research focused on the study of the magnetic properties and the characterization of the in-plane and out-of-plane magnetic anisotropies in Co/HZO films. Since the ME coupling can strongly depend on the magnetic anisotropy of the magnetic sample, a preliminary investigation would help us to identify the Co/HZO sample stack with the magnetic characteristics that would enhance the ME coupling interactions;
- **Fabrication and characterizations of the devices**: aiming to study the ME coupling on a micro device system, based on the results of the Co/HZO thin films magnetic characterizations, we moved on the fabrication of Co/HZO micro capacitors, which were then characterized both magnetically and ferroelectrically;
- **Magnetoelectric coupling experiment**: we investigated the presence of the ME coupling in the Co/HZO microcapacitor system via magneto-optical measurements through a spatial $\mu$MOKE system we developed, applying an electric field to polarize the device.

Based on these experimental activities, the thesis work that is presented has been structured in the following chapters:

- **Chapter 2: "Ferromagnetism and Ferroelectricity"**, a theoretical overview of ferromagnetism and ferroelectricity at the base of our work is given;
- **Chapter 3: "Interaction of light with magnetic systems"**, the theory behind the magneto-optical Kerr effects at the core of light-based magnetization measurements is given;
- **Chapter 4: "Magnetic and ferroelectric detection techniques for thin films"**, this chapter describes the experimental methods we used to characterize

the magnetization and the ferroelectricity of the Co/HZO thin films;

- **Chapter 5: "Co/HZO magnetic thin film characterizations"**, the results on the magnetic characterizations on cobalt thin films are presented;
- **Chapter 6: "$\mu$MOKE characterizations"**, we present the development and the performance characterizations of the spatial $\mu$MOKE system, at the core of this experimental thesis;
- **Chapter 7: "Co/HZO microcapacitor characterizations"**: this chapeter is dedicated to the ferroelectric and magnetoelectric characterizations of the Co/HZO microcapacitor devices;
- **Chapter 8: "Conclusions"**: the conclusions of this work are summarized together with the future perspectives.

# 2 | Ferromagnetism and ferroelectricity

Ferromagnetism is a property of certain materials, such as cobalt, that allows the material to form a permanent magnet. The properties of ferromagnetic materials result from several physical phenomena, that together contribute to their magnetic configuration. In this first section of this chapter, we will introduce the basic principles of the theory of micromagnetism, which allows understanding the different magnetic energy contributions that compete to determine the most favorable magnetic configuration of a given material. In particular, we will focus on the phenomena that are responsible for the rise of perpendicular magnetic anisotropy in thin films.

Ferroelectric materials exhibit a spontaneous electric polarization that shows a hysteretic behavior as a function of an applied external electric field. Ferroelectricity is connected to the structural properties of a material and not to an intrinsic property of an atom, as in the case of ferromagnetism. In the second section of this chapter, we provide an overview of ferroelectricity and its physical origin and describes the structural and ferroelectric properties of Hafnium–Zirconium Oxide (HZO). Finally, the third section is dedicated to the coupling between the two ferroic orders of ferromagnetism and ferroelectricity, called magnetoelectric coupling.

## 2.1. Fundamentals of Micromagnetism

Micromagnetism is the framework used to study magnetization phenomena on the intermediate scale between the quantum mechanical scale of individual atoms and the macroscale [18]. It studies thermodynamically how a magnetic system evolves towards the most stable configuration given initial boundary conditions. It can be shown that the equilibrium is reached by irreversible transformations that minimize the Landau free energy $G_L$ $[J]$ (2.1):

$$G_L = F - \mu_0 \int_V \mathbf{M} \cdot \mathbf{H}_a d\tau \tag{2.1}$$

$$F = U - TS \tag{2.2}$$

where F $[J]$ is the free Helmoltz energy (2.2), $\mu_0$ $[H/m]$ is the vacuum magnetic permeability constant and $U$ $[J]$, $T$ $[K]$, $S$ $[J/K]$ are respectively the internal energy, the temperature and the entropy of the magnetic system. The second term of the equation (2.1) is the Zeeman energy term, which describes the energy interaction between a system with volume $V$ $[m^3]$ provided by a magnetization $\mathbf{M}$ $[A/m]$ and an external magnetic H-field $\mathbf{H}_a$ $[A/m]$. To make our model and calculations easier we will neglect the entropy term of the equation (2.2) by setting $T = 0$ $K$. In the following sections, we will describe the most relevant magnetic energy terms, and anisotropy features, which define the total magnetic energy $U$ of a magnetic system.

### 2.1.1. Exchange interaction

The exchange interaction is a quantum mechanical effect that arises from the Coulomb repulsion and the fermionic antisymmetric nature of the total wave function of two nearby electrons, usually on neighbouring atoms. This interaction is ruled by an energy term, called exchange integral $J$ $[J]$, that in the simplest case of a hydrogen molecule is defined as the energy difference between the singlet and triplet electronic states. Depending on the sign of $J$, the exchange interaction favors the parallel (ferromagnetic, $J > 0$) or antiparallel (antiferromagnetic, $J < 0$) orientation of spins along interatomic distances. The hamiltonian that describes the exchange interaction contribution to the magnetic properties of a magnetic system based on $3d$ transition metal elements, such as cobalt, is given by the equation (2.3) [15]:

$$\hat{H}_{ex} = -\sum_{i \neq j=1}^{N} J_{i,j} \hat{\mathbf{S}}_i \cdot \hat{\mathbf{S}}_j \tag{2.3}$$

where the $\hat{\mathbf{S}}_i$, $\hat{\mathbf{S}}_j$ are the spin moments in the i-th and j-th atomic sites of the system and $J_{i,j}$ their exchange interaction. As we already pointed out, if $J_{i,j} > 0$, $\forall\, i \neq j$, the magnetic dipoles will minimize the energy of the system by defining a magnetic configuration in which they are all parallel. However, the presence in a magnetic system of impurity elements, defects and anisotropy fields can induce small tilting configurations for the

spin dipoles. The tilting between spins can be appreciated over a distance that is called exchange length $l_{ex}$ $[m]$. By definition the exchange length $l_{ex}$ is the shorter length scale, usually units of nanometers, over which the magnetization can be twisted if we consider only exchange and magnetostatic energy. The tilting between first neighbors spin dipoles cannot be too high since that would imply a very important increase of the exchange energy (2.3). If the magnetic system locally present titling of the spin dipoles then the exchange energy term $U_{ex}$ $[J]$ that will give contribution to the Landau free energy (2.1) is described by the equation (2.4) [5]:

$$U_{ex} = \frac{A}{2} \int_V [(\nabla m_x)^2 + (\nabla m_y)^2 + (\nabla m_z)^2] d\tau \tag{2.4}$$

where $A$ $[J/m]$ is called the exchange stiffness parameter and $m_x$, $m_y$, $m_z$ are the components of the unit vector of $\mathbf{M}$. $A$ is related to the exchange interaction of the material that defines the system. We notice that the equation (2.4) is different from zero only if we have $\nabla m_i \neq 0$ for at least one $i = x$, $y$, $z$, which implies that there has to be a local tilting of the magnetization.

### 2.1.2. Magnetic anisotropy

In general, we say that a system is characterized by a magnetic anisotropy whenever we can identify a preferential direction along which, if $\mathbf{M}$ results parallel to it, the total energy gets minimized. The magnetization directions along which the energy of the system is minimized (maximized) are called easy axes (hard axes). If we call $f_k$ $[J/m^3]$ the anisotropy energy density, the anisotropy energy contribution $U_k$ $[J]$ to the Landau free energy (2.1) is described by the equation (2.5):

$$U_k = \int_V f_k(\mathbf{M}, \mathbf{n}(\mathbf{r})) d\tau \tag{2.5}$$

where $\mathbf{n}(\mathbf{r})$ vector in equation (2.5) describes the direction of an anisotropic axis of the system. The $f_k$ term in general depends on the characteristics of the atomic elements that form the magnetic system and how they interact when living inside of a crystal lattice environment. The easiest kind of anisotropy is represented by the uniaxial anisotropy, which means that there will be a single preferential axis for the magnetization $\mathbf{M}$ to get oriented with. Considering the reference system shown in the figure 2.1, the $f_{an}$ term for a system with an uniaxial anisotropy, along the $z$ axis, can be described by the relation (2.6):

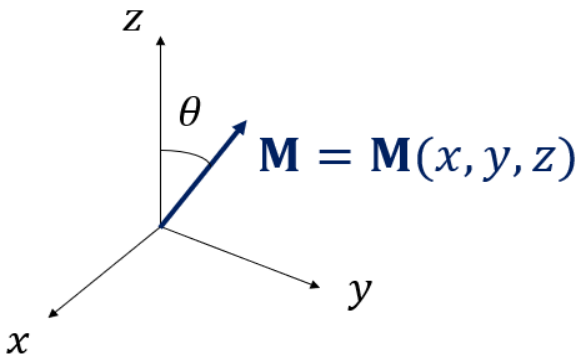


Figure 2.1: Reference system for an uniaxial anisotropy magnetic system with magnetization **M** and the $z$ direction as the easy axis.

$$f_{an}(\theta) \simeq K_0 + K_1 sin^2(\theta) \tag{2.6}$$

where $\theta$ is the angle subtended between the magnetization **M** and the anisotropy $z$ axis. $K_1$ $[J/m^3]$ is the uniaxial anisotropy energy density, which depends on the characteristics of the material. $K_0$ is a constant energy contribution, which can be neglected since it has no influence on the determination of the $\theta$ which minimizes (2.6), which then minimizes the relation (2.5). If $K_1 > 0$, the minima for are found for $\theta = 0, \pi$, meaning that the magnetic system will prefer to align **M** along a defined direction. This is what we call easy-axis anisotropy, as shown in figure 2.2a [82]. Instead, if $K_1 < 0$, the minima for are found for $\theta = \pm\pi/2$, causing the system to orientate **M** over a defined plane. Then, we talk about easy-plane anisotropy, as depicted in figure 2.2b. The two main sources of magnetic anisotropies are spin-orbit and magnetic dipolar interactions [34]. The first is the main responsible for bulk and surface crystalline anisotropies, while the second for the so-called shape anisotropy. Each of these anisotropies, respectively, will be discussed in the subsections 2.1.3, 2.1.5 and 2.1.4.

### 2.1.3. Magnetocrystalline anisotropy

As we already pointed out in section 2.1.1, the origin of magnetism in a crystal system is related to the exchange interaction between the total spin dipoles belonging to the different magnetic ions, which, for a transition element such as cobalt, are determined by the exchange interaction between the $3d$ core electrons. Since each ion is not living isolated but is embedded in a crystal, the crystalline environment significantly affects its properties. In fact, each ion experiences the crystal field, which is the static electric field produced by the charge distribution of the surrounding ions. As a consequence, the symmetry of the

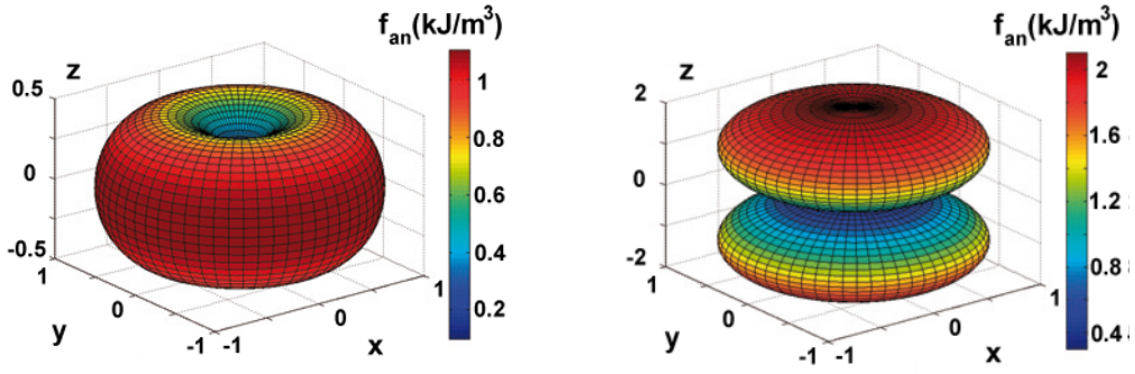


(a) Easy perpendicular direction along $z$ with $K_1 = 1\ kJ/m^3$.

(b) Easy plane ($xy$ plane) with $K_1 = -0.9\ kJ/m^3$.

Figure 2.2: Uniaxial anisotropies represented by energy surfaces. The length of the plotted radial component is proportional to the energy density for that direction. The anisotropy constants are chosen to illustrate different cases at similar energy scales [82].

crystal is reflected in the properties of the crystal field. The crystal field is responsible for the breaking of degeneracies of outer electron $3d$ orbital states. The strong coupling between the lattice field and the orbital moments leads to new electronic configurations, which spatial distribution will be mostly localized along the crystal symmetry directions. This crystal-field interaction tends to stabilize a particular orbital, and by spin-orbit interaction the total spin dipole of the magnetic ion is finally aligned along a particular crystallographic direction. This kind of magnetocrystalline anisotropy is known as *single-ion anisotropy*. An example of bulk magnetocrystalline anisotropy is the cubic anisotropy, which causes $\mathbf{M}$ orientating along the symmetry crystal direction of a cube.

### 2.1.4. Demagnetizing energy and shape anisotropy

The geometrical shape of a magnetic system also has a significant active role in determining the equilibrium magnetic configuration of the system. If we were considering magnetostatic interactions only, it would be more convenient for the magnetic system to orientate $\mathbf{M}$ parallel to the directions along which the system is more elongated. The energy contribution due to shape anisotropy $U_M$ $[J]$, also known as demagnetizing energy, that gives contribution to the Landau free energy (2.1) is described by the equation (2.7):

$$U_M = -\frac{\mu_0}{2}\int_V \mathbf{M}\cdot\mathbf{H}_M d\tau \tag{2.7}$$

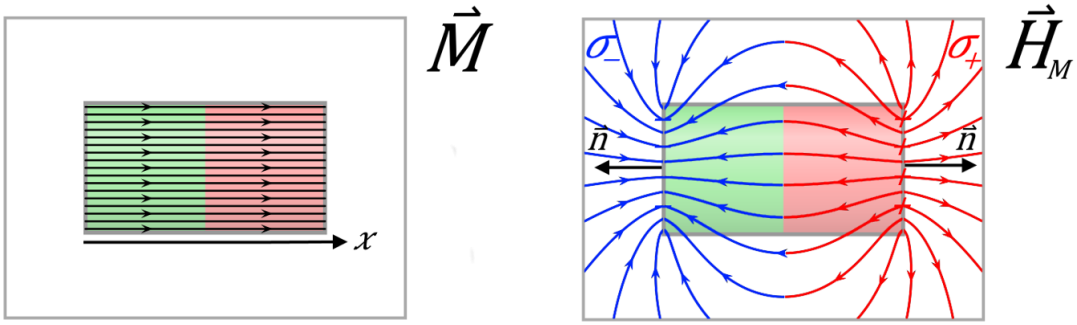


(a) Magnetization field $\mathbf{M}$. (b) Stray field $\mathbf{H}_M$.

Figure 2.3: 2D rectangular magnetic system with uniform magnetization $\mathbf{M}$ along the $x$ axis.

where $\mathbf{H}_M$ $[A/m]$ in the equation (2.7) is the demagnetizing field, which is the magnetic $H$-field generated by the magnetization in the magnetic system. The $\mathbf{H}_M$ field is also called the stray field when we refer to the magnetic field distribution that a magnet, with a magnetization $\mathbf{M}$, generates outside of the magnet. Working in a magnetostatic regime, $\mathbf{H}_M$ can be understood with the concept of magnetostatic charges. The mathematical formalism behind the concept of the magnetostatic charges is very helpful to define the magnetostatic properties of a magnetic system, even though no magnetic charges do actually exist since no single magnetic pole has ever been found so far. Given a system with a magnetization $\mathbf{M}$ we can define the volume $\sigma_V$ $[A/m^2]$ and surface magnetostatic charges and $\sigma_S$ $[A/m]$ with the relations (2.8) and (2.9):

$$\sigma_V = \nabla \cdot \mathbf{M} \tag{2.8}$$

$$\sigma_S = \mathbf{M} \cdot \mathbf{n} \tag{2.9}$$

where $\mathbf{n}$ in equation (2.9) is the normal to a local surface of the magnetic system. An example of the application of magnetostatic charges is shown in the picture 2.3. The magnetic system in the figure 2.3a is a system with uniform magnetization $\mathbf{M}$, so it is already possible to say that no volume magnetostatic charges are present: $\sigma_V = \nabla \cdot \mathbf{M} = 0$. We will find surface magnetostatic charges only along the system surfaces with normals $\mathbf{n}$ parallel to $\mathbf{M}$, such that $\sigma_S = \mathbf{M} \cdot \mathbf{n} \neq 0$. Respectively, we will have positive and negative surface magnetostatic charges $\sigma_+$ and $\sigma_-$ on the right and left lateral surfaces. The magnetic field generated by $\sigma_+$ and $\sigma_-$, pointing from positive to negative, is what we have called $\mathbf{H}_M$, as shown in the figure 2.3b. In general, the demagnetizing field $\mathbf{H}_M$ is always

opposite with respect to the magnetization **M**. In the case of an ellipsoidal ferromagnet, the demagnetizing field $\mathbf{H}_M$ is uniform and can be expressed by the expression (2.10):

$$\mathbf{H}_M = -\mathbf{N} \cdot \mathbf{M} \tag{2.10}$$

where **N** is the shape-dependent demagnetizing tensor. If **M** lies along one of the principal axes of the ellipse, the tensor can be diagonalized and written by the relation (2.11):

$$\mathbf{N} = \begin{pmatrix} N_x & 0 & 0 \\ 0 & N_y & 0 \\ 0 & 0 & N_z \end{pmatrix} \tag{2.11}$$

where $N_i \leq 1$ for $i = x, y, z$ such that $Tr(\mathbf{N}) = 1$. The magnetic system we are interested are thin films, which can be seen as oblate spheroids with two axis, along $x$ and $y$ equal to each other, and the $z$ axis much smaller than the first two. In this case, the tensor elements of (2.11) are such that $N_x = N_y \ll 1$, and, since $Tr(\mathbf{N}) = 1$ must be verified, $N_z = 1$. By considering these approximations to evaluate the relations (2.10) and (2.7), the demagnetizing energy $U_M$ per unit volume can be written by the expression (2.12):

$$E_M = \frac{U_M}{V} = \frac{\mu_0}{2}(N_z - N_x)M_s^2 \cos^2\theta \simeq \frac{1}{2}\mu_0 M_s^2 \cos^2\theta \tag{2.12}$$

where $\theta$ is the angle between **M** and the film norm vector **n**. Since we are describing a thin film, we considered $N_z - N_x \simeq 1$. The demagnetizing energy per unit volume (2.12) is minimized when $\cos^2\theta$ is minimum, that is for $\theta = \pm\pi/2$. For a thin film, we have an easy-plane along the thin film plane itself and a hard-axis along the direction perpendicular to it. From these considerations, it appears that generally, in a thin film, the shape anisotropy forces the magnetization to lie on the plane of the thin film, rather than perpendicular to it. However, in some multilayer thin film systems exploiting interfaces effects, such perpendicular magnetic anisotropy (as shown in the subsection 2.1.5), it is also possible to induce an out of plane easy-axis configuration.

### 2.1.5. Perpendicular magnetic anisotropy

As individual layers in a multilayer stack become thinner, the role of interfaces and surfaces may dominate that of the bulk. In such systems, interface contributions can rotate the easy magnetization direction from a parallel to a perpendicular configuration regarding the film plane. This kind of interface anisotropy, which is known as *perpendicular magnetic*

*anisotropy* (PMA), is still the result of a magnetocrystalline anisotropy at the interface which considerably differs from the one in the bulk. This kind of interface anisotropy was predicted already in 1954 by Néel [58] as a result of the lowered symmetry at the surface or interface between different magnetic layers. Being an interfacial effect, the PMA shows a clear dependence on the thickness of the ferromagnetic material. As the FM layer becomes thinner, the anisotropy constant $K_1$ (see equation 2.6) changes from positive values (in-plane anisotropy) to negative values (out-of-plane anisotropy). The origin of the PMA between a ferromagnetic metal and an oxide, as Fe/MgO, is to be related to the hybridization process of Fe $3d$ and O $2p$ orbitals, which occurs just at the interface between the two layers [85]. The PMA in a multi thin layer system can be induced by, e.g., controlling the growth parameters during the deposition process of the magnetic material, or using post-deposition techniques, such as thermal anneal, to favor the arrangement of atoms at the interface to maximize the surface magnetocrystalline anisotropy effects [63].

## 2.2. Ferroelectricity

Ferroelectrics belong to a special class of materials that exhibit a spontaneous electric polarization. This ferroelectric polarization presents a hysteretic behavior, and it can be reversed by a sufficiently large external electric field [62], similarly to what occurs in ferromagnetic materials when an external magnetic field is applied. Moreover, as ferromagnets, ferroelectric materials become paraelectric above a critical temperature, called Curie temperature $T_C$, which causes them to lose their spontaneous polarization. However, unlike ferromagnetism, ferroelectricity is not caused by the intrinsic properties of an atom, but it is connected to the structural properties of the material. The simplest ferroelectric crystals are the displacive ones, in which the displacements of the ions, constituting the crystal unit cell, causes the generation of a finite electric polarization. Displacive ferroelectrics usually display a coupling between polarization and strain. As piezoelectric materials, they generate an electric field in response to an applied stress and viceversa. The polarization of a piezoelectric material can be written by the expression (2.13):

$$P = E\chi + Zd \tag{2.13}$$

where $Z$ is the stress, $d$ is the piezoelectric constant, $E$ is the electric field and $\chi$ is the dielectric susceptibility. In the following subsections, we present a brief description of the physics behind ferroelectricity and the ferroelectric material investigated in this thesis, which is Hafnium Zirconium Oxide (HZO).

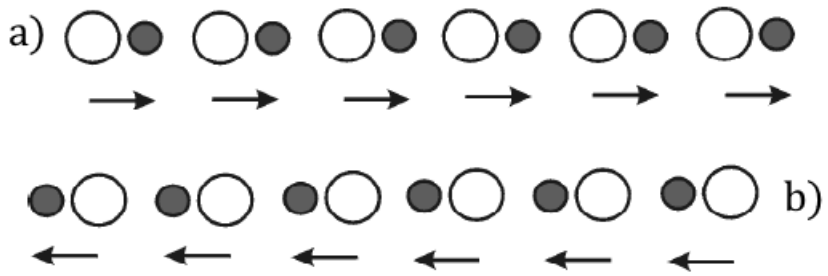


Figure 2.4: One-dimensional crystal made up of two atoms of opposite charge, which can orient the dipoles to point all to the right (a), or all to the left (b). The two structures are completely equivalent, except that they have an opposite sign to the dipole moment. They must therefore have exactly the same energy.

### 2.2.1. Fundamentals of ferroelectricity

Ferroelectrics materials are characterized by a non-zero dielectric polarization which can be described by the equation (2.14):

$$\mathbf{p} = \frac{\sum_i Q_i \mathbf{R}_i}{V} \tag{2.14}$$

where $Q_i$ and $\mathbf{R}_i$ are the charge and the position of the $i$-th atom in the crystal system with volume $V$. From this equation, it is apparent that ferroelectricity is prohibited in crystals that have a center of symmetry. If we consider a one dimensional chain of atoms with opposite charges (as sketched in the figure 2.4), the two different atomic configurations with dipoles oriented to the left and to the right are energetically equivalent. Supposing these are stable configuration, the free energy has two minima separated by a potential barrier $\Delta U$, showed in figure 2.5a. If thermal energy is much lower than $\Delta U$, the system can be found only in one of the two configurations. The application of an electric field allows switching from one configuration to another because it leads to an imbalance of the potential wells, to the polarization reversal and to a hysterestic behavior, as displayed in the figure 2.5b.

### 2.2.2. Hafnium zirconium oxide

Hafnium zirconium oxide $Hf_{0.5}Zr_{0.5}O_2$ (HZO) is a material which ferroelectric behavior is determined at room temperature by its orthorhombic crystalline phase, which structure has been shown in figure 2.6. In this crystalline phase, the polarization vector is aligned to the elongated $c$ axis. The orthorombic phase can be obtained after a mixing of the

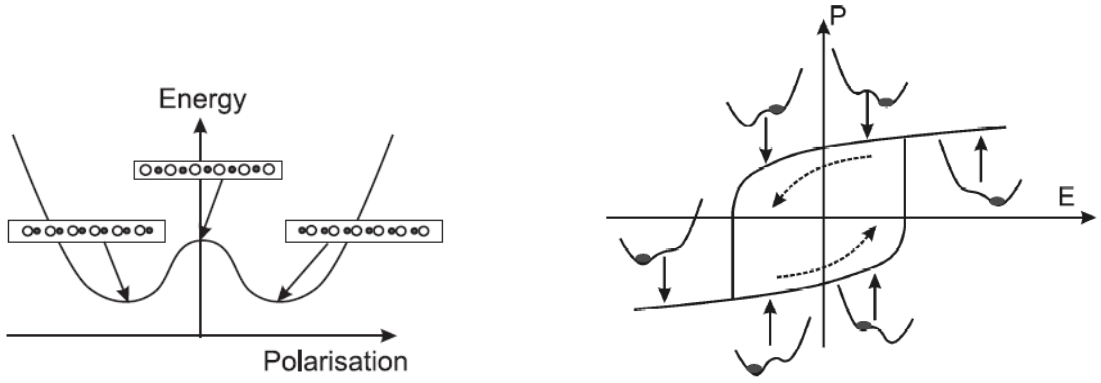


(a) (b)

Figure 2.5: (a) Schematic potential well as a function of the polarization. (b) Schematic picture of hysteresis in an idealized ferroelectric as a function of the electric field.

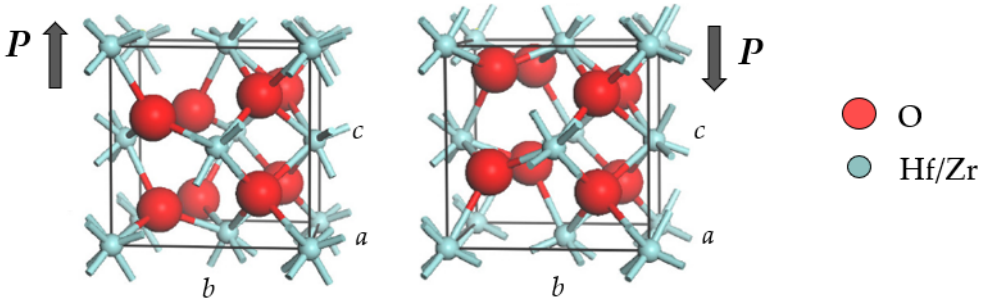


Figure 2.6: HZO othorombic phase structures with polarization **P** up (left) and down (right) parallel the $c$ crystal axis.

two transition metal oxides $ZrO_2$ and $HfO_2$, as pointed out by Muller *et al.* in the work [55]. In fact, the Polarization - Voltage (PV) curves in the picture 2.7 suggest that the ferroelectric response is maximized if the Hf and Zr stoichiometry coefficients are the same.

### 2.2.3. Magnetoelecric coupling

In general, the magneto electric (ME) coupling effect describes the coupling between electric and magnetic fields in matter, such as the induction of magnetization $M$ by an external electric field $E$ or viceversa a polarization $P$ generated by a magnetic field $H$ [81]. Thermodynamically, the ME effect in single-phase crystals can be understood within the Landau theory framework for a magnetoelectric system [29], approached by the expansion

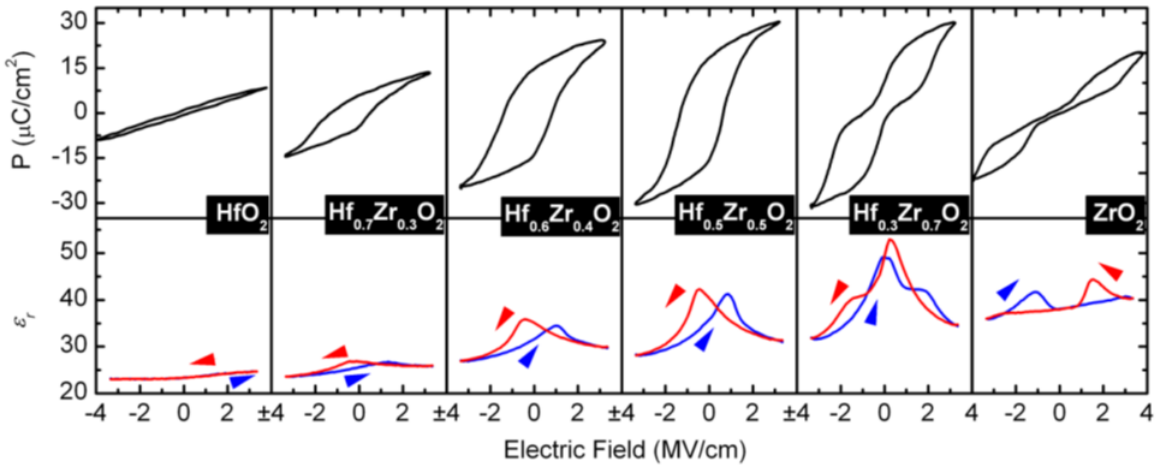


Figure 2.7: E-P hysteresis at 1 kHz and small signal CV hysteresis at 10 kHz (50 mV level) of 9 nm thin Hf$O_2$-Zr$O_2$ based metal-insulator/metal capacitors at room temperature. An evolution from paraelectric Hf$O_2$ to ferroelectric Hf$O_2$-Zr$O_2$ to an antiferroelectric-like behavior in Zr$O_2$ can be observed in PV as well as in CV characteristics [55].

of free energy 2.15 with the $F_{ME}$ magnetocoupling energy contributions 2.16:

$$F(\mathbf{E},\mathbf{H}) = F_0 - P_i^s E_i - M_i^s - \frac{1}{2}\epsilon_0\epsilon_{ij}E_iEj - \frac{1}{2}\mu_0\mu_{ij}H_iHj + F_{ME}(\mathbf{E},\mathbf{H}) \tag{2.15}$$

$$F_{ME}(\mathbf{E},\mathbf{H}) = -\alpha_{ij}E_iH_j - \frac{1}{2}\beta ijkE_iH_jH_k - \frac{1}{2}\gamma ijkH_iE_jE_k + ... \tag{2.16}$$

where $F_0$ is the ground state free energy; the $i$, $j$ and $k$ indexes refer to the three components of a variable in spatial coordinates; $E_i$ and $H_i$ the components of the electric field $\mathbf{E}$ and magnetic field $\mathbf{H}$, respectively; $P_i^s$ and $M_i^s$ are the components of spontaneous polarization $\mathbf{P}^s$ and magnetization $\mathbf{M}^s$; $\epsilon_0$ and $\mu_0$ are the dielectric and magnetic susceptibilities of vacuum; $\epsilon_{ij}$ and $\mu_{ij}$ are the second-order tensors of dielectric and magnetic susceptibilities; $\beta_{ijk}$ and $\gamma_{ijk}$ are the third-order tensor coefficients; $\alpha_{ij}$ is the components of tensor $\alpha$ which is designated as the linear ME effect and corresponds to the induction of polarization by a magnetic field or a magnetization by an electric field. The rest of the terms in the preceding equations correspond to the high-order magnetoelectric effects parameterized by tensors $\beta$ and $\gamma$ [29]. The differentiation of the free energy leads to the polarization and magnetization expressed by 2.17 and 2.18:

$$P_i(\mathbf{E},\mathbf{H}) = -\frac{\partial F}{E_i} = P_i^s + \epsilon_0\epsilon_{ij}E_j + \alpha_{ij}H_j + \frac{1}{2}\beta_{ijk}H_jH_k + \gamma_{ijk}H_iE_j - ... \tag{2.17}$$

$$M_i(\mathbf{E},\mathbf{H}) = -\frac{\partial F}{H_i} = M_i^s + \mu_0\mu_{ij}H_j + \alpha_{ij}E_j + \beta_{ijk}E_iH_j + \frac{1}{2}\gamma_{ijk}E_jE_k - ... \qquad (2.18)$$

The ME mechanism effect may occur:

- in single-phase ME materials (including multiferroics), when an external applied electric field displaces ions from equilibrium positions which changes the magnetostatic and exchange interactions, affecting the magnetization [27].
- in composite multiferroic materials, when a piezoelectric strain in the ferroelectric constituent of the multiferroic heterostructure induces changes in the magnetic properties of the ferromagnetic constituent due to magnetostriction [65, 87].
- in a heterostructure comprising a ferroelectric insulator and a magnetic material, when a ferroelectric displacements of atoms at the interface may be reversed by an external electric field resulting in the sizable change of the interface magnetic moment [25] and surface (interface) magnetic anisotropy [26].
- in the insulator-ferromagnetic heterostructure, when an external electric field polarizes the insulator resulting in the carrier-mediated interface magnetoelectricity [64].

As a matter of fact, both magnetoelectric coupling and PMA are interface effects, therefore it is expected that a ferromagnetic material with PMA would be more sensitive to the magnetoelectric coupling than a material with a magnetic anisotropy parallel to the film plane.

# 3 | Interaction of light with magnetic systems

Light radiation is often used to study the properties of materials, from the composition, electronic structure, to the structural characterization. Among the possible magnetic characterization techniques, such as a vibrating sample magnetometry (VSM) and superconducting quantum interference device (SQUID), light radiation can also be exploited to access information on the magnetic properties of materials. If a linearly polarized light is incident onto a magnetic sample, its polarization main axis can be tilted and an ellipticity can be induced after the reflection. Linearly polarized light can be described by the superposition of circularly left and right polarized lights. In a magnetic material, these two components perceive a different complex refractive index, determining different absorption coefficients and the formation of a phase difference. As a result, the interaction of linearly polarized light with a magnetic material can affect both the rotation of the polarization direction and the dephasing of the light's linearly polarized components, resulting in an elliptical behavior. As it will be shown in the next sections, the rotation, and the ellipticity of the reflected light are, as first order approximation, linearly proportional to the amplitude of the magnetization vector. Light can therefore be used to access the information on the magnetic hysteresis loop of a material.

Investigating magnetic properties, light radiation can be more convenient than other magnetic measurements due to the following advantages:

- **Surface sensitivity**: light is primarily sensitive to the magnetization at the surface of the sample. This is useful when studying thin films or layered structures where the properties at the surface are of particular interest. That is the case of many composite materials studied in research areas related to spintronics and magnetism;
- **High spatial resolution**: focusing the light, it is possible to increase the spatial resolution of the measurement, giving the possibility to perform local magnetic characterizations. For this reason, magneto-optical measurements are suitable to characterize micro devices;

- **Non-intrusive probing benefit**: light can be used to study magnetic materials and devices, to which external stimuli (voltages, currents, heat, stress) are applied, to which VSM and SQUID techniques may be susceptible to disruptions. That comes useful when it is necessary to perform electrical and magnetic characterizations on a sample simultaneously.

In the following sections, we will first present the theoretical concepts to understand the physical principles behind the magneto-optical Kerr effect.

## 3.1. Circular and linear polarization of an electromagnetic wave

We will start with a brief description of the possible polarization states for an electromagnetic wave and then we will focus on how a linearly polarized light could get reflected by a magnetic material, which is at the core of the magneto-optic effect we are interested in. An electromagnetic wave can always be described as the linear combination of two circularly polarized waves, right (RCP) and left (LCP). In circularly polarized light, the electric field **E** rotates in the plane perpendicular to the direction of propagation. Right circularly polarized light (RCP) has **E** rotating clockwise at a given point in space regarding the opposite direction of the wave vector direction. On the other hand, left circularly polarized light (LCP) has **E** rotating counterclockwise. A visual description of left and right circular polarized light can be seen in the figure 3.1. RCP and LCP circularly polarized plane waves propagating along the positive $z$ direction can be described, respectively, by the relations (3.1) and (3.2) [31]:

$$\mathbf{E} = \frac{1}{2}E_0(\mathbf{e}_x + i\mathbf{e}_y)e^{-i(\omega t - kz)} + c.c. \tag{3.1}$$

$$\mathbf{E} = \frac{1}{2}E_0(\mathbf{e}_x - i\mathbf{e}_y)e^{-i(\omega t - kz)} + c.c. \tag{3.2}$$

where $\mathbf{e}_x$ and $\mathbf{e}_y$, are unit vectors along the positive $x$ and $y$ axes, and c.c. stands for complex conjugate. In elliptically polarized light the **E** unit vector at a given point in space describes an ellipse. The ratio of the minor axis of the ellipse to the major axis is the ellipticity, which is said positive or negative according to whether the ellipse is traversed clockwise or counterclockwise with respect the opposite direction of the wave vector direction. Circular polarization and linear polarization are special cases of elliptical polarization. A general description of an elliptical polarized wave is shown by the relation

(3.3):

$$\mathbf{E} = \frac{1}{2}E_0(\mathbf{e}_x + e^{j\delta}\mathbf{e}_y)e^{-i(\omega t - kz)} + c.c. \tag{3.3}$$

where $\delta$ is the phase difference between the $x$ and $y$ components of $\mathbf{E}$. With respect to our reference system, for $\delta = 0$, we have a linearly polarized wave with the electric field oscillating along the direction at 45° in the first and third $xy$ plane quadrant. If $\delta = \pi/2$ we have a wave that is RCP. For $0 < \delta < \pi/2$ we have a positive elliptically polarized light (PEP), while if $\pi/2 < \delta < \pi$ the wave will have a negative ellipticity (NEP). A polar plot of the polarization state of light as function of $\delta$ is shown in the figure 3.2.

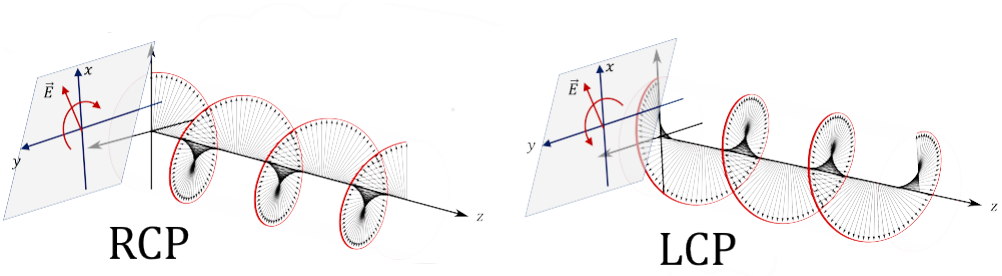


Figure 3.1: Left and right cirucular polarized light propagating along the $z$ direction.

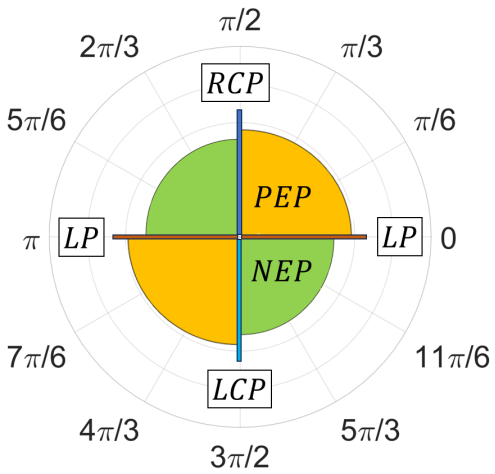


Figure 3.2: Polar plot of the polarization state of light as function of the phase difference $\delta$ between the $x$ and $y$ components of $\mathbf{E}$ (3.3).

## 3.2. Wave and Fresnel equations in a magnetic medium

The light propagation in a magnetic medium is described by Maxwell's equations (3.4), (3.5), (3.6) and (3.7):

$$\nabla \cdot \mathbf{D} = \rho \tag{3.4}$$

$$\nabla \times \mathbf{E} + \frac{\partial \mathbf{B}}{\partial t} = 0 \tag{3.5}$$

$$\nabla \cdot \mathbf{B} = 0 \tag{3.6}$$

$$\nabla \times \mathbf{H} - \frac{\partial \mathbf{D}}{\partial t} = \mathbf{j} \tag{3.7}$$

where $\mathbf{D} = \epsilon \mathbf{E}$ is the electric displacement, $\mathbf{E}$ electric field, $\epsilon$ the dielectric tensor, $\rho$ the free charge density and $\mathbf{j}$ the free density current. For the magnetic quantities it holds the relation $\mathbf{B} = \mu \mathbf{H}$, where $\mathbf{H}$ is the magnetic field, $\mu$ the permeability tensor. If we take the Maxwell-Faraday equation and using Gauss' law in a vacuum system, considering $\mathbf{j} = 0$ and $\rho = 0$, we find the relation (3.8):

$$\frac{1}{c^2}\frac{\partial^2}{\partial t^2}\epsilon \mathbf{E} - \nabla^2 \mathbf{E} = 0 \tag{3.8}$$

where $c = \frac{1}{\sqrt{\epsilon_0 \mu_0}}$ is the speed of light in vacuum. A similar equation can be found also for the magnetic field $\mathbf{B}$. If we consider a harmonic solution of the form $\mathbf{E}(\mathbf{r}, t) = \mathbf{E}_0 e^{-i(\omega t - \mathbf{k}\cdot\mathbf{r})}$ for equation (3.8) with wave vector $\mathbf{k} = \frac{\omega}{c}\mathbf{n}$, where $\mathbf{n}$ is the refractive index in the propagating medium, it is possible to retrieve the Fresnel's equation (3.9) as done in previous works [56] [31]:

$$(n^2 \mathbf{1} - \epsilon - \mathbf{n} : \mathbf{n}) \cdot \mathbf{E} = 0 \tag{3.9}$$

where $n^2 = \mathbf{n} \cdot \mathbf{n}$, $\mathbf{1}$ is the dyadic unit tensor and $\mathbf{n} : \mathbf{n} = n_i n_j$ for $i$,$j = x$,$y$,$z$ is, by definition, with the Einstein convention, the dyadic product. For an isotropic, nonmagnetic medium, $\epsilon$ would be a diagonal tensor with all components equal to $\epsilon_{xx}$, letting $n^2 = \epsilon_{xx}$ be the solution of the equation. This solution is the standard relation between refractive index and dielectric constant. For a magnetic medium however, the off-diagonal components of the dielectric tensor can be non-zero and depend on the magnetization vector $\mathbf{M}$ of the system. As a first order approximation, the dielectric tensor $\epsilon$ for a magnetic medium was proven by You and Shin [86] to be equal to the relation (3.10):

$$\epsilon = \epsilon_{xx} \begin{pmatrix} 1 & -iQm_z & iQm_y \\ iQm_z & 1 & -iQm_x \\ -iQm_y & iQm_x & 1 \end{pmatrix} \tag{3.10}$$

where:

- $m_x$, $m_x$ and $m_z$ are the $x$, $y$ and $z$ components of the magnetization vector normalized regarding the magnetization saturation $M_s$ of the material;
- $Q$ is Voigt's magneto-optical constant and represents the quantum mechanical effect of the interaction between the electromagnetic field and the electrons responsible for the magnetic behavior.

For generality, all physical quantities are treated as complex numbers.

## 3.3. Magnetic-optical Kerr effect

The magneto-optical Kerr effect (MOKE) describes a change in polarization and ellipticity of light reflected from a surface with a given magnetization $\mathbf{M}$. By solving the Fresnel equation (3.9), using the dielectric tensor (3.10) for a magnetic material, we can therefore find the refractive index perceived by the RCP and LCP light components. The induced Kerr rotation is associated to the different phase delay undergone by RCP and LCP components (birefringence), while the Kerr ellipticity to the different absorption of RCP and LCP light (dichroism) [31].

In the following, we consider a linearly polarized incident light, travelling through a non-magnetic material, on a magnetic media with an incident angle $\theta_0$ as it is sketched in the figure 3.3. The non-magnetic and magnetic media are defined by the refractive indexes $n_0$ and $n_1$, respectively. The light transmission angle $\theta_1$ is given by the Snell's law (3.11):

$$n_0 \sin\theta_0 = n_1 \sin\theta_1 \tag{3.11}$$

As shown in the figure 3.4, the incident and reflected light are described in terms of $s$ and $p$ wave components: a $s$-wave $\mathbf{e}_s = \begin{pmatrix} 0 \\ 1 \end{pmatrix}$, or transverse-electric wave (TE), is a linearly polarized light in which the electric field oscillates perpendicularly with respect to the plane of incidence ($yz$ plane); a $p$-wave $\mathbf{e}_p = \begin{pmatrix} 1 \\ 0 \end{pmatrix}$, or transverse-magnetic wave (TM), is a linearly polarized light in which the electric field oscillates parallel regarding the

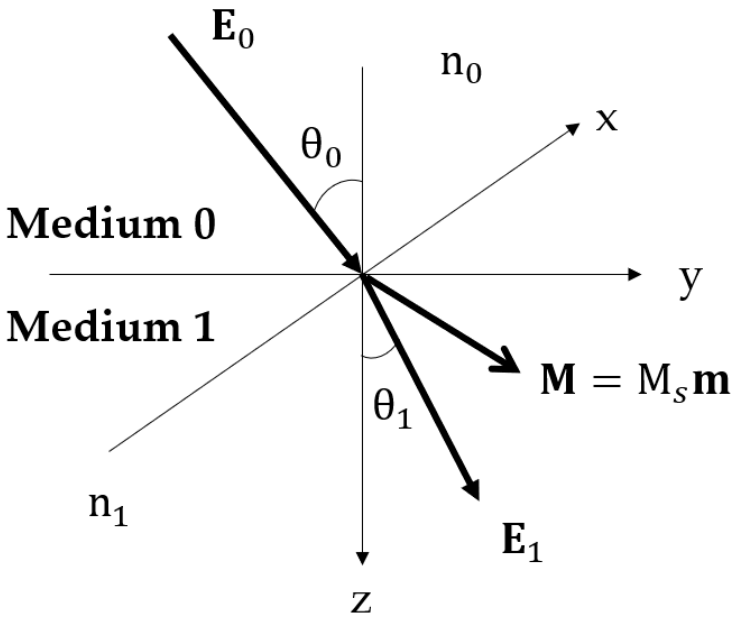


Figure 3.3: The coordinate system of the nonmagnetic (medium 0) and the magnetic regions (medium 1), with refractive indexes $n_0$ and $n_1$. $\theta_0$ and $\theta_1$ are the incident and light transmission angles regarding the plane of incidence ($yz$ plane) [86].

plane of incidence. As it was demonstrated by You and Shin [86], the magneto-optical matrix describing the reflection properties of a magnetic medium, at the interface with a non-magnetic medium, is given by the relation (3.12):

$$\mathbf{R} = \begin{pmatrix} r_{pp} & r_{ps} \\ r_{sp} & r_{ss} \end{pmatrix} \tag{3.12}$$

where $r_{ij}$ is the ratio between the incident $j$ polarized electric field and the reflected $i$ polarized electric field and is expressed by the relations (3.13), (3.14), (3.15), (3.16):

$$r_{pp} = \frac{n_1 \cos\theta_0 - n_0 \cos\theta_1}{n_1 \cos\theta_0 + n_0 \cos\theta_1} - \frac{i2n_0 n_1 \cos\theta_0 \cos\theta_1 m_x Q}{n_1 \cos\theta_0 + n_0 \cos\theta_1} \tag{3.13}$$

$$r_{sp} = \frac{in_0 n_1 \cos\theta_0 (m_y \sin\theta_1 + m_z \cos\theta_1) Q}{(n_1 \cos\theta_0 + n_0 \cos\theta_1)(n_0 \cos\theta_0 + n_1 \cos\theta_1) \cos\theta_1} \tag{3.14}$$

$$r_{ss} = \frac{n_1 \cos\theta_0 - n_0 \cos\theta_1}{n_1 \cos\theta_0 + n_0 \cos\theta_1} \tag{3.15}$$

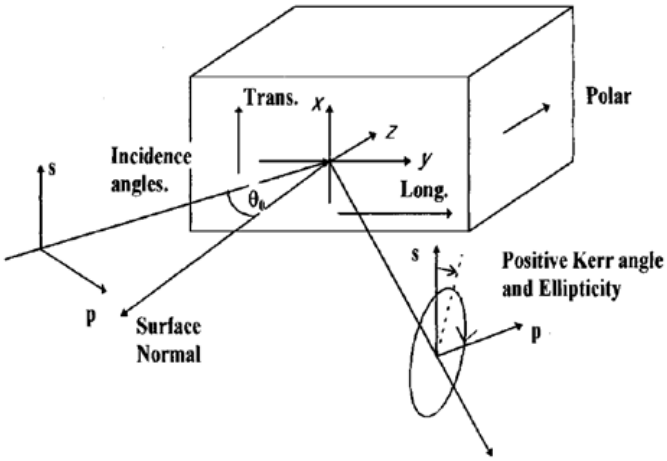


Figure 3.4: Schematic configurations for the polar, longitudinal, and transverse magneto-optical Kerr effects [86].

$$r_{ps} = \frac{in_0 n_1 \cos\theta_0 (m_y \sin\theta_1 - m_z \cos\theta_1) Q}{(n_1 \cos\theta_0 + n_0 \cos\theta_1)(n_0 \cos\theta_0 + n_1 \cos\theta_1) \cos\theta_1} \tag{3.16}$$

These solutions are valid within the first-order approximation of the magneto-optical constant $Q$.

We now define $\Theta_K$ the complex Kerr angle as the combination of the Kerr $\theta_K$ rotation and ellipticity $\epsilon_K$ of the reflected light, as shown by the relation (3.17):

$$\Theta_K = \theta_K + i\epsilon_K \tag{3.17}$$

It is possible to demonstrate that the complex Kerr angles $\Theta_K^p$ and $\Theta_K^s$, respectively for an incident $p$ and $s$ waves, can be obtained starting from the magneto-optical Fresnel reflection matrix coefficients, as shown by the relations (3.18) and (3.19):

$$\Theta_K^p = \theta_K^p + i\epsilon_K^p = \frac{r_{sp}}{r_{pp}} = \frac{\cos\theta_0 (m_z + m_y \tan\theta_1)}{\cos(\theta_0 + \theta_1)} \frac{in_0 n_1 Q}{n_1^2 - n_0^2} \tag{3.18}$$

$$\Theta_K^s = \theta_K^s + i\epsilon_K^s = \frac{r_{ps}}{r_{pp}} = \frac{\cos\theta_0 (m_z - m_y \tan\theta_1)}{\cos(\theta_0 - \theta_1)} \frac{in_0 n_1 Q}{n_1^2 - n_0^2} \tag{3.19}$$

From the relations (3.18) and (3.19) we find that the Kerr rotation and ellipticity for the reflected wave are proportional to the components of the normalized magnetization vector $\mathbf{m}$. Since the information regarding the magnetization saturation $M_s$ is contained in the

Voigt constant $Q$, and their mutual dependence is generally not known, magneto-optical Kerr effects do not allow retrieving the information regarding the absolute magnetization and magnetic moment of a material. Phenomenologically, we differentiate between three distinct MOKE geometries: longitudinal, polar and transversal. These are determined by the orientation of the magnetization regarding the plane of incidence of light and the surface of the sample, as shown in the figure 3.4. In the longitudinal Kerr effect $\mathbf{m}$ is parallel to the surface and lies in the light incident plane, in the polar Kerr effect $\mathbf{m}$ is normal to the reflecting $xy$ surface, while in the transverse Kerr effect $\mathbf{m}$ is parallel to the surface but perpendicular to the plane of incidence. In thin films, the polar component is generally zero as the shape anisotropy confines the magnetization $\mathbf{m}$ along the surface of the sample.

### 3.3.1. Longitudinal MOKE

In a longitudinal MOKE geometry as show in the Figure 3.5, the magnetization is such that $m_y \neq 0$ and $m_x = m_z = 0$. The dielectric tensor $\epsilon$ of the magnetic sample and the induced Kerr complex angles $\Theta_K^p$ and $\Theta_K^s$ for the reflected light are expressed by the relations (3.20), (3.21), (3.22):

$$\epsilon = \epsilon_{xx} \begin{pmatrix} 1 & 0 & iQm_y \\ 0 & 1 & 0 \\ -iQm_y & 0 & 1 \end{pmatrix} \tag{3.20}$$

$$\Theta_K^p = \theta_K^p + i\epsilon_K^p = \frac{r_{sp}}{r_{pp}} = \frac{\cos\theta_0 m_y \tan\theta_1}{\cos(\theta_0 + \theta_1)} \frac{in_0 n_1 Q}{n_1^2 - n_0^2} \tag{3.21}$$

$$\Theta_K^s = \theta_K^s + i\epsilon_K^s = \frac{r_{ps}}{r_{pp}} = -\frac{\cos\theta_0 m_y \tan\theta_1}{\cos(\theta_0 - \theta_1)} \frac{in_0 n_1 Q}{n_1^2 - n_0^2} \tag{3.22}$$

The relations (3.22) and (3.21) are different from zero only when the angle $\theta_0 > 0$. In fact, if $\theta_0 = 0$, by the Snell law (3.11), $\theta_1$ would be zero, thus causing $\tan\theta_1 = 0 \rightarrow \Theta_K^{s,p} = 0$. For this reason, whenever we want to observe a longitudinal MOKE, the light must not be at normal incidence regarding the sample surface.

### 3.3.2. Polar MOKE

In a polar MOKE configuration as show in the Figure 3.5, the magnetization is such that $m_z \neq 0$ and $m_x = m_y = 0$. The dielectric tensor $\epsilon$ of the magnetic sample and

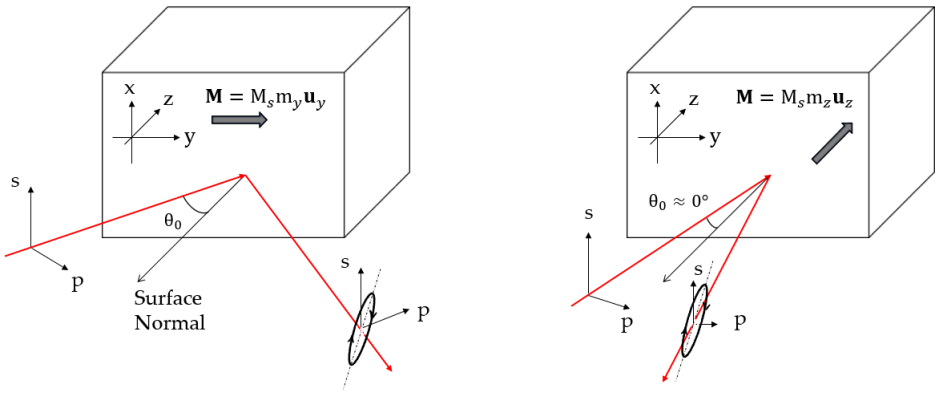


Longitudinal MOKE Polar MOKE

Figure 3.5: Schematic configurations for the longitudinal, and polar magneto-optical Kerr effects.

the induced Kerr complex angles $\Theta_K^p$ and $\Theta_K^s$ for the reflected light are expressed by the relations (3.23), (3.24), (3.25):

$$\epsilon = \epsilon_{xx} \begin{pmatrix} 1 & -iQm_z & 0 \\ iQm_z & 1 & 0 \\ 0 & 0 & 1 \end{pmatrix} \tag{3.23}$$

$$\Theta_K^p = \theta_K^p + i\epsilon_K^p = \frac{r_{sp}}{r_{pp}} = \frac{\cos\theta_0 m_z}{\cos(\theta_0 + \theta_1)} \frac{in_0 n_1 Q}{n_1^2 - n_0^2} \tag{3.24}$$

$$\Theta_K^s = \theta_K^s + i\epsilon_K^s = \frac{r_{ps}}{r_{pp}} = \frac{\cos\theta_0 m_z}{\cos(\theta_0 - \theta_1)} \frac{in_0 n_1 Q}{n_1^2 - n_0^2} \tag{3.25}$$

In a polar configuration, having $\mathbf{m}$ only along $z$, to maximize the complex Kerr angle signals, we need to maximize the term $\cos\theta_0$, which implies we need to work as close as possible to normal incidence, meaning $\theta_0 = 0$. The polar geometry is the only one where MOKE can be observed at normal incidence [59].

# 4 | Magnetic and ferroelectric detection techniques for thin films

This chapter describes the experimental apparatus and techniques used to conduct the magnetic and ferroelectric characterizations of thin film samples.

## 4.1. Longitudinal MOKE

In this section, we present a longitudinal MOKE system we developed to characterize the in-plane magnetization of thin films. Since thin films could present magnetic easy and hard axes along the plane, we integrated a rotational sample to allow in-plane angle resolved measurements.

### 4.1.1. Setup

A general longitudinal MOKE setup scheme is shown in the figure 4.1a, where the optical components and instruments are marked by respective abbreviations and the directionality of light (**k**-vector) is given by arrows. To realize a MOKE measurement, we need in principle:

- a laser light source $L$;
- a first linear polarizer $P_1$ to linearly $s(p)$-polarize the light source;
- a magnet $M$ to induce the sample $S$ to a longitudinal magnetization;
- a second linear polarizer $P_2$ to analyze the new polarization state after reflection of the incident polarized beam from the sample $S$;
- a photodiode $PD$ to detect the light passed through the polarizer $P_2$.

As we discussed in the subsection 3.3.1, to observe the longitudinal MOKE, the light ray

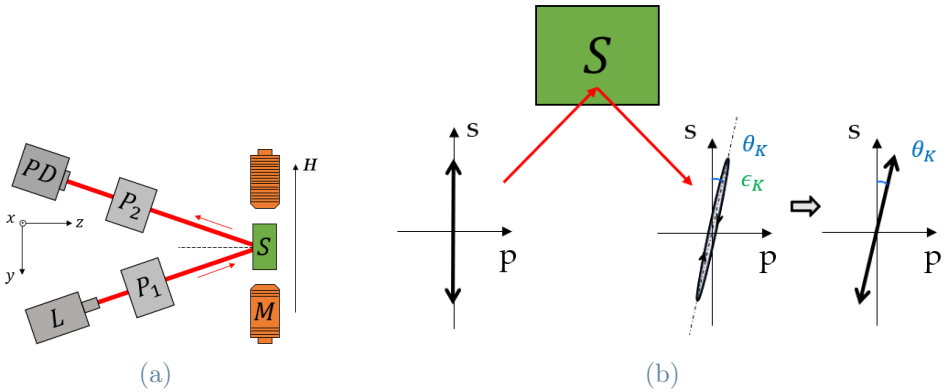


Figure 4.1: (a) Longitudinal MOKE setup scheme. (b) Schematic draw of the rotation $\theta_K$ and ellipticity $\epsilon_K$ induced to an s-polarized light by a magnetic sample.

must not be at normal incidence regarding the sample surface, as depicted in the setup scheme 4.1a. After the reflection by the magnetic sample, the beam polarization will gain a Kerr rotation $\theta_K$ and ellipticity $\epsilon_K$. In general, the ellipticity $\epsilon_K$ is so small that the sample action on the polarization of incident light can be considered as a simple rotation of the incident electric field vector, as depicted in figure 4.1b. Within this approximation, we shall dispose the polarizers $P_1$ and $P_2$ in a cross configuration, with their optical axes perpendicular to each other, to let $P_2$ transmit the light polarization component induced by the sample only.

If we refer to the coordinate system in figure 4.1a, the electric field can be described as a vector with two components $p$ and $s$, parallel and perpendicular to the $yz$ plane of incidence. Using as mathematical vector bases $\mathbf{e}_s = \begin{pmatrix} 0 \\ 1 \end{pmatrix}$ and $\mathbf{e}_p = \begin{pmatrix} 1 \\ 0 \end{pmatrix}$ to describe $s$ and $p$ waves, a generic electric field is given by the linear combination of $\mathbf{e}_s$ and $\mathbf{e}_p$ basis, as shown by the relation (4.1):

$$\mathbf{E} = E_s\mathbf{e}_s + E_p\mathbf{e}_p = \begin{pmatrix} E_p \\ E_s \end{pmatrix} \tag{4.1}$$

Working in a geometrical optics regime, we can describe the light interactions with the different optical components with optical matrices, built using the same $s$ and $p$ waves vector basis. The optical matrix for the generic optical polarizer $P$ is given by the relation (4.2) [49]:

$$\mathbf{A} = \begin{pmatrix} \cos^2\alpha & \sin\alpha\cos\alpha \\ \sin\alpha\cos\alpha & \sin^2\alpha \end{pmatrix} \tag{4.2}$$

where $\alpha$ is the angle between the optical axis of the polarizer and the $yz$ plane of incidence. Assume that the two polarizers $P_1$ and $P_2$ are in the cross-configuration, such that:

- the $P_1$ transmission axis is parallel to the $s$-direction with $\alpha_1 = \pi/2$;
- the $P_2$ transmission axis is parallel to the $p$-direction with $\alpha_2 = 0$.

Then, the polarizers $P_1$ and $P_2$ will be described by the optical matrices (4.3) and (4.4), respectively:

$$\mathbf{A}_1 = \begin{pmatrix} 0 & 0 \\ 0 & 1 \end{pmatrix} \tag{4.3}$$

$$\mathbf{A}_2 = \begin{pmatrix} 1 & 0 \\ 0 & 0 \end{pmatrix} \tag{4.4}$$

Then, the light crossing the polarizers $P_1$ and $P_2$ will get only $s$-wave and $p$-wave components to be transmitted, respectively. The reflection matrix $\mathbf{R}$ is given by magneto-optical Fresnel reflection matrix (3.12). The electric field $\mathbf{E}_0$ coming out of the laser source $L$ can be described by the relation (4.1). Then, when the first polarizer is $s$ and the second polarizer (analyzer) is $p$, the electric field $\mathbf{E}_{PD}$ arriving at the detector $PD$ is obtained by calculating the product matrix of the operators as shown by the relation (4.5):

$$\mathbf{E}_{PD} = \mathbf{A}_2 \cdot \mathbf{R} \cdot \mathbf{A}_1 \cdot \mathbf{E}_0 = \begin{pmatrix} r_{ps}E_s \\ 0 \end{pmatrix} \tag{4.5}$$

This result tells us that the magnetic sample induces a $p$ wave component on the incident $s$ wave laser light, which implies that the light polarization is rotated by a Kerr angle $\theta_K$. Geometrically, $\theta_K$ is related to the magneto-optical Fresnel reflection matrix coefficients, as shown by the relation (4.6):

$$\tan\theta_K = \frac{r_{ps}}{r_{ss}} \tag{4.6}$$

For a small $\theta_K$, it is possible to write $\tan\theta_K = \frac{r_{ps}}{r_{ss}} \sim \theta_K$, thus, $r_{ps} \sim r_{ss}\theta_K$ as a first order approximation. Then, at the detector, $\mathbf{E}_{PD}$ can be rewritten with the relation (4.7):

$$\mathbf{E}_{PD} = \begin{pmatrix} r_{ss}\theta_K E_s \\ 0 \end{pmatrix} \tag{4.7}$$

However, what the photodiode $PD$ can measure is not $\mathbf{E}_{PD}$ but its intensity $I \propto |\mathbf{E}_{PD}|^2$. For the consideration made in the section 3.3.1, as a first order approximation we get $I \propto |\mathbf{E}_{PD}|^2 = r_{ss}^2\theta_K^2 E_s^2 \propto \theta_K^2 \propto M^2$. Since $I \propto M^2$, the light intensity on the photodiode will not mimic the hysteresis loop of the magnetization because positive and negative $M$ values give the same contribution (e.g., a perfectly square hysteresis loop $M(H)$ will give a constant value in the $M^2(H)$ representation). This issue can be solved if we work in a quasi-crossed configuration for the two polarizers $P_1$ and $P_2$ meaning that $\alpha_1 = \pi/2$ and $\alpha_2 \approx 0$.

If $\alpha_2 \approx 0$, the optical matrix for the polarizer $P_2$ can be approximated by the relation (4.8).

$$\mathbf{A}_2 = \begin{pmatrix} \cos^2\alpha_2 & \sin\alpha_2\cos\alpha_2 \\ \sin\alpha_2\cos\alpha_2 & \sin^2\alpha_2 \end{pmatrix} \sim \begin{pmatrix} 1 & \alpha_2 \\ \alpha_2 & 0 \end{pmatrix} \tag{4.8}$$

Within this approximation, by evaluating once again the product matrix considering the new $A_2$ matrix for the polarizer $P_2$, the electric field arriving at the detector can be written with the relation (4.9):

$$\mathbf{E}_{PD} \sim \begin{pmatrix} r_{ss}\theta_K E_s + \alpha_2 r_{ss} E_s \\ \alpha_2 r_{ss}\theta_K E_s \end{pmatrix} \tag{4.9}$$

Then, the intensity at the detector D can be written with the relation (4.10):

$$I \propto |\mathbf{E}_{PD}|^2 \propto \alpha_2^2 r_{ss}^2 E_s^2 + (r_{ss}^2 E_s^2 + \alpha^2 r_{ss}^2 E_s^2)\theta_K^2 + 2\alpha r_{ss}^2 E_s^2 \theta_K \tag{4.10}$$

Working in a quasi-crossed configuration for the two polarizers $P_1$ and $P_2$, neglecting quadratic terms in $\theta_k$ found from the relation (4.10), we get the equation (4.11):

$$I \propto \alpha_2^2 r_{ss}^2 E_s^2 + 2\alpha r_{ss}^2 E_s^2 \theta_K \tag{4.11}$$

Since $I \propto \theta_K \propto M$, now it is possible to resolve the magnetic signals such as hysteresis loops.

However, since MOKE signals generally have a small amplitude, an intensity modulator and a lock-in amplifier (LIA) are introduced to improve the signal-to-noise ratio. This integration serves to mitigate the influence of low-frequency noise (1/f) introduced by electronic components, the signal acquisition chain, and ambient light disturbances. Light modulation can be realized by amplitude modulation, via a chopper, or by phase modulation, via a photoelastic modulator. The two modulation techniques are discussed in the subsections 4.1.2 and 4.1.3.

### 4.1.2. Light signal modulation with a chopper

An optical chopper is a rotating disc mechanical shutter used to interrupt the light beam periodically. The chopper operates at variable frequency between 0 and up to a maximum of 1000 Hz. Since it cannot provide a high-frequency modulation, the rejection of the low frequency noise (1/f) will be lower than other modulation techniques (e.g., a photoelastic modulator working at 50 kHz). Still, it gains in terms of simplicity of the device. Since, the chopper provides only a time modulation of the electric field amplitude without affecting the polarization state of the laser beam, it can be used in a longitudinal MOKE setup, working with the polarizer $P_1$ and $P_2$ in a cross-configuration, without affecting the optical signal theory previously exposed in the subsection 4.1.1.

### 4.1.3. Light signal modulation with a photoelastic modulator

In this subsection, we discuss the modulation technique, via a photoelastic modulator, we decided to implement in the longitudinal MOKE setup we developed.

A photo elastic modulator (PEM) is a crystal which exhibits a birefringence when mechanically stressed. As a first order approximation, the birefringence response is proportional to the induced stress. When the crystal is stressed, compressed, or stretched, the polarization components perpendicular or parallel to the crystal optical axis travel at different speed, causing a phase shift $\delta_0$ in the two components. By setting the crystal optical axis parallel to the $s$-direction, and modulating the crystal stress applying a modulated voltage to piezoelectric material attached to it, it is possible to modulate the phase difference between the $s$ and $p$ light components. The photoelestic modulator operates modulating the light signal at 50 $kHz$. By exploiting the crystal birefringence, this instrument allows retrieving both the information regarding the Kerr rotation $\theta_K$ and ellipticity $\epsilon_K$. The high-frequency modulation allows providing a better rejection of the low frequency noise (1/f) regarding the chopper modulator, but it loses in complexity and fragility.

Figure 4.2 shows a picture of the longitudinal MOKE setup with the photoelastic mod-

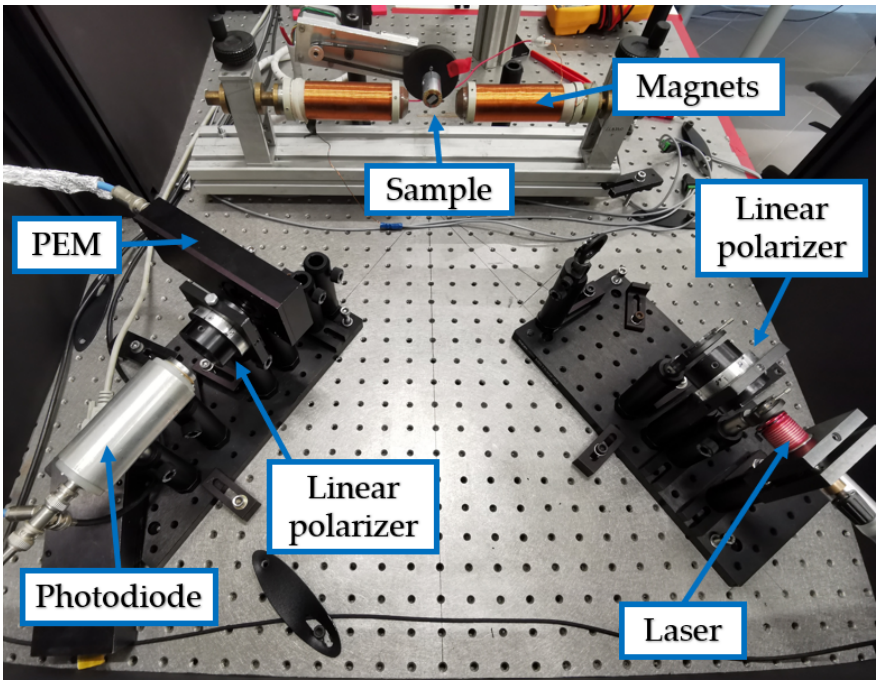


Figure 4.2: Longitudinal MOKE setup.

ulator. The photoelastic modulator was placed, in between of the magnetic sample and the second light analyser. If the second polarizer transmission axis is at 45° regarding the first polarizer axis, it is possible to demonstrate that with a lock-in amplifier, demodulating at frequency $f$ and $2f$ respectively, we obtain two voltage signals proportional to the rotation and Kerr ellipticity, as shown by the relations (4.12) and (4.13) [59]:

$$V_{1f} = 4V_{DC} \cdot J_1(\delta_0) \cdot \epsilon_K \tag{4.12}$$

$$V_{2f} = 4V_{DC} \cdot J_2(\delta_0) \cdot \theta_K \tag{4.13}$$

where:

- $f$ is the modulation frequency of the photoelastic modulator;
- $\delta_0$ is the phase difference that is induced between the $s$ and $p$ light travelling components;
- $V_{DC}$ is the DC component of the light measured by the photodiode;
- $J_n$, with $n = 1, 2$, is the $n$-th Bessel function evaluated in $\delta_0$.

$\delta_0$ is set at 2.41 rad (137.9°) because it maximizes the amplitude of the signals (4.12) and

(4.13) [59].

Moreover, from the relations (4.12) and (4.13), we can get direct information on the polarization rotation and ellipticity induced on the laser light after the reflection. To do that is necessary to retrieve the DC component of the laser signal. Then, it is possible to evaluate the Kerr rotation $\theta_K$ and the ellipticity $\epsilon_K$ with the relations (4.14) and (4.15) [59].

$$\theta_K = \frac{\sqrt{2}}{4J_2(\delta_0)}\frac{V_{2F}}{V_{DC}} \tag{4.14}$$

$$\epsilon_K = \frac{\sqrt{2}}{4J_1(\delta_0)}\frac{V_{1F}}{V_{DC}} \tag{4.15}$$

To reduce the ambient light noise contributions to the MOKE signals, the setup was closed inside a black box. The light source used in this longitudinal setup is a red laser diode (635 nm), which is made to impinge on a sample with an angle of incidence of 34° regarding the normal direction of the sample. The longitudinal MOKE setup spatial resolution is determined by the laser spot size, which is 500 $\mu$m. The dimension of the light spot size sets the minimum spatial area across which the MOKE system can effectively distinguish between different magnetic configurations, such as magnetic domains or microstructures.

### 4.1.4. Signal-to-Noise ratio

The quality of a signal is quantified by the signal-to-noise ratio (SNR) which compares the level of the signal to the level of background noise of the system. The SNR ratio parameter for a magneto-optical loop measurement is defined by the equation (4.16) [28].

$$SNR = \frac{\Delta}{\sqrt{\sigma_+^2 + \sigma_-^2}} \tag{4.16}$$

where:

- $\Delta$ is the hysteresis loop opening amplitude, calculated as the difference between the mean values of the magnetic data distributions at positive and negative saturation, as shown by the orange and blue regions in the figures 4.3a and 4.3b;
- $\sigma_+^2$ and $\sigma_-^2$ are the standard deviations of the magnetization data sets at positive and negative saturation regime, as it is shown in the figures 4.3a and 4.3b.

A high SNR (4.16) can be determined by a high $\Delta$ and by a low $\sigma$, which can be obtained by a proper and noise filtering by the signal acquisition electronics and by optimizing the configuration of the optical components (linear polarizers, waveplates, prisms, etc...) crossed by the laser light.

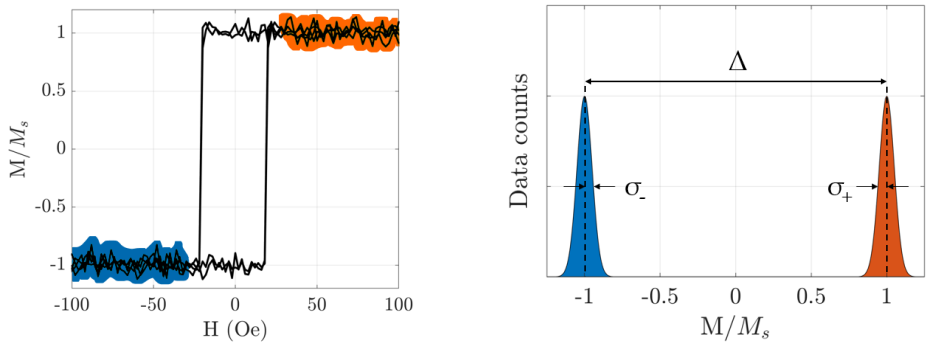


(a) (b)

Figure 4.3: (a) Normalized hysteresis loop positive and negative saturation regions. (b) Normalized magnetization data at positive and negative saturation for a MOKE measurement.

### 4.1.5. Longitudinal MOKE measurements on an iron thin film

In this subsection, we present the longitudinal MOKE measurements on a 10 nm iron thin film, epitaxially grown on a 1 × 1 cm MgO(100) substrate, presenting magnetic cubic anisotropy along the diagonals of the sample, which coincide with the [100] and [010] iron crystallographic directions. The sample was mounted such that one of the diagonal easy axis was parallel to the direction of the $H$ field generated by the magnets. Measurements were done by modulating the light with the photelastic modulator, as we discussed in the section 4.1.3.

The figures 4.4a and 4.4b display the normalized iron film magnetization hysteresis signals for $V_{1F}$ and $V_{2F}$, derived from averaging ten individual loops. In the table 4.1, we displayed the magnetic parameters, retrieved from the 1F and 2F hysteresis curves, related to:

- the coercive fields $H_c$;
- the $M_r/M_S$ ratio, where $M_r$ is the magnetization remanence (at H = 0) and $M_s$ the saturation magnetization of the iron film;
- the magneto-optic SNR parameter (4.16);

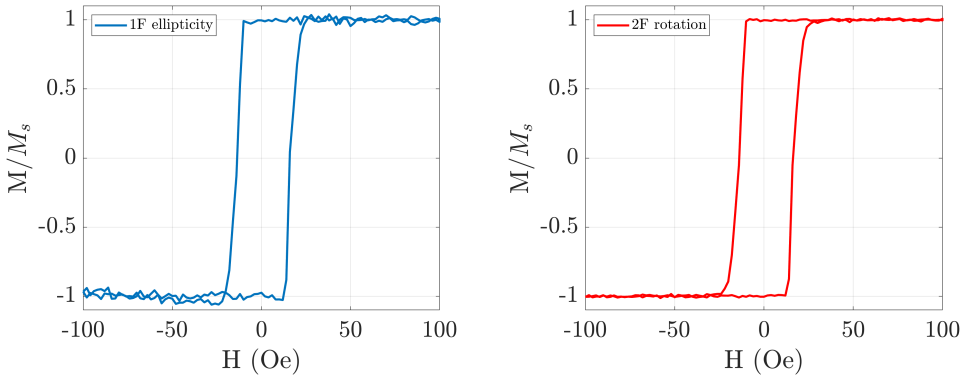


(a) 1F ellipticity magnetization signal. (b) 2F rotation magnetization signal.

Figure 4.4: 1F and 2F longitudinal MOKE measurements for a 10 nm thin film of iron grown on a MgO(100) substrate.

| **Signal** | $H_c$ [Oe] | $M_r/M_S$ | SNR | $\theta_K$ [mrad] | $\Delta\theta_k$ [mrad] | $\epsilon_K$ | $\Delta\epsilon_k$ |
|---|---|---|---|---|---|---|---|
| **1F** | 14.7 | 0.95 | 75 | - | - | $2.7 \cdot 10^{-4}$ | $10^{-6}$ |
| **2F** | 15.1 | 0.96 | 239 | 0.88 | 0.001 | - | - |

Table 4.1: 10 nm thin film of iron longitudinal MOKE magnetic parameters

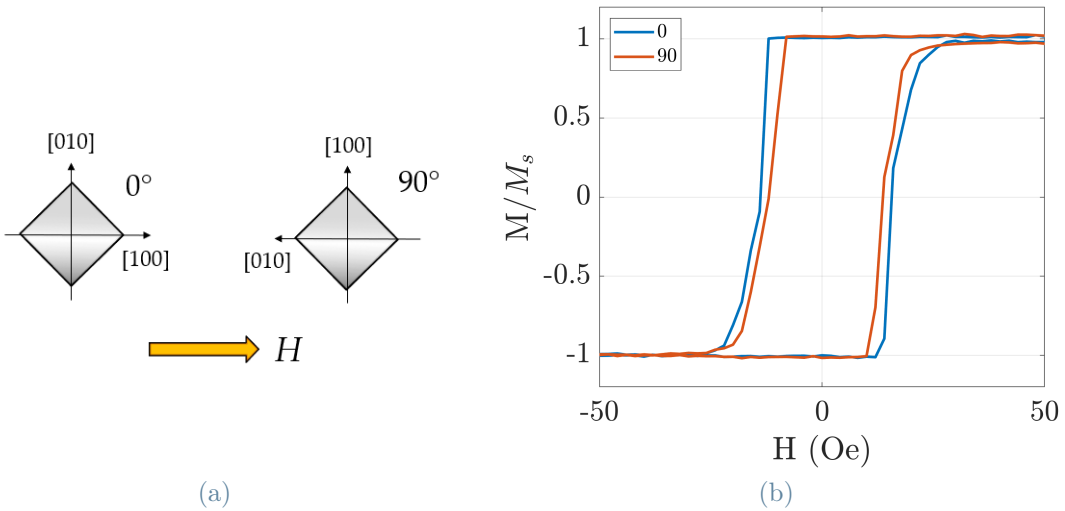


(a) (b)

Figure 4.5: (a) Fe [100] and [010] iron crystallographic directions regarding the longitudinal $H$ field. (b) In-plane magnetic anisotropy characterizations for the Fe film.

- the induced Kerr rotation $\theta_K$ and ellipticity $\epsilon_K$ amplitudes (4.14) and (4.15) and resolution at saturation ($|H| > 20$ Oe).

The higher SNR we calculated for the 2F signal regarding the 1F signal has to be related to a different magneto-optical response that has occurred between the iron film and the red laser wavelength. The induced Kerr rotation and ellipticity amplitudes measured are coherent with what it was found in previous works [37, 61]. Figure 4.5b displays the angle resolved measurements for the iron film along its [100] and [010] crystallographic directions (depicted in figure 4.5a). For the curves at 0° and 90° we obtain the coercive fields 14.7 and 13 Oe, which difference could be related to a different domain dynamics along the two iron [100] and [010] easy axes.

## 4.2. Vibrating Sample Magnetometer

The vibrating sample magnetometer (VSM) is an instrument, which functioning is based on the Faraday's Law of Induction (3.5), which allows determining with high precision magnetic information, e.g., the magnetic moment of a material [1], which cannot be accessed by magneto-optical measurments as we discussed in the section 3.3. The VSM is a technique sensitive to the total magnetic moment of the sample, so it cannot be used to resolve single layers or micro devices (fabricated on the same sample) contributions. Due to their mutual advantages and limitations, combining measurements based on magneto-optical and magnetic induction effects can provide a more complete characterization of a thin film magnetic materials.

VSM measurements are done by attaching the sample to a diamagnetic sample holder, which is made to vibrate in between two pick-up coils and two pole pieces of an electromagnet (as depicted in figure 4.6), which provide a magnetic field of high homogeneity in the perpendicular direction regarding the sample holder axis. An oscillator makes the sample move vertically following a sinusoidal signal. Since the sample is magnetized by the magnetic field, this motion causes a change of the magnetic flux passing through the coils, and therefore a current is induced whose amplitude is proportional to the magnetic moment of the sample. Hence, by measuring an electrical signal (through a lock in amplifier synchronized with the mechanical oscillator) we get to know the magnitude of the sample magnetization. Since the VSM is sensible to any form of magnetism, the measurement will always be affected by diamagnetic and paramagnetic contributions due to:

- the sample holder, made of glass, which is diamagnetic;

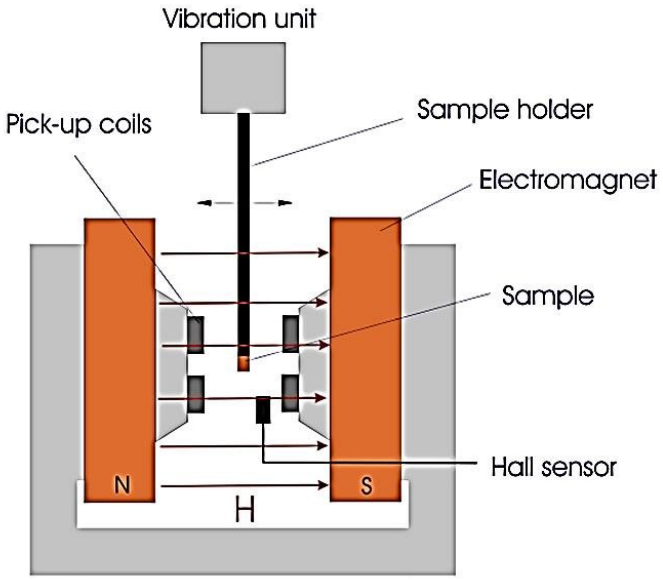


Figure 4.6: VSM device scheme. The sample is put within a uniform magnetic field **H**, generated by an electromagnet, and a pair of pick-up coils used to measure the magnetic signal from the sample exploiting the Faraday Neumann Lenz law. The sample is attached to a sample holder, which is connected to a mechanical system that makes the sample vibrate vertically.

- the non-ferromagnetic layers, that may be either paramagnetic or diamagnetic;
- the adhesive tape used to attach the sample to the sample holder.

The VSM software compensates for these magnetic contributions after a background calibration based on measurements of the sample holder with adhesive tape and the sample holder with a clean substrate layer without the FM material has been conducted.

The VSM used in this thesis work is the MicroSense Easy (EZ9) VSM [1].

## 4.3. Ferroelectric characterization techniques

In this section, we discuss the fundamental techniques used to characterize the ferroelectric material investigated in this thesis, which is Hafnium Zirconium Oxide (HZO).

### 4.3.1. Ferroelectric training

Ferroelectric materials might not show ferroelectric behavior in as-grown condition, even in epitaxial ferroelectric films. To improve the ferroelectricity of a FE material, a series of cycling electric fields over the ferroelectric junction of the sample are applied. Such a pro-

cedure, called *training* of the ferroelectric, redistributes the defects inside the ferroelectric layer, allowing previously pinned ferroelectric domains to switch their polarization and decreasing the junction leakage current [72]. The defects rearrangement and the leakage current decrease are also essential to improve the identification of the ferroelectric switching peak when performing a PUND measurement (discussed in the subsection 4.3.2).

Studies have indicated that a training processes can affect the HZO polarization response [72]. A training process allows the HZO polarization enhancement due to the redistribution of:

- oxygen vacancies [38, 83];
- pinned ferroelectric domains, which could prevent the HZO from presenting a ferroelectric orthorhombic Pbc2 phase [4], in which the HZO ferroelectric response is higher [55].

### 4.3.2. PUND technique

Positive-Up-Negative-Down (PUND) technique is the method used in this thesis to obtain I-V curve characterizations. The technique consists of five voltage pulses applied to the ferroelectric junction of the sample. In Figure 4.7a is reported the concept of PUND. A first negative pulse (X) pre-polarizes the ferrolectric layer in one direction. The second (P) pulse switches the polarization to the opposite direction. The current measured when the second (P) is applied is given by two contributions:

- the non-ferroelectric contributions [72] (yellow curve), in turn defined by:
  - the leakage currents ($I_{leakage}$), related to the resistive response of the capacitor junction;
  - the capacitor's charging current ($I_{DE}$);
- the ferroelectric contributions ($I_{FE}$), which are represented by a peaked current curve due to the caused by the HZO ferroelectric domain switching the ferroelectric transition from one state of polarization to another (red curve).

The third positive pulse (U) does not induce any switching since the sample is already polarized in this direction and, thus, the current measured allows to retrieve the only non-ferroelectric contributions, as shown by the yellow line in figure 4.7b. The same happens for the fourth (N) and fifth (D) negative pulses to characterize the negative polarization state. Thus, one can subtract the current measured for pulses with the same polarity ($I_P$ – $I_U$, $I_N$ – $I_D$) to observe only the ferroelectric contribution ($I_{FE^+}$ and $I_{FE^-}$). The final

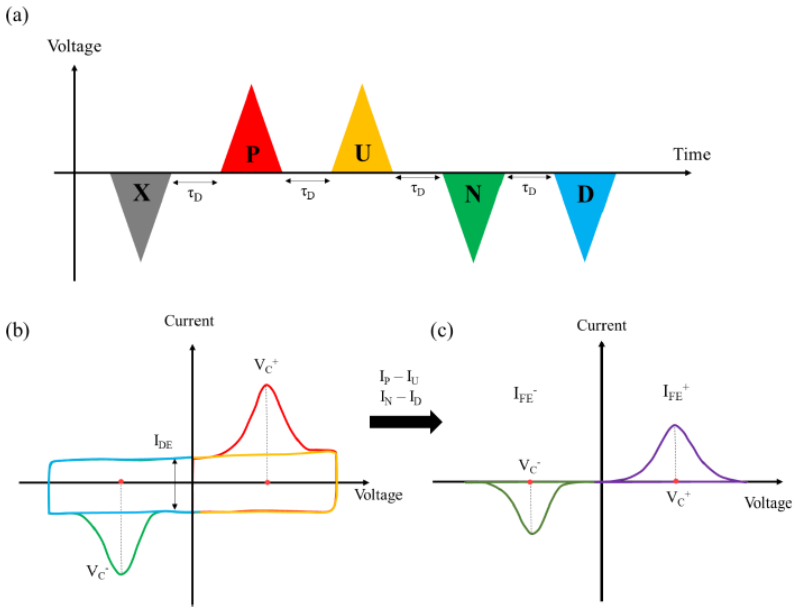


Figure 4.7: (a) Sequence of pulses applied to the sample using the PUND technique. (b) Representation of the current response corresponding to each voltage pulse. (c) Final I-V curves obtained by $I_P - I_U$ and $I_N - I_D$. The only current contribution visible is related to ferroelectric switching [72].

I-V curve is sketched in figure 4.7c, and its integration in time gives rise to the polarization curve $P$ of the system as described by the relation 4.17:

$$P = \frac{\int_{t_0}^{t_0+\Delta t} I_{FE} \cdot d\tau}{A} \tag{4.17}$$

where $A$ [m$^2$] is the section area of the capacitor junction, while $\Delta t$ is the time over which the ferrolectric charge displacement occurs. Since the N pulse is used to switch the ferroelectric layer, while the D pulse is used to read the non-ferroelectric contributions, once the PUND measurement is terminated, the ferroelectric layer will go to its remanence polarization state, which polarity is determined by the sign of the last N pulse.

# 5 | Co/HZO thin film magnetic characterizations

In this chapter, we study the magnetic properties of Co/HZO thin films fabricated in collaboration with the Fraunhofer-Gesellschaft Institute. The stacks of the samples fabricated are shown in the table 5.1. The goal of this study is to characterize magnetically the thin films to understand which one presents the best magnetic configuration that would maximize the magnetoelectric coupling at the Co/HZO interface, the main focus of our scientific investigation. Specifically, we are interested in a sample that has a perpendicular magnetic anisotropy (PMA). As we discussed in the sections 2.1.5 and 2.2.3, since PMA is caused by interface effects, we expect that a possible ME coupling, which is also a surface effect, will be maximized. For a complete characterization analysis, we proceed with:

- the identification of sample easy and hard axis through VSM measurements;
- an in-plane magnetic anisotropy characterization for the samples showing an in-plane easy axis with the angle-resolve longitudinal MOKE that we developed.

## 5.1. Easy and hard axes characterizations

The in-plane and out-of-plane VSM magnetic characterizations for the samples C10, C3 and C1 (see table 5.1) are shown respectively in the figures 5.1a, 5.2a and 5.3a. Coherently with the theory (see section 2.1.4), the samples C10 and C3 present the easy axis along the

| Sample | Stack |
|---|---|
| **C10** | p-Si/TiN(10)/HZO(10)/Co(10)/Pt(5) |
| **C3** | p-Si/TiN(10)/HZO(10)/Co(3)/Pt(5) |
| **C1** | p-Si/TiN(10)/HZO(10)/Co(1)/Pt(5) |

Table 5.1: HZO/Co multilayers systems for magnetic characterizations.

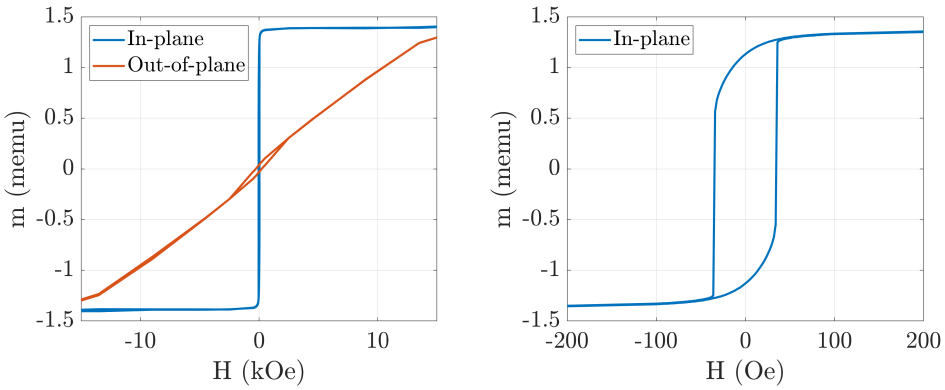


(a) Easy vs Hard axis response.

(b) Easy axis response around the $H$ origin.

Figure 5.1: C10 sample VSM in-plane and out-of plane magnetic characterizations.

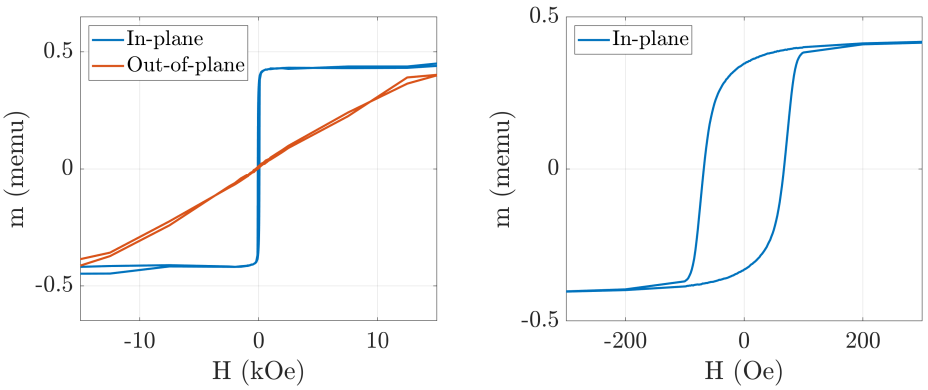


(a) Easy vs Hard axis response.

(b) Easy axis response around the $H$ origin.

Figure 5.2: C3 sample VSM in-plane and out-of plane magnetic characterizations.

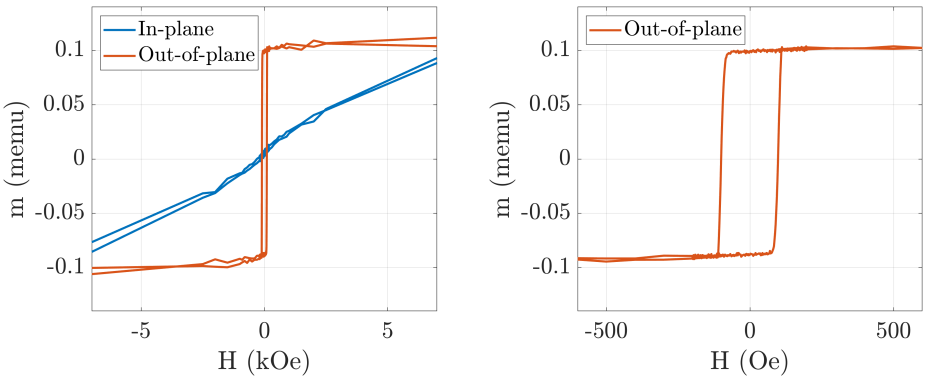


(a) Easy vs Hard axis response.

(b) Easy axis response around the $H$ origin.

Figure 5.3: C1 sample VSM in-plane and out-of plane magnetic characterizations.

thin film plane. On the opposite, the sample C1 is the only one to show an out-of-plane easy axis. As we discussed in the subsection 2.1.5, the presence of PMA is related to:

- the small Co thickness (1 nm), which favors surface magnetocrystalline anisotropy effects at the Co/HZO interface;
- post-thermal annealing treatments after the materials deposition process meant to favor the arrangement of atoms at the interface to maximize the PMA.

The samples C3 and C10 could not display PMA because as a magnetic thin film gets thicker, bulk and shape anisotropy effects become dominant, forcing the magnetization to remain confined along the film plane. A similar trend was recognized by Tudu *et al.* [77] in a Co/Pt multilayer system with Co presenting PMA for thicknesses below the 0.4 nm. The figures 5.1b, 5.2b and 5.3b display the magnetization curves in the restricted range zoomed around the origin of the $H$ field to evidence the hysteretic behaviors along the easy axes for samples C10, C3 and C1. As we discussed in the chapter 4.2, These data can be used to obtain different quantitative magnetic information about the magnetic layer. Moreover, from the saturation magnetization moment $m_s$ retrieved by the VSM, we can calculate the thickness of the layer $t$ with the relation (5.1):

$$t = \frac{m_s \cdot \gamma}{M_s \cdot S} \tag{5.1}$$

where $\gamma = 10^{-3} A \cdot m^2$ is a conversion factor to pass from emu to A/m units, and S $[m^2]$ is the area of the plane section of the magnetic layer. Taking $M_s = 1.44 \cdot 10^6$ A/m for Cobalt and S = 1 $cm^2$, the magnetic parameters evaluated from the easy axis magnetic curves for the samples C10, C3 and C1 are shown in the table 5.2.

| **Sample** | Easy axis | $m_s$ [memu] | $H_c$ [Oe] | $m_r/m_s$ | $t$ [nm] |
|---|---|---|---|---|---|
| **C10** | IP | 1.4 | 34.4 | 0.8 | 9.6 |
| **C3** | IP | 0.4 | 63.5 | 0.82 | 2.7 |
| **C1** | OOP | 0.1 | 101.2 | 0.93 | 0.7 |

Table 5.2: HZO/Co multilayers VSM magnetic parameters.

From the approximated relation (5.1), we were able to retrieve the thickness values of the Cobalt layers in good agreement (with a maximum discrepancy of 0.4 nm) with their nominal values (see table 5.1).

## 5.2. In-plane anisotropies characterizations

To complete our magnetic characterizations, we investigated the presence of in-plane anisotropies for the C10 and C3 samples. The angular in-plane longitudinal MOKE magnetic characterizations, obtained by rotating the sample with an angle step of 10° from 0° to 360°, are shown in the figures 5.4a and 5.4b. Figure 5.5a and 5.5b display the polar plots of the coercive fields $H_c$ and the $m_r/m_s$ for the C10 and C3 samples. The results we found show perfect examples of magnetic isotropic samples defined by an easy-plane anisotropy, as we discussed theoretically in the subsection 2.1.2. We notice the different response regarding the in-plane anisotropy measurements for the iron film presented in the section 4.1.5. The high isotropicity of the sample is due to a deposition process of the magnetic material. Alameda *et al.* show that obliquely deposited cobalt thin films can present in-plane anisotropy easy axes [3]. Studying a cobalt film deposited via e-beam evaporation, with an incidence angle of the vapor beam regarding the normal surface of the sample of 60°, they found cobalt films magnetically isotropic along the film plane.

## 5.3. Conclusions

The magnetic characterizations we did on the Co/HZO films showed that:

- the cobalt layer presents an isotropic magnetic behavior along the film plane for thickness $t \geq 3$ nm;
- the 1 nm thick Co layer presents PMA.

Among the three different Co/HZO material stacks, the sample that is the most promising to show magnetoelectric coupling at the Co/HZO is the sample C1. Since the study of the presence of magnetooptical coupling finds its motivations in the field of research on alternative systems for memory device applications, the next step will be to proceed with the fabrication and characterization of micro devices based on the sample C1 multilayer structure.

To study the magnetic property and the magnetoelectric coupling in the new Co/HZO device system, we will employ the $\mu$MOKE setup detection system, which is at the core of this thesis work. The next chapter will be dedicated to the explanation of the characteristics and performances of the $\mu$MOKE system we developed.

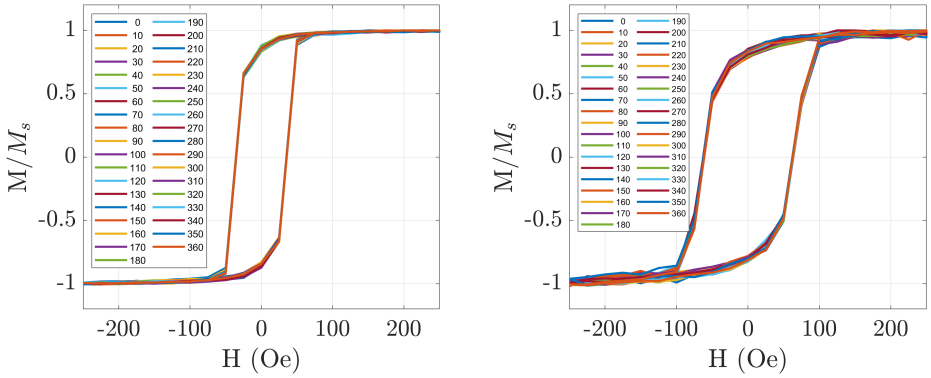


(a) C10 sample. (b) C3 sample.

Figure 5.4: In-plane magnetic anisotropy MOKE characterizations.

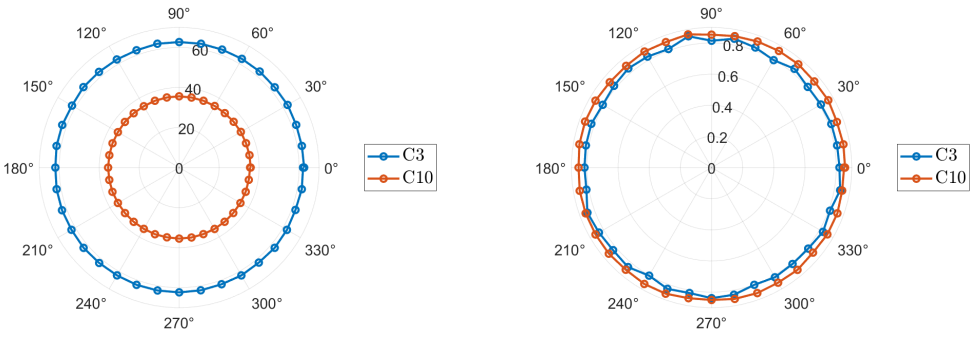


(a) $H_c$ (Oe) vs Angle (deg). (b) $m_r/m_S$ vs Angle (deg).

Figure 5.5: Coercive fields and $m_r/m_S$ polar plots for samples C3 and C4 obtained by longitudinal MOKE angle scans.

# 6 | $\mu$MOKE characterization

When dealing with magnetic systems which properties change on a micrometric scale, magnetic characterizations cannot be done anymore with a standard MOKE setup, as the one presented in the section 4.1.1. That is for two reasons:

- **Low spatial sensitivity**: a MOKE system is not able to distinguish locally between different magnetic configurations if the light spot size is higher than the dimension of the magnetic domain or feature of interest;
- **Sample size**: when studying micro magnetic devices (e.g. magnetic hall bars and microcapacitors) due to their small size, it is not easy to understand which region we are pointing at with the light source.

These problems can be solved by introducing an optical objective, which has a dual function: it can focus the laser beam spot, thus increasing the spatial resolution of the incident light, and, exploiting the principle of a microscope, it can realize a magnified image of the sample in order to understand which region is invested by the light. Whenever an objective is introduced, we talk about a $\mu$MOKE system.

In this chapter, we present a $\mu$MOKE system that not only allows spatially resolving of the magnetization of the sample, but manages to do it with high sensitivity. High sensitivity is essential when studying systems with small magnetic signals. To increase the sensitivity of our $\mu$MOKE we used a balanced detector which functioning is based on a differential light acquisition system, capable of rejecting most of the noise and disturbances affecting the light signal. Furthermore, the high sensibility of the detector allows performing measurements even without a light modulation stage. The system we developed also allows:

- **High spatial resolution**: when working with a 100x objective, the setup spatial resolution can be improved down to 5 $\mu$m;
- **Magnetic characterizations versability**: the setup is able to perform both longitudinal and polar magnetic characterizations. That is an important feature because micromagnetic systems, due to their reduced size and/or due to interfaces effects,

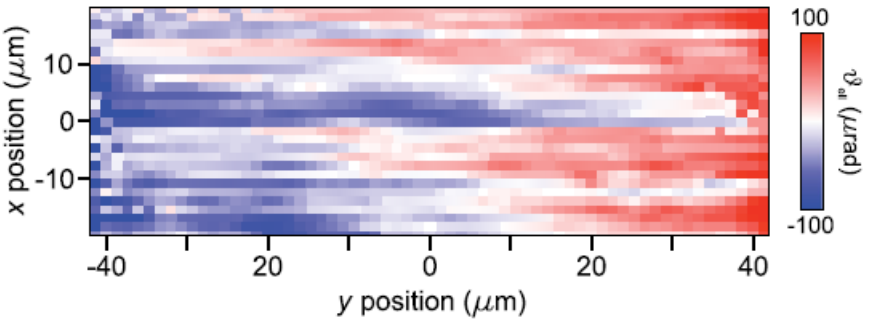


Figure 6.1: Kerr ellipticity spin accumulation map across a $n$-doped Ge channel [17].

could present at the same time in-plane and out-of-plane magnetization components.

This $\mu$MOKE system could be used to investigate phenomena, which require high signal sensitivity, such as:

- the magnetic properties of microstructures, e.g., nanoflake based magnetic heterostructures [47];
- the magnetic anisotropy field in nanostructured ferromagnetic thin film for the characterization of spin-orbit-torque-induced magnetization dynamics with electric current injection [84];
- the domain wall structure and dynamics driven by spin-orbit-torques in racetrack structures [80];
- the thermal and electrical generation of spin currents, spin accumulation and spin-to-charge conversion experiments in microdevices. [17, 56]. Figure 6.1 depicts the spin accumulation map over a $n$-doped Ge micro channel, measured with a polar $\mu$MOKE system using a balanced photodiode. The spin accumulation map was obtained by measuring the Kerr ellipticity $\theta_{ell}$ signal, which amplitude depends on the sign of the spins and their density $n_s$ inside the Ge channel [17].

## 6.1. Experimental setup

Figure 6.2 shows a picture of the final setup together with the corresponding scheme, where all the components are marked by respective abbreviations and the directionality of light (**k**-vector) is given by arrows.

### 6.1.1. Laser optical path and detection

A laser diode $L$ provides light at 515 nm with a 500 $\mu$m spot size. We chose a green laser because it was already used and employed in $\mu$MOKE systems to characterize spintronics devices and phenomena [56]. The laser light undergoes the following optical steps:

- since the laser diode is mounted on a mount fixed to the optical table, two dielectric mirrors $M_1^1$ and $M_1^2$ were placed to precisely align the laser beam along the optical paths of the setup and to guide the light to a polarizer $P$;
- a chopper $C$ is placed between the laser diode and the $M_1^1$ mirror to allow light intensity modulation;
- the polarizer $P$ provides a $s$ polarization (perpendicular to the optical table) to the incoming light, which is then transmitted toward a 50:50 beam splitter $BS^1$;
- an optical iris $I^1$ is placed in front of the polarizer $P$ to control the spot size of the laser;
- the beam splitter $BS^1$ transmits half of the light intensity, which is blocked by a beam block $BB$, and reflects the other half to a dichroic mirror $M_2$;
- in the middle between $BS^1$ and $M_2$, an optical iris $I^2$, which aperture is set at the laser beam height, and it is used to constantly have a check that the light rays reflected by the $BS^1$ are aligned with respect to the optical components;
- the dichroic mirror $M_2$, which only reflects light below 567 nm as the green laser light we use, directs the laser light toward an objective lens $OL$. $M_2$ is also used to allow the integration of a microscope system, which functioning, and optical components are discussed in the subsection 6.1.2;
- an objective lens $OL$ is used to focus the laser light onto the sample $S$. With a beam spot diameter of 500 $\mu$m, the light can be focused by a set of 10x, 60x and 100x objective lenses, increasing the $\mu$MOKE system spatial resolution to 50 $\mu$m, 9 $\mu$m and 5 $\mu$m respectively.
- the sample $S$ is mounted on a sample holder that can be translated by a micrometric stage along the $x$,$y$,$z$ directions.
- The laser light is reflected by the sample. After a series of simple reflections, the sample is the first component that introduces a change in the polarization state of the light after the polarizer $P$. The interaction between the light and the sample is discussed in the subsection 6.1.4. Then, the light is:

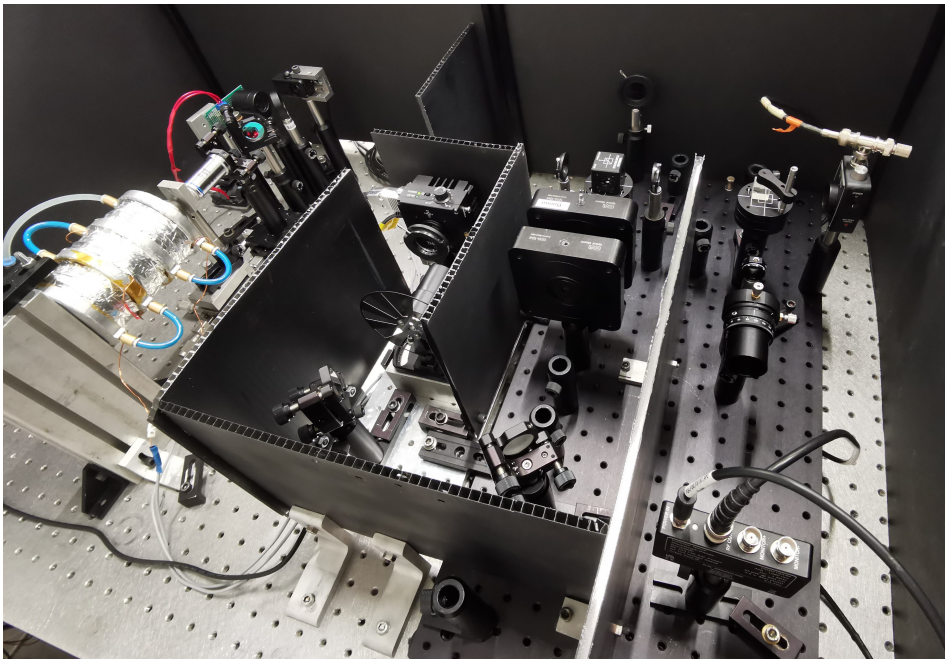

(a)

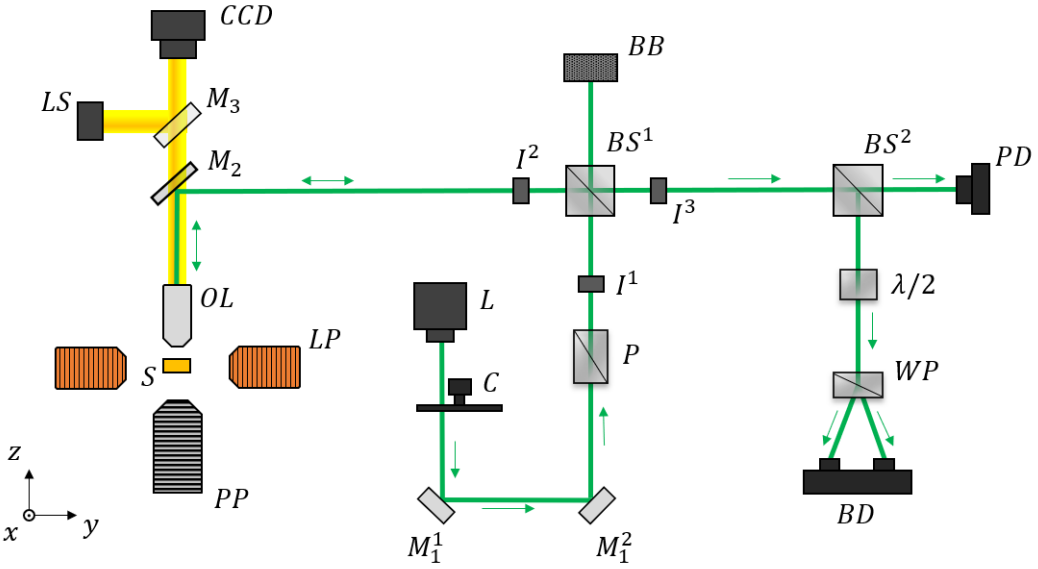


(b)

Figure 6.2: Picture of the final $\mu$MOKE setup (a) and corresponding scheme with relative components (b). The $\mu$MOKE setup in the figure (a) is set in a polar configuration.

  - transmitted again through the objective;
  - reflected by $M_2$ to $BS^1$;
  - transmitted by $BS^1$ and sent to a second 50:50 beam splitter $BS^2$.

- along the optical path in the middle between $BS^1$ and $BS^2$, an optical iris $I^2$, which aperture is set at the laser beam height, is used to constantly have a check that the light rays reflected by the sample are aligned regarding the optical components;
- the beam splitter $BS^2$ transmits half of the laser signal to a photodiode $PD$ and reflects the other half to a half-wave plate $\lambda/2$. The beam splitter $BS^2$ was placed to allow use of the photodiode $PD$.
- the photodiode $PD$ is used specifically to measure the power of light reflected by the sample, irrespectively of its polarization, to quantitatively evaluate the Kerr rotation $\theta_K$ amplitude (in rads), as we will further discuss in the subsection 6.1.5 and in the appendix A. The photodiode $PD$ is necessary since this operation cannot be done by the balanced photodiode $BD$ alone. The measurement of the light intensity to obtain the rotation can be done without a light modulation stage;
- the half-wave plate $\lambda/2$, with optical axis at 22.5° regarding the $x$ axis, is used to rotate the light polarization by 45° regarding the $s$ ($x$) direction;
- the light transmitted by the wave plate is sent to a Wollaston prism $WP$, which separates the $s$ and $p$ light polarization components;
- the two $s$ and $p$ separated light components are measured by a balanced photodiode $BD$, which generates an output signal proportional to the difference between the two light polarization optical powers (6.1):

$$P_{BD} = P_s - P_p \tag{6.1}$$

where $P_s$ and $P_p$ are the optical powers regarding the $s$ and $p$ polarization component of the light, reflected by the sample, entering the Wollastone prism. Thus, we have two possibilities:

1. if the sample reflecting the light is non-magnetic, no Kerr rotation is induced, and the light polarization is preserved in the $s$-state established by the polarizer $P$. When passing through $\lambda/2$, the $s$-polarization will be rotated by 45°, causing the light a new linear polarization state where the $s$ and $p$ components have same amplitude, with equal optical powers $P_s = P_p$, determining a

$P_{BD} = 0$ signal measured by the balanced photodiode;

2. if the sample is magnetic, the polarization of the reflected light will gain a Kerr rotation. As a consequence, when the reflected light polarization is rotated by 45° by the $\lambda/2$, a slight unbalance between the $s$ and $p$ state is introduced, which is reflected in their respective optical powers, such that $P_s \neq P_p$. Thus, the difference between the $s$ and $p$ optical powers (6.1) will determine a non zero balanced detector signal. In the subsection 6.1.4, we demonstrate that $P_{PB}$ is proportional to the Kerr rotation $\theta_K \propto M$.

The ability of the balancing detector to measure the differential signal (6.1) allows it to remove the contributions and background disturbances equally present in the $s$ and $p$ power signals separated by the Wollastone prism. Furthermore, since the detector is equipped with a high-speed and low-noise transimpedance amplifier [76], it is capable of amplifying small signals, further increasing its sensitivity.

### 6.1.2. Microscope system

The direct observation of sample for the laser positioning is done with the microscope system (shown in figure 6.3a) realized with:

- a LED light source $LS$ is used to illuminate the sample. Since the LED light was defined by a divergent beam, a lens was placed in front of the LED source to collect the maximum amount of light in the microscope system;
- a 50:50 coupling mirror $M_3$ is used to reflect half of the LED light to the dichroic mirror $M_2$;
- the dichroic mirror $M_2$, which only reflects light below 567 nm, transmits the LED light wavelength components above 567 nm to the objective;
- the objective is used to focus the LED light onto the sample;
- the reflected light image of the sample is transmitted again through the objective;
- the red light components of the sample image are transmitted by the dichroic mirror to the 50:50 coupling mirror;
- the coupling mirror $M_3$ transmits the sample image to a camera, where the image is detected.

The ability of the dichroic mirror to filter the light components below 567 nm has allowed the use of LED light, which, as it is never transmitted along the optical path leading to

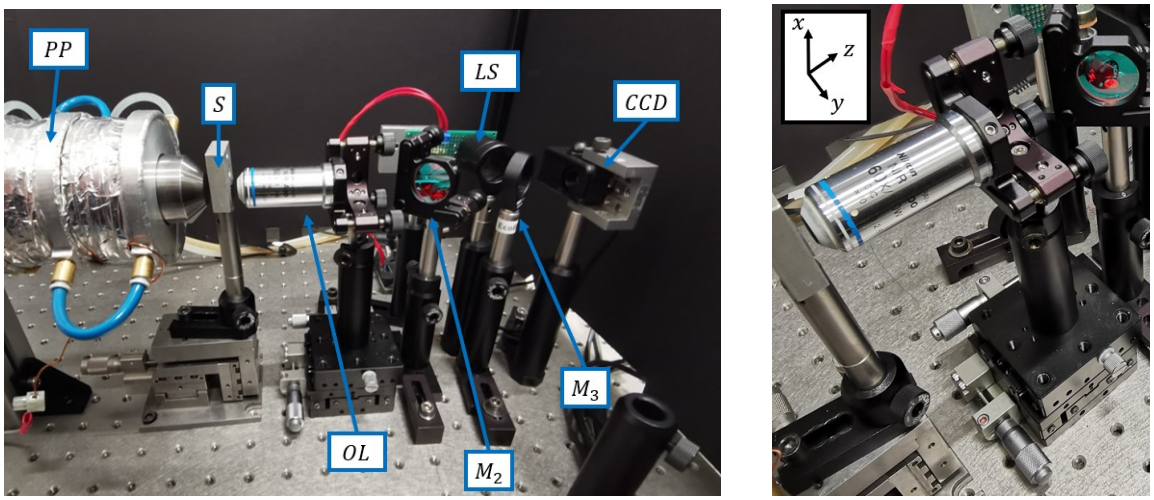


(a) (b)

Figure 6.3: (a) Picture of the $\mu$MOKE microscope system with relative components (b) Overview of the objective movable with a micrometric stage along the $y$, $z$ directions.

the detectors, does not cause disturbances during the measurement.

### 6.1.3. Longitudinal and polar measurement configurations

The control of the magnetization of the sample $S$ during the measurements is carried out by magnetic poles around the sample stage:

- the magnetic poles $LP$ are used to generate magnetic fields along the in-plane $y$ direction, to perform longitudinal characterizations;
- the magnetic poles $PP$ is used to generate magnetic fields along the out-of-plane $z$ direction, to perform polar characterizations. We use only one pole so as not to interfere with the position of the objective.

As we discussed in the subsection 3.3.1, longitudinal MOKE measurements cannot be realized if the laser is at normal incidence regarding the sample surface. For this reason, the objective lens can longitudinally shift along the $y$-axis via a micrometric stage (as illustrated in the figure 6.3b), enabling us to displace the beam off-center in the objective lens. This induces a non-normal focus of light onto the sample, consequently allowing us to switch from polar MOKE to longitudinal MOKE geometry (see subsections 3.3.1 and 3.3.2), as sketched in the figure 6.4.

When working in both longitudinal and polar configurations, the objective lens $OL$ can be exposed to the magnetic field generated by the magnetic polar extensions $PP$ and $LP$.

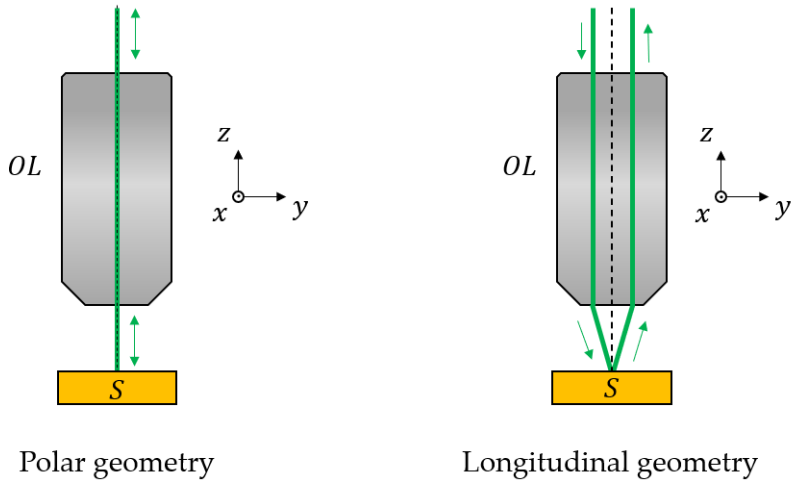


Figure 6.4: Scheme of the $\mu$MOKE polar and longitudinal MOKE geometries obtained by shifting the objective lens along the $y$ direction.

Depending on the MOKE geometry we could have to deal with two spurious contributions of magneto-optical origin:

- **Faraday effect**: when light is transmitted through a transparent medium, such as the objective lenses, with a magnetic field applied parallelly to the light **k**-vector, as in a polar MOKE configuration, the transmitted light polarization will be altered as a function of the magnetic field. This is known as the Faraday effect, which therefore constitutes a background regarding the Kerr rotation measurement. The dependence of the former on the magnetic field is linear, and thus it can be removed, once the measurement is completed, by a simple linear subtraction [31];
- **Voigt effect**: if light propagates through a transparent medium, such as the objective lenses, with a magnetic field applied perpendicularly to the light **k**-vector, its polarization state will also be altered as a function of the magnetic field. This is known as the Voigt effect, which can also constitute a signal background, which dependence on the magnetic field is quadratic as a first order approximation. Eventually, this non-linear quadratic background can be removed by a quadratic non-linear fit once the measurement is complete [31]. This effect can be present both in the polar and longitudinal geometries, depending on the magnetic field lines generated by the poles and the position of the objective lens regarding the poles.

### 6.1.4. Balanced detector magnetic signal

If we refer to the coordinate system in Figure 6.5, the electric field can be described as a vector with two components $p$ and $s$, parallel and perpendicular to the $yz$ plane of

incidence. Using as mathematical vector bases $\mathbf{e}_s = \begin{pmatrix} 0 \\ 1 \end{pmatrix}$ and $\mathbf{e}_p = \begin{pmatrix} 1 \\ 0 \end{pmatrix}$ to describe $s$ and $p$ waves, a generical electric field is given by the linear combination of $\mathbf{e}_s$ and $\mathbf{e}_p$ basis as shown by the relation (6.2):

$$\mathbf{E} = E_s\mathbf{e}_s + E_p\mathbf{e}_p = \begin{pmatrix} E_p \\ E_s \end{pmatrix} \tag{6.2}$$

By referring to $\alpha$ as the angle between the optical axis of a generic optical component and the $yz$ incident plane, the optical matrices describing the optical polarizer $P$ and the $\lambda/2$ waveplate, located before the Wollastone prism, are described by the relations (6.3) and (6.4) [49]:

$$\mathbf{A} = \begin{pmatrix} \cos^2\alpha & \sin\alpha\cos\alpha \\ \sin\alpha\cos\alpha & \sin^2\alpha \end{pmatrix} \tag{6.3}$$

$$\mathbf{\Lambda} = i\begin{pmatrix} \cos 2\alpha & \sin 2\alpha \\ \sin 2\alpha & -\cos 2\alpha \end{pmatrix} \tag{6.4}$$

To induce a $s$-polarization for the green laser light, the polarizer $P$ will be defined by an $\alpha = \pi/2$. To rotate the light polarization by 45° with respect to the $s$-direction, the $\lambda/2$ waveplate optical axis has to be positioned at 22.5° with respect to the $x$-direction, which implies $\alpha = 3\pi/8$. Then, the polarizer, the waveplate and the Fresnel reflection matrixes are described by the relations (6.5), (6.6) and (6.7), respectively:

$$\mathbf{A} = \begin{pmatrix} 0 & 0 \\ 0 & 1 \end{pmatrix} \tag{6.5}$$

$$\mathbf{\Lambda} = \frac{i}{\sqrt{2}}\begin{pmatrix} -1 & 1 \\ 1 & 1 \end{pmatrix} \tag{6.6}$$

$$\mathbf{R} = \begin{pmatrix} r_{pp} & r_{ps} \\ r_{sp} & r_{ss} \end{pmatrix} \tag{6.7}$$

The electric field $\mathbf{E}_L$ coming out of the laser source $L$ can be described by the relation (6.2). The laser electric field $\mathbf{E}_0$ coming out from the polarizer $P$ is given by the relation (6.8):

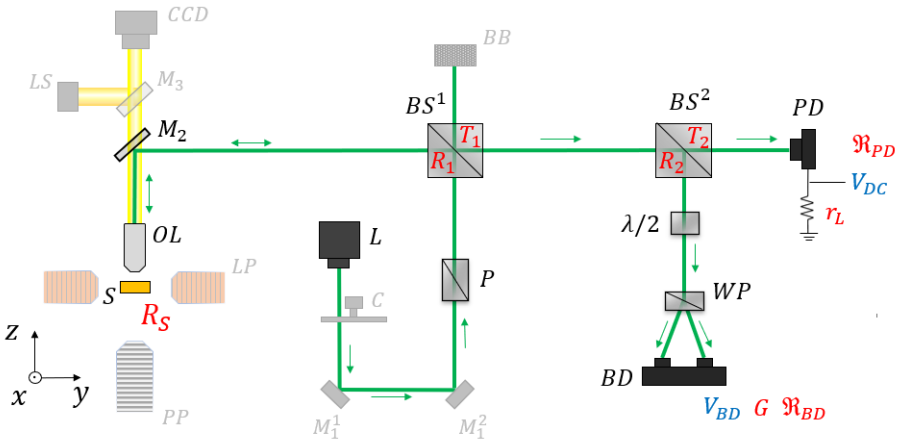


Figure 6.5: Optical path and detection setup for the laser light in the $\mu$MOKE scheme.

$$\mathbf{E}_0 = \mathbf{A} \cdot \mathbf{E}_L = \begin{pmatrix} 0 & 0 \\ 0 & 1 \end{pmatrix} \cdot \begin{pmatrix} E_p \\ E_s \end{pmatrix} = \begin{pmatrix} 0 \\ E_0 \end{pmatrix}. \tag{6.8}$$

Then, the electric field $\mathbf{E}_{WP}$ at the wollaston prism is obtained by the relation (6.9):

$$\mathbf{E}_{WP} = \begin{pmatrix} E_p^{WP} \\ E_s^{WP} \end{pmatrix} = \mathbf{\Lambda} \cdot \mathbf{R} \cdot \mathbf{E}_0 = i\frac{E_0 r_{ss}}{\sqrt{2}} \begin{pmatrix} -\frac{r_{ps}}{r_{ss}} + 1 \\ \frac{r_{ps}}{r_{ss}} + 1 \end{pmatrix} \tag{6.9}$$

The $s$ and $p$ components of the relation (6.9) are separated by the wollastone prism ($WP$) and directed to the two balanced photodiode ($BD$) different active regions, each dedicated to detect one of the two components. The two active regions will measure two $P_s$ and $P_p$ power signals described by the relations (6.10) and (6.11):

$$P_s = \frac{1}{2} A_L c \epsilon_0 |\mathbf{E}_{WP} \cdot \mathbf{e}_s|^2 = \frac{P_0 |r_{ss}|^2}{2} |\frac{r_{ps}}{r_{ss}} + 1|^2 \tag{6.10}$$

$$P_p = \frac{1}{2} A_L c \epsilon_0 |\mathbf{E}_{WP} \cdot \mathbf{e}_p|^2 = \frac{P_0 |r_{ss}|^2}{2} |-\frac{r_{ps}}{r_{ss}} + 1|^2 \tag{6.11}$$

where $P_0 = \frac{1}{2} A_L c \epsilon_0 E_0$ is the optical power of the laser beam after passing through the polarizer $P$, and $A_L$ is the laser beam section area. The ratio between $r_{ps}$ and $r_{ss}$ is equal to the complex Kerr angle $\Theta_K$ (6.12) [86]:

$$\Theta_K = \theta_K + i\epsilon_K \tag{6.12}$$

By substituting (6.12) in the equations (6.10) and (6.11), we obtain the new relations (6.13) and (6.14):

$$P_s = \frac{P_0|r_{ss}|^2}{2}[(1+\theta_K)^2 + \epsilon_K^2] \tag{6.13}$$

$$P_p = \frac{P_0|r_{ss}|^2}{2}[(1-\theta_K)^2 + \epsilon_K^2] \tag{6.14}$$

Finally, the output signal from the detector $I_{BD}$ is determined by the difference between (6.13) and (6.14) which is equal to the relation (6.15):

$$P_{BD} = 2R_S P_0 \theta_K \tag{6.15}$$

where $R_S = |r_{ss}|^2$ is the fraction of incident $s-$light reflected by the surface of the magnetic sample $S$. However, we still did not count the power transmittivity and reflectivity affecting the power $P_0$ exiting the polarizer $P$, caused by non-polarizing beam splitters $BS^1$ and $BS^2$. Thus, it becomes necessary to reformulate the relation (6.15)$P_{BD}$ using the expression (6.16):

$$P_{BD} = 2R_1 T_1 R_2 R_S P_0 \theta_K \tag{6.16}$$

where $R_i$, $T_i$ are the reflectivity and trasmittivity of the beam splitter $BS^i$, with $i = 1, 2$. The intensity reflectivity of the dichroic mirror $M_2$, which reflects twice the light, was not considered since ideally it completely reflects the laser light at 515 nm, while the objective lens $OB$ was supposed to have a trasmittivity equal to 1.

Thus, it holds that $I_{BD} \propto \theta_K \propto M$, which implies that with this optical configuration it is possible to resolve magnetic signals. These calculations would be still valid in an optical configuration in which we were performing a signal modulation with a chopper, since it provides a time modulation of the electric field amplitude without affecting the polarization of light.

### 6.1.5. Kerr rotation evaluation

Working in an optical configuration as the one shown in the section 6.1.4, from a balanced photodiode signal (6.15), we can retrieve the induced Kerr rotation $\theta_K$. By referring to the setup scheme in figure 6.5, it is possible to demonstrate that $\theta_K$ can be experimentally

evaluated with the formula (6.17) (see apprendix A):

$$\theta_K = \frac{\Re_{PD}(\lambda)}{\Re_{BD}(\lambda) \cdot G} \frac{T_2}{R_2} \frac{r_L}{2V_{DC}} V_{BD} \tag{6.17}$$

where:

- $\Re_{PD}(\lambda)$ $[A/W]$ is the responsivity of the photodiode PD;
- $r_L$ $[\Omega]$ is the load resistance of photodiode PD;
- $\Re_{PD}(\lambda)$ $[A/W]$ is the responsivity of the balanced detector $BD$;
- $G$ $[V/A]$ is the transimpedance gain of the balanced detector $BD$;
- $T_2$ and $R_2$ are the trasmittivity and reflectivity of the 50:50 beam splitter $BS^2$;
- $V_{DC}$ $[V]$ is the output signal of the photodiode $PD$;
- $V_{BD}$ $[V]$ is the output signal of the balanced photodiode $BD$ .

### 6.1.6. Laser diode signal stability

In this subsection, we present the intensity stability of the laser diode used in this $\mu$MOKE setup. Our laser is based on a Thorlabs L515A1 green laser diode, mounted on a Thorlabs LDM9T laser mount, which light emission can be controlled by a Thorlabs LDC202C controller. The LDM9T laser mount is designed to temperature control the laser diode to increase the thermal laser signal stability [75]. The LDC200C Laser Diode controller is a power controller for the laser diode [74]. The LDC200C controller allows driving the laser diode in two possible modes:

- **Constant Current** (CC): the current to the laser is fixed at the prescribed level;
- **Constant Power** (CP): the internal photodiode integrated into the L515A1 laser diode is used to actively stabilize the laser's output power, which is adjusted by a feedback circuit.

In the figure 6.6, we plot the standard deviation of the voltage signal induced by light in a photodiode at the exit of the LDM9T laser mount, as a function of the measuring time for the constant current and power modes. These data were obtained with a Thorlabs DET100A2 silicon photodiode connected to a multimeter. Despite the presence of systems for thermalization of the laser and control of the diode power stability, the signal drift that we observe for the two modes could be attributed to a possible faulty response on

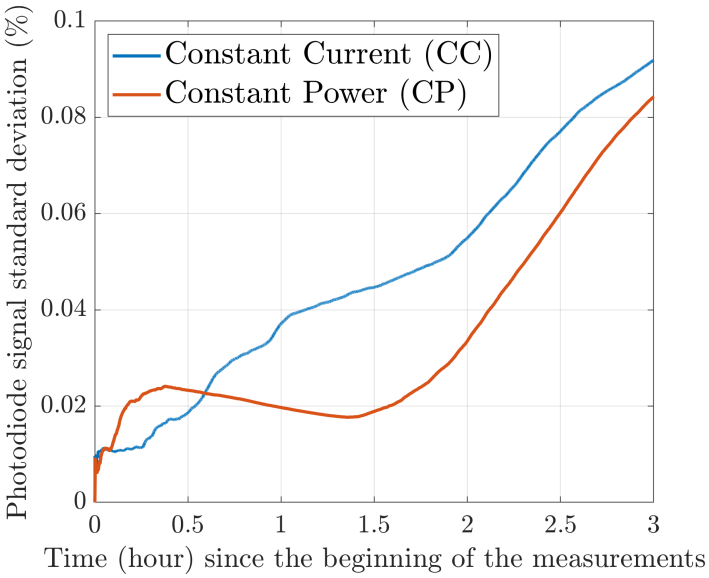


Figure 6.6: Standard deviation of the L515A1 laser light voltage signal measured by a DET100A2 photodiode as a function of time when controlled by the LDC200C controller operating in constant current and power modes.

the part of the diode itself. Still, over three hours of measurement, both the LDC200C control modes guarantee a signal error below the 0.1 %.

## 6.2. Experimental applications

## 6.3. Setup validation

In this section, we present the experimental characterizations and data noise analysis for the $\mu$MOKE setup on thin films and patterned reference samples, in the longitudinal and polar configurations. We compare the analyses on hysteresis data obtained by modulating the signal with an optical chopper (531 Hz) and without a modulation stage. We evaluate the ability of the $\mu$MOKE system to resolve magnetic signals in longitudinal and polar configurations, both for thin film systems and for patterned structures. Characterizations were done on the following samples:

- **Sample FI**: 10 nm thick iron film, epitaxially grown on a 1 $cm$ $\times$ 1 $cm$ MgO(100) substrate, presenting an in-plane magnetic cubic anisotropy along the diagonals of the sample;
- **Sample MI**: micrometric Hall bar system with 10 nm thick CoFeB layer presenting an in-plane easy axis along the longidudinal channel of the Hall bar;

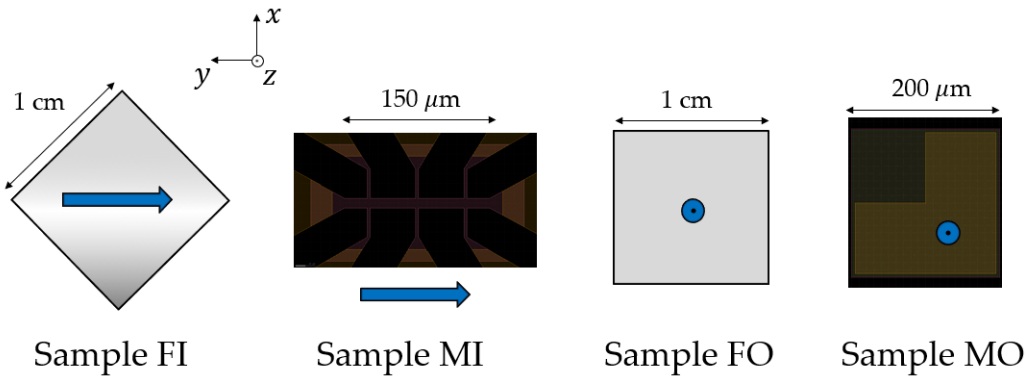


Figure 6.7: Scheme of the in-plane ($yx$ plane) sections of samples, their dimensions, and their magnetic easy axes (blue arrows).

| Sample | Stack | Easy axis |
|---|---|---|
| **FI** | MgO/Fe(10) | IP |
| **MI** | $SiO_2$/CoFeB(10)/Ru(2) | IP |
| **FO** | p-Si/TiN(10)/HZO(1)/Co(1)/Pt(5) | OOP |
| **MO** | p-Si/TiN(10)/HZO(1)/Co(1)/Pt(5) | OOP |

Table 6.1: HZO/Co multilayers systems for magnetic characterizations (thicknesses in nm).

- **Sample FO**: 1 nm thick cobalt film, grown on 10 nm of HZO, presenting perpendicular magnetic anisotropy (PMA) due to the orbitals hybridization effects at the interface with the HZO oxide layer;
- **Sample MO**: a patterned structure nanofabricated from the sample FO.

Figure 6.7 sketches the in-plane ($yx$ plane) sections of samples, their dimensions, and their magnetic easy axes. The sample multilayer stacks are displayed in table 6.1.

The signal-to-noise ratio (SNR) parameter for a magneto-optical cycle measurement remains the one defined by the relation (6.18) introduced in the subsection 4.1.4.

$$SNR = \frac{\Delta}{\sqrt{\sigma_+^2 + \sigma_-^2}} \tag{6.18}$$

where $\Delta$ represents the hysteresis loop amplitude, evaluated as the difference between the mean values of the magnetic data distributions at positive and negative saturation, while

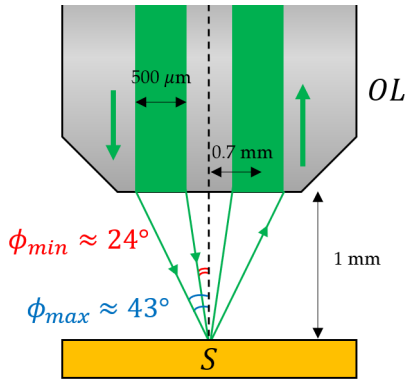


Figure 6.8: Light ray minimum and maximum angles of incidence working with a 100x objective lens, with 1 mm focal lenght, shifted by 0.7 mm regarding the laser beam and assuming a laser spot size diameter of 500 $\mu$m.

$\sigma_+^2$ and $\sigma_-^2$ are the standard deviations of the magnetization data sets at positive and negative saturation regime, respectively.

### 6.3.1. Longitudinal $\mu$MOKE characterizations

The longitudinal MOKE measurements were realized with the 100x objective. To set the system in the longitudinal MOKE configuration, the 100x objective lens axis was shifted regarding the laser beam by 0.7 mm, Assuming a laser spot size diameter of 500 $\mu$m entering the objective with a 1 mm focal lenght, we can estimate the angle of incidence of the focused beam rays onto the magnetic sample. We found that the light rays angle of incidence $\phi$ , from the closest and outer spot regions regarding the objective axis, is defined over the range $\phi \in [24°; 43°]$ as sketched in the figure 6.8.

When working with the 100x objective, it was observed that after starting a measurement, the system would experience a loss of focus overtime. This determined a worsening of the signal SNR, as the objective lens was not able anymore to focus the light in the optimal longitudinal (or polar) MOKE geometry configuration. As a result, we verified that it was possible to maintain the focus without a worsening of the SNR for up to 30 minutes, which allowed to complete approximately 40 single scan measurements.

#### Fe in-plane film characterizations

In this subsection, we present the longitudinal $\mu$MOKE measurements on sample FI (see table 6.1). The sample was mounted such that one of the easy axis was parallel to the direction of the $H$ field.

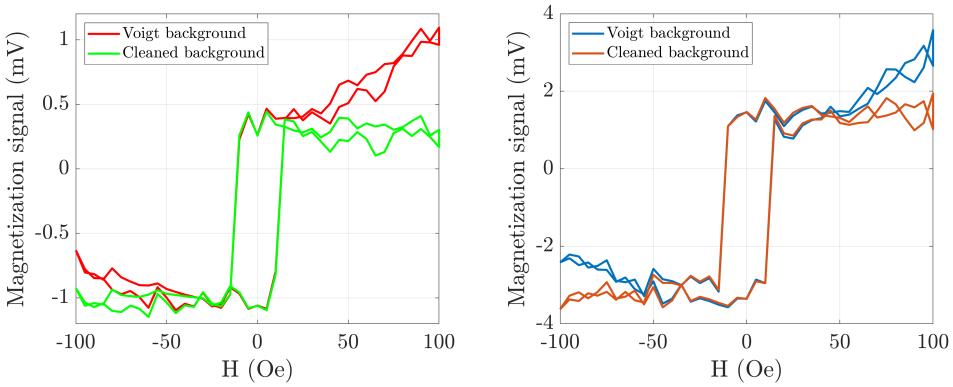


(a) Chopper (531 Hz). (b) No modulation.

Figure 6.9: Longitudinal raw single measurement data with and without Voigt background measured with (a) and without (b) chopper modulation stage for the Fe film.

We analyzed 40 hysteresis loop cycles, acquired with both modulated and unmodulated configurations, within 30 minutes, as discussed in the previous section. The data exhibited Voigt quadratic background contributions attributed to proximity of the objective lens to the magnetic poles, as discussed in section 6.1. The figure 6.9 compares the differences between a single raw loop measurement before and after the Voigt background subtraction. The SNR related to the hysteresis single scan signals, calculated after the quadratic background subtraction, with and without a modulation stage, is presented in the figure 6.10a. Since there is no distinction between measurements, we consider the constant trend of the SNR of the measured single loops as consistent. We obtain the SNR averages and standard deviations for single measurements:

- SNR $= 10 \pm 0.7$ with light modulation;
- SNR $= 11 \pm 2$ without modulation.

Within standard deviations, the SNR parameters for single measurements measured without and via chopper are equivalent. Then, we proceed with the analyses on the SNR when we average the single hysteresis loops, after having subtracted from each their own Voigt background. Figure 6.10b presents the SNR profile of averaged data as a function of the number of averages. An increase of the SNR as a function of the number of averages is what we indeed expect when averaging signals defined by the same noise contributions. The curves present the $\sqrt{N}$ polynomial improvement that we would expect by averaging $N$ noisy independent signals. The magnetic and rotation hysteresis data, obtained by averaging 40 single cycles, are shown in the figure 6.11. The normalization of the signals was done regarding the expectation value of the magnetization data at saturations. The openings of the cycles at saturations are attributable to a Voigt background, which could

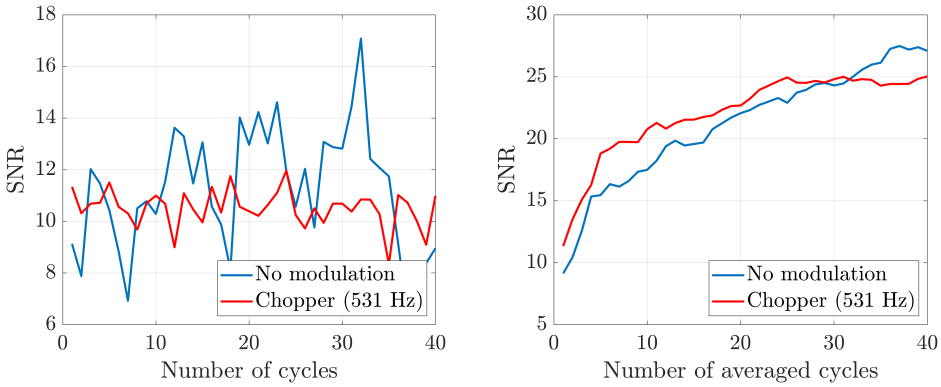


(a) (b)

Figure 6.10: SNR for the Fe film single hysteresis loops (a) and averaged loops (b) as a function of the average.

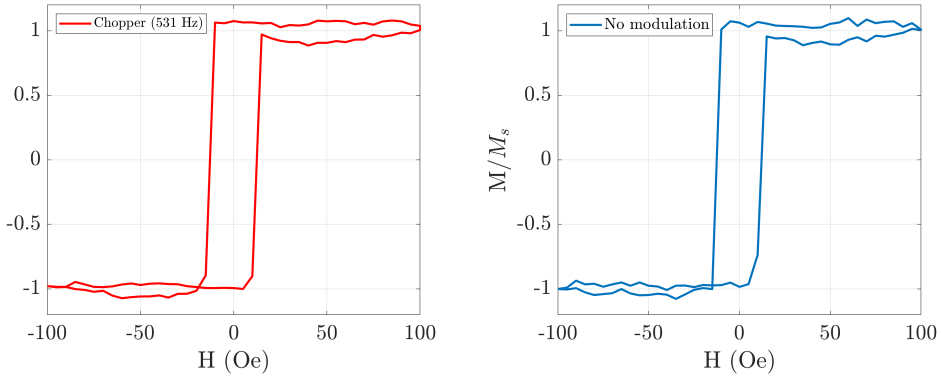


(a) Chopper (531 Hz). (b) No modulation.

Figure 6.11: Longitudinal $\mu$MOKE normalized measurements for the Fe film with (a) and without (b) chopper modulation, obtained by averaging 40 single cycles.

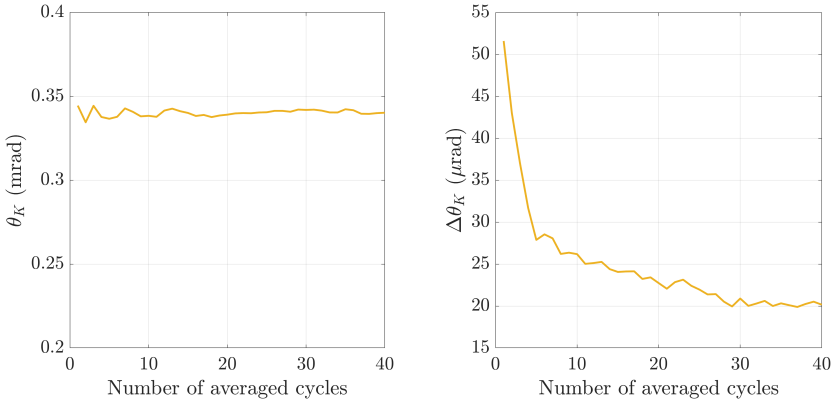


(a) (b)

Figure 6.12: Kerr rotation signal average (a) and resolution (b) at saturation ($|H| > 20$ Oe) as function of the number of averages for the Fe film.

| Modulation | $H_c$ [Oe] | SNR |
|---|---|---|
| **No** | 12.2 | 27 |
| **Chopper** | 12.4 | 25 |

Table 6.2: Fe film longitudinal $\mu$MOKE magnetic parameters.

not be eliminated by subtracting a polynomial curve.

We stress that the quality of the signal acquired with and without the modulation stage is similar, thanks to the amplifier differential system of the balanced photodiode. The iron thin film magnetic parameters calculated from the signals in the plots 6.11 are presented in the table 6.2. We calculate:

- $H_c = 12.2$ Oe $\pm$ 1 with modulation;
- $H_c = 12.4$ Oe $\pm$ 1 without modulation.

The coercive fields standard deviation bars were estimated from the data distributions of the coercive fields calculated by each single loop measurement. The expectation value and resolution of the Kerr rotation (in mrad) at saturation ($|H| > 20$ Oe) for the Fe film as a function of the number of averages are shown in the figure 6.12. The Kerr rotation presents a constant profile if we look at the average, and a decreasing profile if we look at its resolution, which is what is expected by a physical parameter that is constant through the measurement, so its expected value does not depend on the number of averages. With 40 average cycles, at saturation the iron film induces on the light polarization state a rotation amplitude of 0.33 mrad with 20 $\mu$rad as resolution. The order of magnitude we found is comparable with the Kerr rotation results presented in the subsection 4.1.5.

With the longitudinal MOKE setup (presented in section 4.1) based on a 635 nm laser, we calculated for the iron film a rotation of 0.88 mrad. The difference in amplitude in the results obtained from the two MOKE systems is related to a different wavelength response of the light and the angle of incidence of the light with the iron system. According to Judy *et al.* [35, 36], the change in the lasers angle of incidence and their wavelength can each introduce an attenuation of the Kerr rotation by a 10 nm Fe film by a factor 1.5. Indeed, if we take the Kerr rotation we measured with the red laser, and we divide it by $1.5^2$, we obtain $0.88/1.5^2 \approx 0.38$ rad, which is comparable with the 0.33 rad we evalued experimentally on the Fe film with the $\mu$MOKE system.

## Ru(2)/CoFeB(10) Hall bar in-plane characterizations

Devices systems, as a Hall bar and capacitor devices, are often studied in spintonics and microelectronic application to perform electrical measurements. Whenever, a magnetic characterization is required in a context in which a device system has to be electrically characterized, VSM or SQUID techniques cannot be used due to their sensibility to voltages and currents. Moreover, VSM and SQUID techniques are sensitive to the total magnetic moment of the sample, so they cannot be used to resolve micro devices (fabricated on the same sample) contributions. $\mu$MOKE systems, such as the one we have developed, offer a viable solution for analyzing and evaluating the magnetization of electrical devices, as they provide a high spatial resolution and are unaffected by the presence of voltages and currents.

In this subsection, we present the longitudinal $\mu$MOKE measurements on a magnetic Hall bar (sample MI in the table 6.1). The layout of the Hall bar microsystem is shown in the figure 6.13a. Hall bars are commonly used to measure the concentration of carriers in semiconductors. In spintronics, Hall bars are devices used to carry out resistive characterizations to measure the Hall effect, which can provide valuable information on the spin-dependent transport properties of materials [44].

The magnetic Hall bar region is defined by a 150 $\mu$m longitudinal channel with 10 $\mu$m width, intersected by three transverse channels of length 70 $\mu$m and width 3 $\mu$m as shown in the figure 6.13b. The nanofabrication methods for fabricating the device, shown in the figure 6.13, are reported further in the appendix B. In our analysis, we investigated the 10 nm thick CoFeB layer longitudinal channel magnetic response. The 10 $\mu$m longitudinal channel width sets the upper limit required laser beam diameter spot to distinguish between magnetic and non-magnetic regions. A spatial resolution lower than 10 $\mu$m could be reached with the 100x objective. The system scheme is shown in figure 6.14. Figure 6.14a is a picture of the sample taken from the camera. Thanks to the 100x objective, we can clearly see the Hall bar longitudinal channel and the laser spot with a diameter spot size of 5 $\mu$m. The corresponding scheme of the $yz$ Hall bar section is sketched in figure 6.14b. During the measurements, the longitudinal channel was oriented to be parallel to the direction of the magnetic field generated by the magnetic poles.

Analyzing 40 hysteresis loops, we realized that the presence of a low Kerr rotation signal and a significant Voigt quadratic background did not make it possible to resolve the hysteresis loop of the sample with a single measurement. The low Kerr rotation signal could be determined by the low response of the CoFeB magnetization to the green light. Only by averaging raw cycle measurements and then subtracting the Voigt background

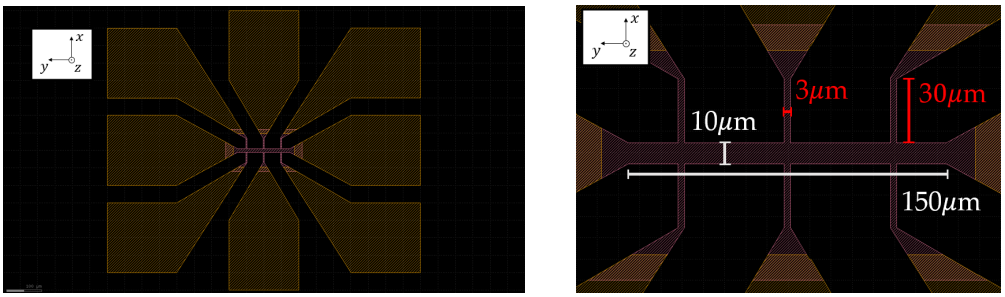


(a) (b)

Figure 6.13: (a) The HB sample Hall bar layout. (b) The HB sample Hall bar layout zoomed over the magnetic region.

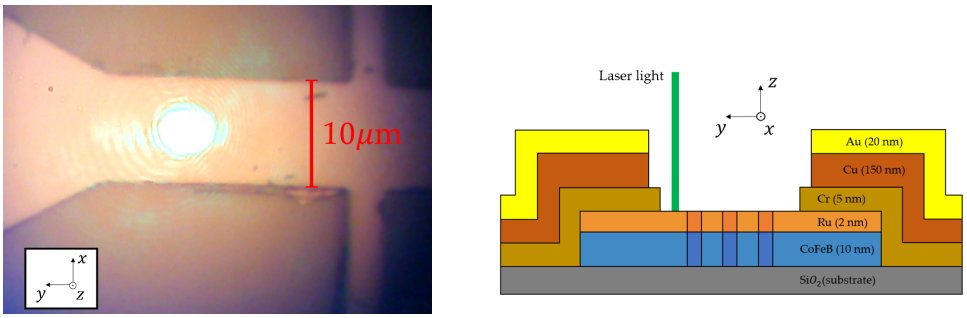


(a) (b)

Figure 6.14: (a) Picture of the sample and the green laser spot, with 5 $\mu$m diameter, taken with the camera. (b) 2D $yz$ section scheme of the structure, not in scale, corresponding to (a) with green laser ray.

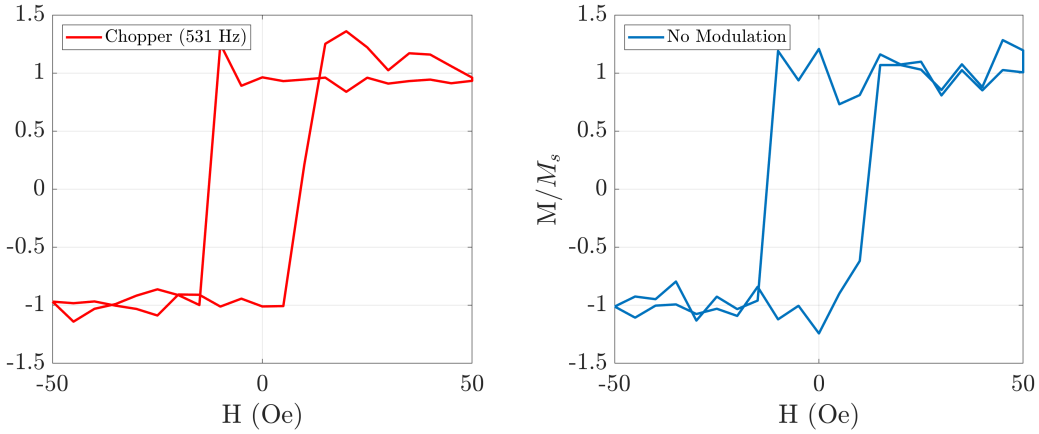


(a) Chopper (531 Hz) (b) No modulation

Figure 6.15: Longitudinal $\mu$MOKE normalized measurements for a CoFeB Hall bar with (a) and without (b) chopper modulation, obtained by averaging 40 single cycles.

| Modulation | $H_c$ [Oe] | SNR | $\theta_K$ [$\mu$rad] | $\Delta\theta_k$ [$\mu$rad] |
|---|---|---|---|---|
| **No** | 11.3 | 11 | 27 | 4 |
| **Chopper** | 12 | 17 | 23 | 3 |

Table 6.3: 10 nm CoFeB Hall bar longitudinal $\mu$MOKE magnetic parameters.

contribution, it was possible to resolve the magnetic signal of the sample. The results of the signal analysis for the two signal acquisition approaches are presented in the figures 6.15a and 6.15b. The 10 nm CoFeB magnetic parameters calculated from the signals in the plots 6.15 are presented in the table 6.3.

### 6.3.2. Polar $\mu$MOKE characterizations

#### Co/HZO out-of-plane film characterizations

In this subsection, we present the polar $\mu$MOKE measurements on the sample FO (see table 6.1). Measurements were done with a 100x objective set in a polar configuration. As shown in the figure 6.4, it is possible to obtain a polar geometry when the laser light and the lens axes are collinear.

We analyzed 40 hysteresis loop cycles, acquired with both modulated and unmodulated configurations, as discussed at the beginning of the subsection 6.3.1. The data exhibited Faraday linear background contributions attributed to the front position of the objective lens regarding the polar pole surface, as discussed in section 6.1. The figure 6.16 compares the differences between a single raw loop measurement before and after the Faraday linear background subtraction. The SNR parameter calculated for each single hysteresis scan signals, after the linear background subtraction, with and without a modulation stage, is presented in the figure 6.17a. As expected, the SNR parameters present a constant profile for both the modulation and unmodulated configurations. We obtain:

- SNR = 13.3 $\pm$ 1.4 with modulation;
- SNR = 4.2 $\pm$ 1.2 without modulation.

These results tell us that with the chopper it is possible to measure single loops with a better quality, because of a better noise rejection via modulation. Then, we present the analyses on the SNR when we average the single hysteresis loops, already cleaned from the Faraday linear background. Figure 6.18 show the magnetic and rotation hysteresis we obtained by averaging the single raw loop cycles, after having subtracted from each their

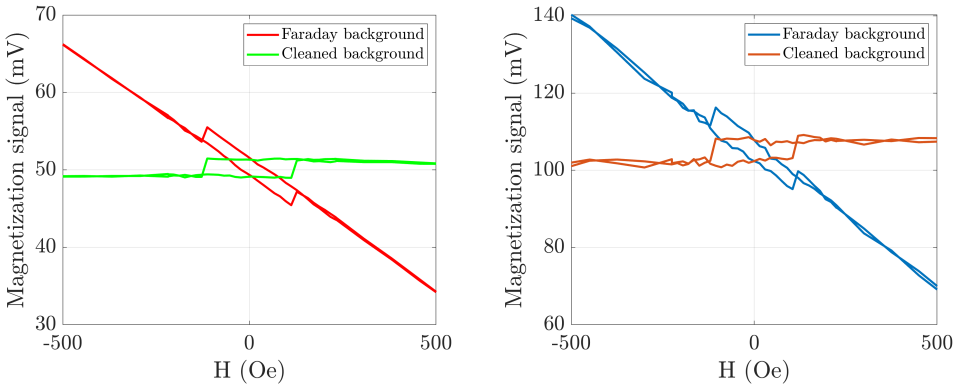


(a) Chopper (531 Hz). (b) No modulation.

Figure 6.16: Polar raw single measurement data with Faraday linear background measured with (a) and without (b) chopper modulation stage.

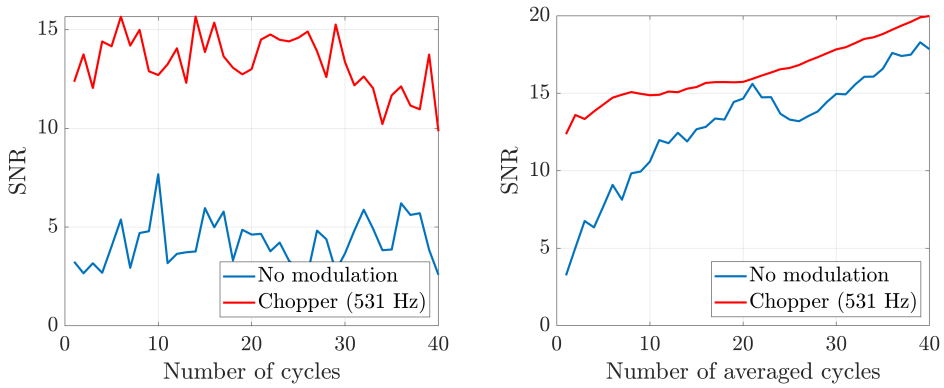


(a) (b)

Figure 6.17: SNR parameter for the Co film single signals (a) and averaged loops (b) as a function of the number of the averages.

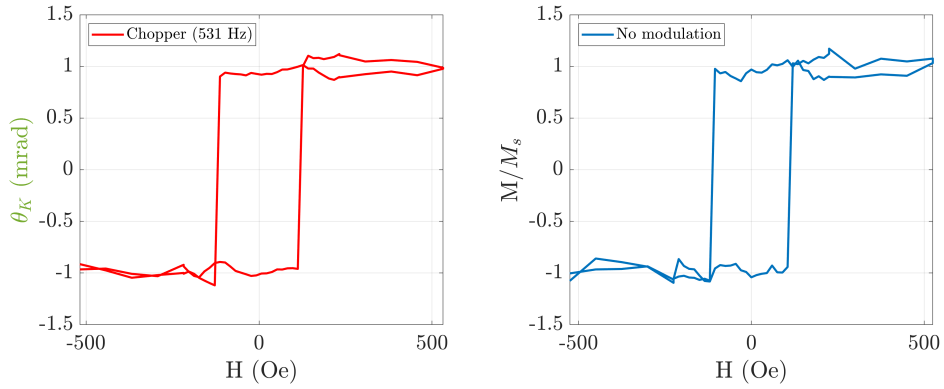


(a) Chopper (531 Hz) (b) No modulation

Figure 6.18: Polar $\mu$MOKE normalized measurements for the sample FO with (a) and without (b) chopper modulation, obtained by averaging 40 single cycles.

| | IP | | OOP | |
|---|---|---|---|---|
| *Signal* | **Chopper** | **No mod** | **Chopper** | **No mod** |
| Single | $10 \pm 0.7$ | $11 \pm 2$ | $13.3 \pm 1.4$ | $4.2 \pm 1.2$ |
| Average | 27 | 25 | 20 | 18 |

Figure 6.19: SNR parameter comparisons between the longitudinal and polar thin film measurements for single/averaged signals with and without modulation.

| **Modulation** | $H_c$ [Oe] | SNR | $\theta_K$ [mrad] | $\Delta\theta_k$ [mrad] |
|---|---|---|---|---|
| **No** | 111.8 | 18 | 0.59 | 0.047 |
| **Chopper** | 113.1 | 20 | 0.52 | 0.050 |

Table 6.4: 1 nm thick Co polar $\mu$MOKE magnetic parameters.

own Faraday contribution. The openings of the loops can be attributable to a Faraday background, which could not be eliminated by subtracting the linear fit.

The 1 nm Co thin film magnetic parameters calculated from the signals in the plots 6.18 are presented in the table 6.4. We found:

- $H_c = 113.1$ Oe $\pm$ 2 with modulation;
- $H_c = 111.8$ Oe $\pm$ 2 without modulation.

These results changes by about 10 Oe compared to the coercive field evaluated for the same sample C1 via VSM, as shown in the table 5.2. We consider this difference of 10 Oe in the measured fields is reasonable due to:

- the change in the VSM and polar pole sensibilities and calibrations;
- the polar magnetic pole used in this setup may not be uniform, unlike that of the VSM (as discussed in the section 4.2).

As shown in the table 6.19, the SNR parameter for the polar signals, regarding the values found for the Fe film, is:

- higher for single scans obtained via chopper;
- smaller for single scans obtained without modulation;
- lower after averaging 40 loops with and without modulation.

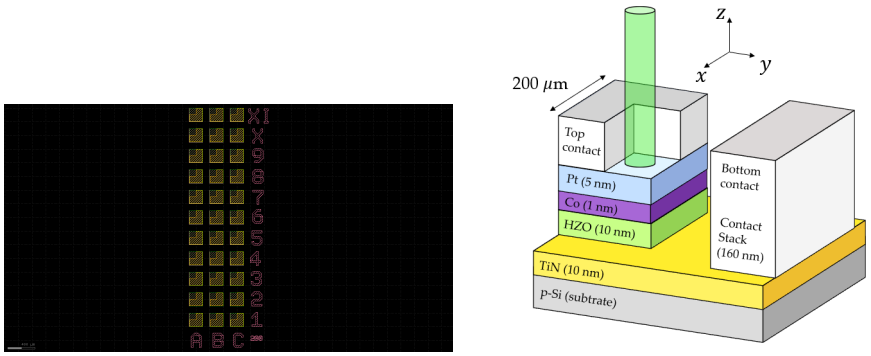


(a) (b)

Figure 6.20: (a) Microcapacitors layouts (b) 3D microcapacitor representation scheme, not in scale, with the laser pointing on the magnetic region provided by PMA.

## Co/HZO out-of-plane capacitors characterizations

In this subsection, we show the spatial $\mu$MOKE system capabilities to carry out a spatial characterization of various microcapacitors by exploiting the focusing of the objective and the acquisition of images via the camera.

The polar magnetic characterizations made both via VSM and the spatial $\mu$MOKE on the sample FO confirmed the presence of PMA in the cobalt layer. The next step was to create a microsystem device on this multilayer sample to study its magnetic properties. To prepare ourselves to study the HZO layer ferroelectric properties and magneto-electric coupling effects between the HZO electric polarization and the Co magnetization at their interface, we decided to realize micro capacitors devices (sample MO in the table 6.1). The layout of the micro capacitors and the 3D representation scheme are shown in the figure 6.20. The multilayer stack is the same as the sample FO. Each capacitor has a 200 $\times$ 200 $\mu$m base section and 160 $\mu$m height, and it is connected to the other capacitors by the common TiN back contact base. On top of each capacitor, a 200 x 200 $\mu$m contact made of Ti(10 nm), Au(50 nm) and Al(100 nm) was deposited to give the possibility to connect the capacitor to external electrical circuits. A 100 $\times$ 100 $\mu$m squared lateral hole on the top contact layer was done to allow the laser to point normally on the magnetic region provided by PMA. The capacitors are electrically connected to a parallelepiped Ti/Au/Al bottom contact to allow electrical measurements. Further details on the nanofabrication methods for fabricating the microcapacitor devices, shown in the figure 6.20, are explored in the appendix B.

The 100 x 100 $\mu$m squared lateral hole size sets the maximum required laser beam diameter spot to distinguish between magnetic and non-magnetic regions. Since the maximum

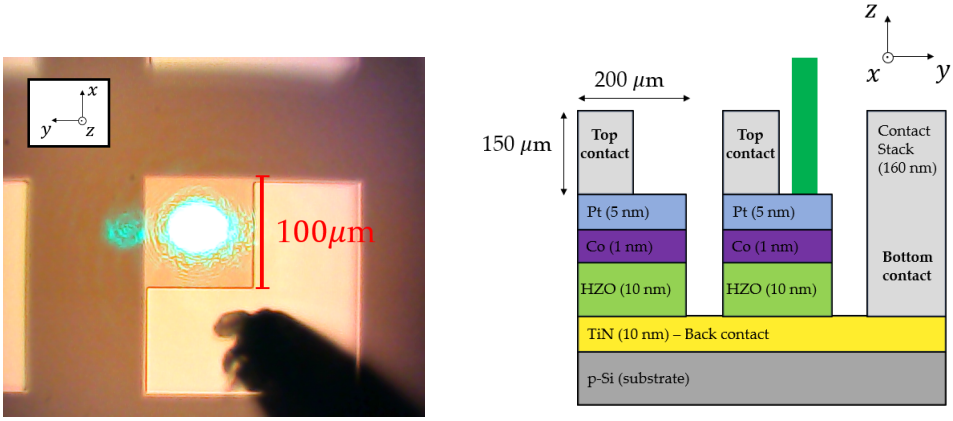


(a) (b)

Figure 6.21: (a) Picture of the sample and the green laser spot, pointed on the magnetic region, with 50 $\mu$m diameter, taken with the camera. (b) 2D $yz$ section scheme of the structure, not in scale, corresponding to (a) with green laser ray.

| **Capacitor** | 2B | 2C | 3B | 3C | 4B | 4C | 5B | 5C |
|---|---|---|---|---|---|---|---|---|
| SNR | 37 | 33 | 22 | 31 | 17 | 20 | 28 | 25 |

Table 6.5: SNR parameters for the Co/HZO capacitors obtained by averaging 5 single loops.

required laser spot size would be 100 $\mu$m, magnetic characterizations can be done with a 10x objective lens, which allows reaching a spatial resolution of 50 $\mu$m. The configuration of measurement is shown in figure 6.21. Figure 6.21a is a picture of the sample taken from the camera. Thanks to the 10x objective, we can clearly see the microcapacitor and the laser spot with a diameter size of 50 $\mu$m. The analysis done on the sample FO has confirmed us that the balanced detector can measure signals without light modulation, which quality does not differ significantly regarding the signals obtained via chopper. In the future, we will be interested in studying the magnetic properties of the capacitor, when a modulated gate voltage is applied. The use of the lock-in amplifier dedicated to demodulate the voltage signal won't allow the modulation of the light signal. For this reason, the next $\mu$MOKE characterizations will be done by exploiting the differential system of the balanced photodiode measuring without any modulation stage.

By referring to the layout scheme in figure 6.22a, we characterize the eight capacitors underlined in red square close line. For each capacitor, we took five measurements scans because their SNR ratio could be comparable or higher than the SNR values we obtained

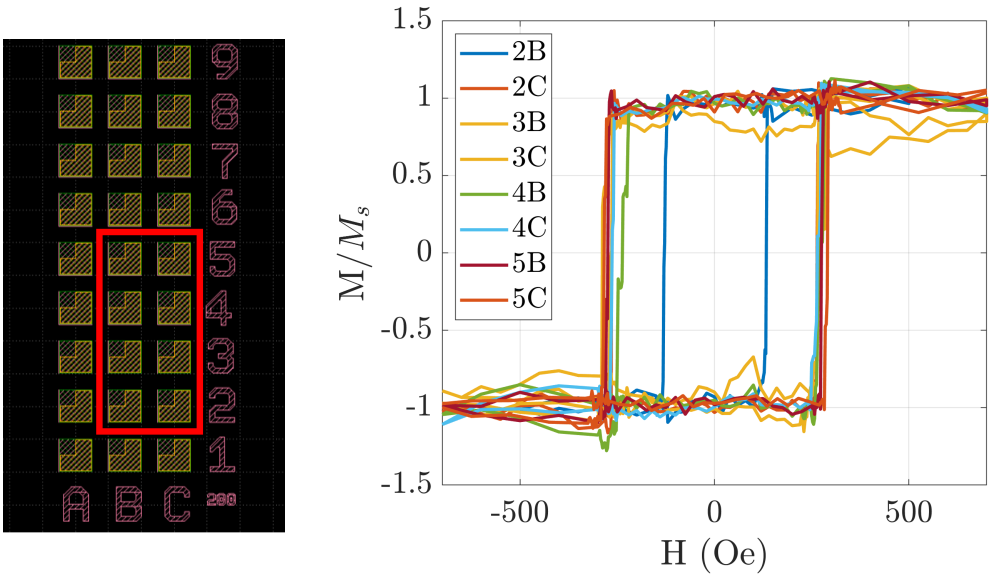


(a) (b)

Figure 6.22: HZO/Co microcapacitors magnetic response (a). Micro capacitors studied shown on the sample layout (b).

with the Fe thin, as shown by the table 6.5. The figure 6.22b show the microcapacitors averaged hysteresis loops. The coercive fields $H_c$ and their standard deviations for each of the capacitors are displayed in the table 6.6. Excluding the results of capacitor 2B, which showed anomalous behavior due to a fabrication defect, the capacitors present a coercive field distribution with an average $H_c = 252$ Oe and standard deviation equal to 50 Oe attributable to the nanofabrication process. Overall, the fabrication processes have induced an increase in the magnetic coercivity by 140 Oe, regarding the $H_c = 111.8$ Oe for the 1 nm Co thin film presented in the table 6.4, because of the shrinking of the magnetic system size. Moreover, some microcapacitors, as the 3C and 4B turrets, would present an asymmetric magnetization switching, which could be related to second order effect related to the dynamics of the domains.

### 6.3.3. Conclusions

To sum up, the setup characterizations showed us the following capabilities and the potentialities of our spatial $\mu$MOKE system:

- **High magnetic sensitivity**: all the different magnetic characterizations made clear, that without light modulation, the balanced photodiode can measure signals which quality does not differ significantly regarding the signals acquired via chopper, as shown in the tables 6.7 and 6.19. In fact, we were able to carry on magnetic

| **Capacitor** | 2B | 2C | 3B | 3C | 4B | 4C | 5B | 5C |
|---|---|---|---|---|---|---|---|---|
| $H_c^+$ [Oe] | 133.7 | 264 | 265.3 | 272.2 | 268.3 | 264.4 | 275.3 | 290.6 |
| $\Delta H_c^+$ [Oe] | 0.6 | 0.8 | 0.4 | 8 | 7 | 4.7 | 0.9 | 0.5 |
| $H_c^-$ [Oe] | -128.6 | -264 | -265.2 | -288.1 | -236.5 | -263.1 | -274.8 | -283.6 |
| $\Delta H_c^-$ [Oe] | 1.9 | 0.6 | 2.8 | 1 | 9 | 2.2 | 1.8 | 2 |

Table 6.6: Microcapacitors positive and negative coercive field amplitudes $H_c^{\pm}$ and standard deviations $\Delta H_c^{\pm}$.

characterizations both on thin film and micro systems with a cobalt magnetic layer which thickness was below the nanometer, even without modulation. The advantage of being able to measure without modulation allows expanding the setup capacity to carry out more experiments and investigations that would require multiple signal modulations, which are frequent in spintronics applications and experiments;

- **High spatial resolution**: The use of objective lenses allows us to increase the resolution of the system. We were able to present two study cases that required different spatial resolutions ranging from 100 $\mu$m to 10 $\mu$m, as we did with the CoFeB Hall bar and Co microcapacitors;
- **Magnetic characterizations versability**: by shifting the objective lens axis off-center regarding the laser beam, we were able to switch from polar MOKE to longitudinal MOKE geometry, increasing the flexibility of the $\mu$MOKE system to characterize magnetic systems with different magnetic configurations.

An issue that we had to face with was the presence of spurious magneto-optical effects, such the Voigt and the Faraday effects. The difficulty in processing and subtracting such background contributions from raw magnetic measurements can be an important source of noise for our signals. As future prospects for improving the quality of measured signals, it will be essential to focus on the reduction of such background effects, by:

- working with objectives which Voigt and Faraday responses is lower;
- working with longer focal distance lenses, compatibly with the required spatial resolution, to reduce interactions between the objective lens and the line fields generated by the magnets;
- working with magnetic poles which able to generate fields concentrated between the poles and with fewer lines on the objective.

| **Sample** | SNR Chopper | SNR without modulation |
|---|---|---|
| FI | 25 | 27 |
| MI | 12 | 11 |
| FO | 20 | 18 |
| MO | - | 37 |

Table 6.7: SNR parameter for the average signals obtained in the longitudinal and polar magnetic configurations in the case of thin films and devices.

In the chapter 7, we will use this spatial-micro MOKE setup to systematically study the magneto-electric coupling effects in the HZO/Co microcapacitors system we mentioned before.

# 7 | Co/HZO microcapacitors characterizations

In this chapter, we present the ferroelectric characterizations and the magnetoelectic measurements for the HZO capacitors introduced in chapter 6.

## 7.1. HZO ferroelectric characterizations

The reasons we studied ferroelectricity on a micro capacitor system, rather than a system of thin films (like sample C1 in the table 5.1), are:

- because we are interested in studying the magnetoelectric coupling effects in functional devices, e.g., for memory application;
- the grain boundary defects, present even in epitaxial ferroelectric HZO films, cause the formation of a non-negligible density of conductive filaments, which could prevent the system to show ferroelectric switching [72].

Electrical characterizations were done by a ferroelectric probe station (*TF Analyzer 2000E*), set in the measurement configuration shown in the figure 7.1. Measurements were done working in a top-bottom configuration, in which a driven probe is placed on the capacitor top contact, whereas a grounded probe is placed on the bottom contact.

### 7.1.1. Characterization results

The I-V curve of a 200 $\times$ 200 $\mu m^2$ Co/HZO capacitor is shown in the figure 7.2a. Integrating in time, the I-V FE curve obtained, after the HZO ferroelectric training (see subsection 4.3.1), by PUND technique (see subsection 4.3.2) in time, we calculate the polarization is depicted in figure 7.2b. We obtain:

- a saturation polarization of 0.384 $\pm$ 0.002 $\mu C/cm^2$;
- a remanent polarization of 0.374 $\pm$ 0.002 $\mu C/cm^2$;

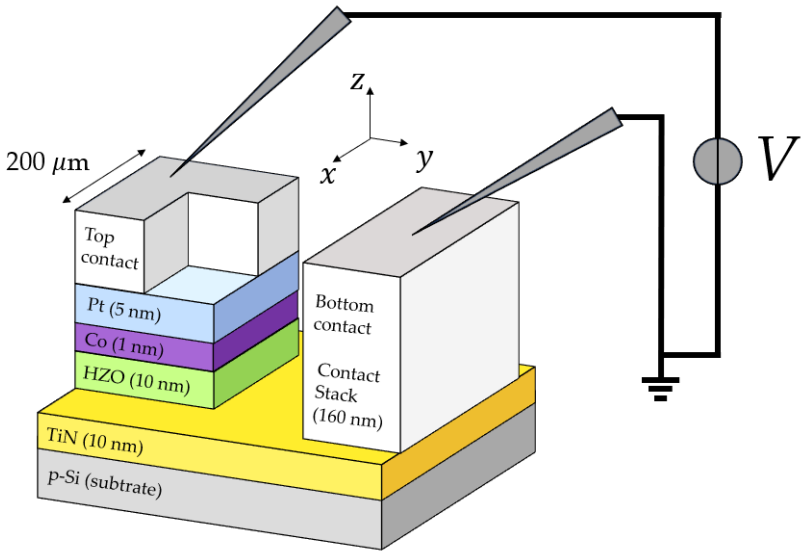


Figure 7.1: 3D scheme of the capacitor structure and bottom contact connected electrically with the probe station

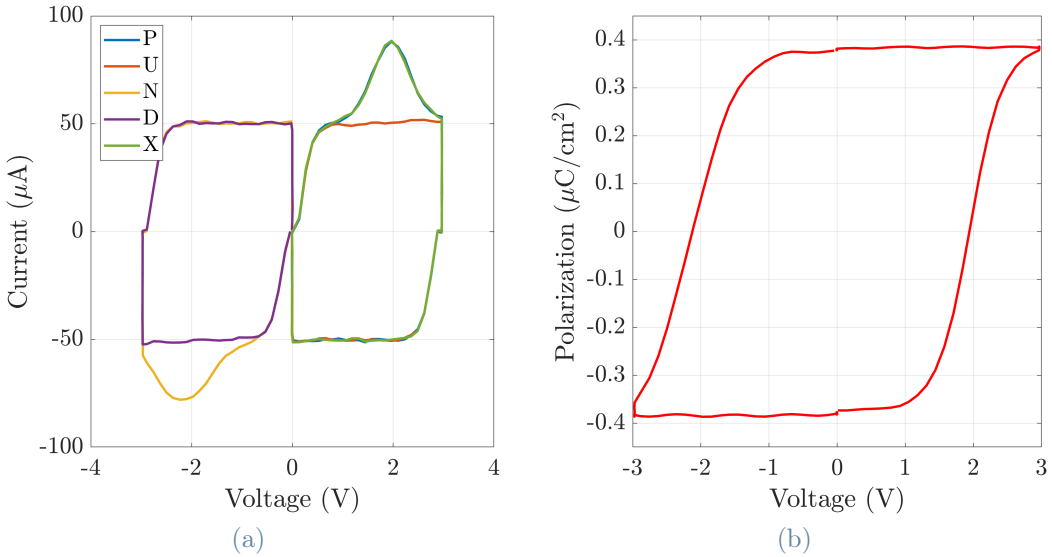


Figure 7.2: HZO/Co capacitor ferroelectric characterization of a sample. (a) I–V plot and (b) P–V plot.

- a coercive field of 2V.

Those values are lower than those found in the literature, e.g., a remanent polarization of 16 $\mu C/cm^2$ of a 10 nm thick HZO capacitor pillar with a 300 $\mu$m diameter [14]. The smaller polarization we measure might be due to several factors, e.g., the presence of defect that might create conductive paths, reducing the polarization. Furthermore, the hysteresis loop closes at the maximum field we set, so we cannot be sure that saturation is really achieved, or we are measuring a minor loop. Overall, the data confirm the ferroelectricity of the HZO microcapacitors and justify us to proceed with the magnetoelectric measurements. The ferroelectricity of HZO is though a critical parameter for the ME coupling, and must be improved in the future.

## 7.2. Magnetoelectrical measurements

In this section, we investigate the presence of magneto-electric (ME) coupling phenomena in the Co/HZO capacitors with PMA, magnetically characterized before the ferroelectric training in the section 6.3, because ME coupling and the PMA are interface phenomena.

To realize the magneto-electrical measurements, we integrated the ferroelectric probe station into the $\mu$MOKE system to control the HZO polarization state in real time. To allow for the probe landing on the capacitors and the $\mu$MOKE system to point the laser on the device to create a magnified image via the camera, we mounted a 10x objective with a long focal distance, the same used in the section 6.3. The sample holder has been modified to allow both the magnetic sample and the probes to be mounted on it, to guarantee both a rigid body motion during the laser pointing procedure. The $\mu$MOKE setup region around the sample holder, with the probes systems and the 10x objective lens, is shown in the figure 7.4.

Electrical measurements were done in a top-bottom configuration, as shown in figure 7.3. As for the polar $\mu$MOKE characterizations in the section 6.3, magneto-optical measurements were done without modulating the laser light.

### 7.2.1. Results and discussion

In this subsection, we present the study on the magneto-electric coupling effects induced in the cobalt layer by a remanence polarized HZO layer. We investigated the ME coupling in a Co/HZO capacitor by comparing the polar $\mu$MOKE hysteresis loop measurements taken:

- before the HZO ferroelectricity improvement through a ferroelectric training (see

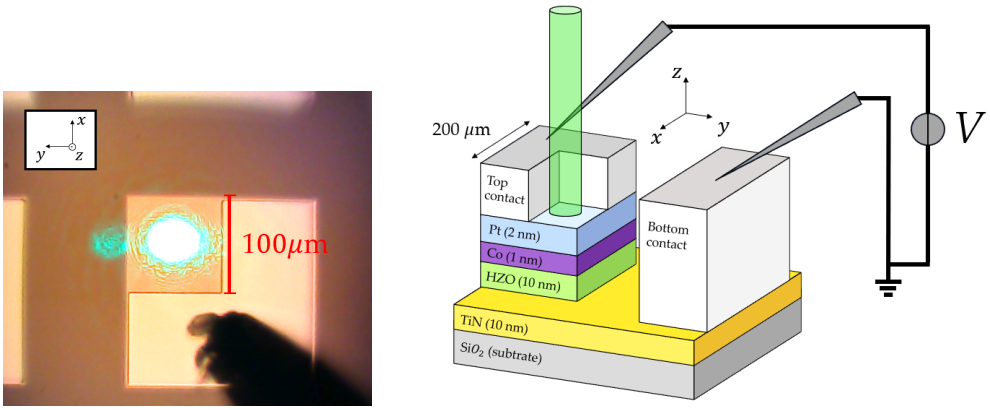


(a) (b)

Figure 7.3: (a) Picture of the capacitor sample with the probe on the top contact layer and the 50 $\mu$m green laser spot. (b) 3D scheme of the capacitor structure and bottom contact connected electrically with the probes system and the laser light pointing at the magnetic region showing PMA.

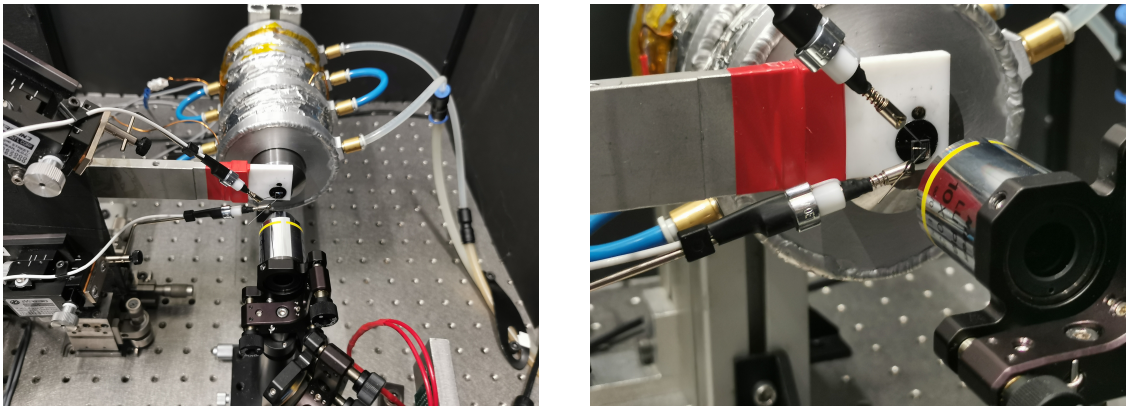

(a) (b)

Figure 7.4: $\mu$MOKE setup region around the sample holder with the probes systems and the 10x objective.

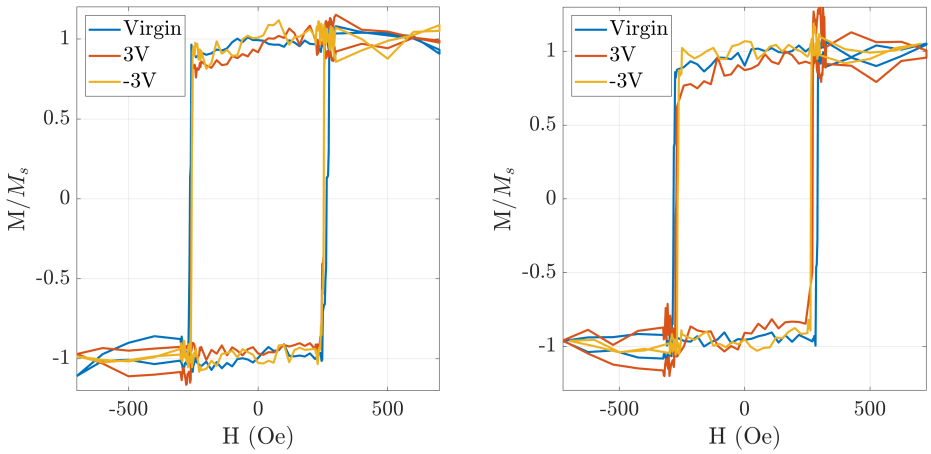


(a) 4C capacitor (b) 5C capacitor

Figure 7.5: Polar $\mu$MOKE hysteresis loop measurements taken for the capacitor 4C and 5C in their virgin state, before the HZO layer waking-up and training, and after a PUND measurement at -3V and 3V.

subsection 4.3.1), which we call virgin state;

- after a PUND measurement (once the HZO training is done) to set one of the two HZO remanence polarization state (see subsection 4.3.2).

Out of eight devices we measured, we will only show results for four, since the other half broke before giving any results. We attribute the main cause of device breakage to voltage breakdown effects, caused by leakage currents conducting through the HZO layer defects when a PUND measurement is done [21]. The two remanent polarizations were set by PUND measurements at -3V and 3V maximum because the analyses on PUND polarization measurements showed that HZO capacitors break more frequently at higher voltages.

We show the analysis done on the 3B, 3C, 4C and 5C capacitors, which were already presented in the section 6.3. In the figure 7.5, it is shown the comparison between then polar $\mu$MOKE hysteresis loop measurements, obtained from the average of five individual scans, for the 4C and 5C capacitors. Figure 7.6 depicts the positive and negative coercive fields, together with their standard deviations, calculated from the averaged hysteresis loops as a function of the polarization remanence of the HZO layer for capacitors 3B, 3C, 4C and 5C. Standard deviation bars were estimated from the distributions of positive and negative coercive fields of single cycle measurements. The standard deviations we found could be related to a magnetic domain dynamics. Coercive fields plotted for a remanence polarization $P_r$ equal to zero are referred to the capacitors virgin states' hysteresis loop

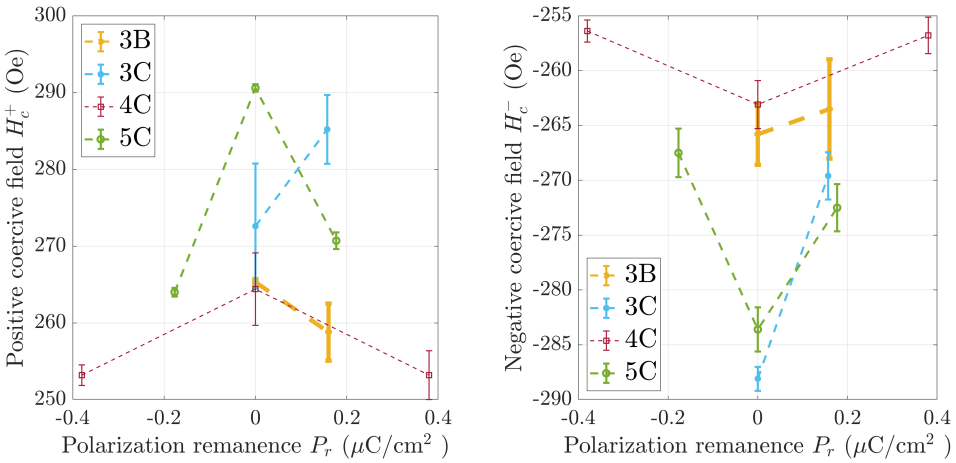


Figure 7.6: Positive and negative coercive fields, with standard deviation bars, as a function of the HZO layer polarization remanence in the 3B, 3C, 4C and 5C capacitors.

measurements. The 3B and 3C capacitors coercive fields data at negative remanence are not shown because, after performing the PUND measurements at -3V, the devices were broken. Figure 7.6 shows that the PUND meausurements did not induce a uniform negative and positive polarization measurements on the different capacitors. The non uniformity of the remanence polarizations could be inferred to:

- the nanofabrication process;
- we may not have reached saturation through the PUND measurements as shown in the figure 7.2b, which could represent a minor loop response.

Still, it is possible to recognize a change in the cobalt coercive fields. The data whose coercive fields show a difference larger than their standard deviation tables are presented in the tables 7.1 and 7.2, where:

- $H_i^{\pm}$ is the capacitor positive/negative coercive field, with the HZO layer in the virgin ($i = v$), positive ($i = p$) and negative ($i = n$) remanence polarization states;
- $\Delta H_j^{\pm} = |H_v^{\pm} - H_j^{\pm}|$ is the absolute value of the difference of the positive/negative coercive fields between the HZO virgin and $j$-remanence polarization state, with $j = p, n$.

Among the measured capacitors, we consider the results relating to the 4C and 5C capacitors to be the most significant. Figure 7.7 shows that the presence of a HZO polarization remanence causes the hysteresis loop to narrow compared to the hysteresis loop of the virgin HZO state. In the case of capacitor 4C the effect produced by the remanence

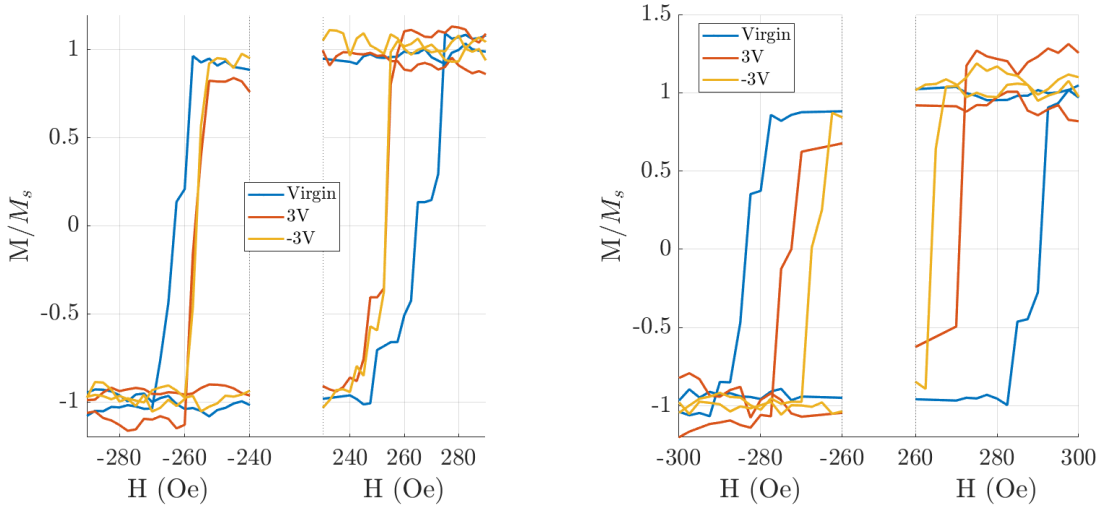


(a) 4C capacitor (b) 5C capacitor

Figure 7.7: Polar $\mu$MOKE hysteresis loop measurements taken for the capacitor 4C and 5C zoomed over the magnetic transition regions.

polarization is the same, while in the case of capacitor 5C an asymmetric tuning of $H_c$ occurs.

The data in the tables 7.1, 7.2 and the figure 7.6 show that the HZO polarization remanences is causing variations of the coercive fields, if compared to that of the capacitor virgin states. Since these data are preliminary, a statistical analyses based on the study of more capacitor samples will be required in the future. Once it is done, the analyses could demonstrate that a coercive field dependence on the ferroelectric remanence polarization state is present.

| **Capacitor** | $H_v^+$ [Oe] | $H_p^+$ [Oe] | $H_n^+$ [Oe] | $\Delta H_p^+$ [Oe] | $\Delta H_n^+$ [Oe] |
|---|---|---|---|---|---|
| 3B | 265.3 | 258.8 | - | 6.5 | - |
| 4C | 264.4 | 253.2 | 253.2 | 11.2 | 11.2 |
| 5C | 290.6 | 270.7 | 264 | 19.9 | 26.6 |

Table 7.1: Positive magnetic coercive fields of hysteresis loops for 3B, 4C and 5C capacitors with the HZO layer in the virgin ($v$), positive ($p$) and negative ($n$) remanence polarization states.

| Capacitor | $H_v^-$ [Oe] | $H_p^-$ [Oe] | $H_n^-$ [Oe] | $\Delta H_p^-$ [Oe] | $\Delta H_n^-$ [Oe] |
|---|---|---|---|---|---|
| 3C | -288.1 | -269.6 | - | 18.5 | - |
| 4C | -263.1 | -256.8 | -256.4 | 6.3 | 6.7 |
| 5C | -283.6 | -272.5 | -267.5 | 11.1 | 16.1 |

Table 7.2: Negative magnetic coercive fields of hysteresis loops for 3C, 4C and 5C capacitors with the HZO layer in the virgin ($v$), positive ($p$) and negative ($n$) remanence polarization states.

### 7.2.2. Conclusions and perspectives

In this section, we presented a preliminary investigation on the magneto-electric coupling at the HZO/Co interface of our capacitors. The data suggest that the HZO polarization can affect the magnetic state of Co, thus suggesting the presence of a magnetoelectric coupling, resulting in the tuning of $H_c$. To verify this inference, in the future it will be necessary to proceed with statistical analyzes of a larger capacitor population.

Our preliminary studies and previous work results indicate that it will be crucial to improve the ferroelectric response of the HZO layer. Zhang *et al.* were able to obtain in a 10 nm thick HZO pillar capacitor systems remanence and saturation polarizations up to 15 and 30 $\mu$m/cm$^2$ [14], more than ten times the remanence polarizations we have been working with. The HZO ferroelectricity is a crucial parameter for the ME coupling, so maximizing the polarization state of HZO could lead to an enhancement of the magneto-electric coupling effects. The enhancement of HZO ferroelectricity can be achieved by optimizing the HZO ferroelectric training and investigating whether thermal annealing treatments can influence the reorganization of atoms and defects within the HZO layer, resulting in a further improvement of polarization amplitude [41].

# 8 | Conclusion

This thesis work involved the development, characterization, and optimization of a high-sensitivity $\mu$MOKE spatial sensing system. The system we have developed demonstrated great versatility to characterize systems with longitudinal and polar magnetic configurations. The focusing of the light allows achieving an ultimate spatial resolution of the system up to 5 $\mu$m regarding the size of the magnetic region, which has made it possible to study magnetic systems ranging from large area films to micrometric devices, which are of fundamental interest in the research fields related to magnetism, spintronics. Moreover, a key feature is represented by its high sensitivity to magnetic signals thanks to the use of the balanced photodiode based on a differential signal acquisition system. Indeed, we were able to measure longitudinal and polar configurations in both thin films and devices. Furthermore, we have demonstrated the ability of this system to carry out measurements both in the presence and in the absence of light intensity modulation, which in our experiments was via a chopper. In fact, we were able to measure the small magnetic signals coming from thin films and devices whose magnetic layer was a cobalt characterized by perpendicular magnetic anisotropy (PMA) with a thickness below the nanometer. This is an important result due to the consequences it entails. The $\mu$MOKE system can perform measurements with continuous light signals, allowing us to introduce a modulation stage if we are interested in the frequency response of the signal or a very small signal. This system, in its different longitudinal and polar measurement configurations for thin films and devices, presents performances in terms of SNR which can range from 12 to 25 with light intensity modulation, and from 11 to 37 without modulation.

This system was applied to the study of the magnetoelectric coupling effects between the magnetization and the electrical polarization of a composite multiferroic system based the HZO/Co herostructure, where cobalt, with a thickness below the nanometer, is characterized by perpendicular magnetic anisotropy (PMA). The relevance of this experiment resides in the application of magnetoelectric materials, which are very attractive nowadays, mostly in the field of non-volatile memory technology, as they could permit data to be written exploiting a voltage, instead than a current, avoiding the power consumption and heat dissipation issues of the writing process currently used in STT-MRAMs.

Although ferroelectric characterizations showed a low amplitude polarization in the HZO capacitors, preliminary results, based on statistics on 4 devices, suggest a cobalt coercive field modulation of 5 % induced by HZO remanence polarization. Further developments of this work will focus on the one hand on the analysis of a greater number of devices to accumulate greater statistics, and the optimization of the structure in order to increase the polarization at the interface, currently well below the expected value [14].

Overall, these measurements demonstrate the potentiality of the $\mu$MOKE space system that we have developed to characterize devices and magnetoelectric coupling phenomena. In the future, this high sensitivity $\mu$MOKE system could be used to investigate phenomena as thermal and electrical generation of spin currents, spin accumulation and spin-to-charge conversion experiments in microdevices systems which dimension goes down to the microscale [17, 56]. This $\mu$MOKE system can be considered a versatile and powerful tool to predict and study the spin properties of materials, fundamental for spintronics applications.

# Bibliography

[1] Ez9 vibrating sample magnetometer (vsm). URL `http://www.microsense.net/products-vsm-ez9.htm`.

[2] Advantages and disadvantages of photolithography. URL `https://www.platypustech.com/advantages-and-disadvantages-of-photolithography`.

[3] Effects of the initial stages of film growth on the magnetic anisotropy of obliquely-deposited cobalt thin films. *Journal of Magnetism and Magnetic Materials*, 154(2): 249–253, 1996. ISSN 0304-8853.

[4] Mechanism of polarization "wake-up" in ferroelectric hafnia-zirconia thin films. *Solid-State Electronics*, 208:108714, 2023. ISSN 0038-1101.

[5] A. Aharoni. *Introduction to the theory of ferromagnetism*. Oxford University Press, 2 edition, 2007. ISBN 9780198508090.

[6] P. K. Amiri and W. K. L. Voltage-controlled magnetic anisotropy in spintronic devices. *SPIN*, 02(03):1240002, 2012.

[7] P. K. Amiri, W. K. L., and J. G. Alzate. Low-power non-volatile spintronic memory: STT-RAM and beyond. *Journal of Physics D: Applied Physics*, 46(7):074003, 2013.

[8] T. Andre, S. M. Alam, D. Gogl, C. K. Subramanian, H. Lin, W. Meadows, X. Zhang, N. D. Rizzo, J. Janesky, D. Houssameddine, and J. M. Slaughter. St-mram fundamentals, challenges, and applications. In *Proceedings of the IEEE 2013 Custom Integrated Circuits Conference*, pages 1–8, 2013.

[9] J. S. Andrew, J. D. Starr, and M. A. Budi. Prospects for nanostructured multiferroic composite materials. *Scripta Materialia*, 74:38–43, 2014. ISSN 1359-6462.

[10] D. Apalkov, A. Khvalkovskiy, S. Watts, V. Nikitin, X. Tang, D. Lottis, K. Moon, X. Luo, E. Chen, A. Ong, A. Driskill-Smith, and M. Krounbi. Spin-transfer torque magnetic random access memory (stt-mram). *ACM Journal on Emerging Technologies in Computing Systems*, 9(13):1–35, 1997.

[11] E. Ascher, H. Rieder, H. Schmid, and H. Stössel. Some Properties of Ferromagnetoelectric Nickel-Iodine Boracite, $Ni_3B_7O_{13}I$. *Journal of Applied Physics*, 37(3): 1404–1405, 03 1966.

[12] M. N. Baibich, J. M. Broto, A. Fert, F. N. Van Dau, F. Petroff, P. Etienne, G. Creuzet, A. Friederich, and J. Chazelas. Giant Magnetoresistance of (001)Fe/(001)Cr Magnetic Superlattices. *Phys. Rev. Lett.*, 61:2472–2475, Nov 1988.

[13] L. Baldrati, C. Rinaldi, A. Manuzzi, M. Asa, L. Aballe, M. Foerster, N. Biškup, M. Varela, M. Cantoni, and R. Bertacco. Electrical Switching of Magnetization in the Artificial Multiferroic CoFeB/$BaTiO_3$. *Advanced Electronic Materials*, 2:1600085, 2016.

[14] Z. Bao, L. Chunlong, H. Peizhen, and H. Zongliang. Ferroelectric control of the perpendicular magnetic anisotropy in PtCoRu/$Hf_{0.5}Zr_{0.5}O_2$ heterostructure. *Applied Physics Letters*, 119(2):022405, 07 2021. ISSN 0003-6951.

[15] S. Blundell. *Magnetism in Condensed Matter*. Oxford University Press, 1 edition, 2001. ISBN 0198505914.

[16] M. Bohr. A 30 year retrospective on dennard's mosfet scaling paper. *IEEE Solid-State Circuits Society Newsletter*, 12(1):11–13, 2007.

[17] F. Bottegoni, C. Zucchetti, S. Dal Conte, J. Frigerio, E. Carpene, C. Vergnaud, M. Jamet, G. Isella, F. Ciccacci, G. Cerullo, and M. Finazzi. Spin-hall voltage over a large length scale in bulk germanium. *Phys. Rev. Lett.*, 118:167402, Apr 2017. doi: 10.1103/PhysRevLett.118.167402. URL `https://link.aps.org/doi/10.1103/PhysRevLett.118.167402`.

[18] W. F. Brown. *Micromagnetis*. Interscience Publishers, New York, 1963.

[19] S. A. Campbell. *The Science and Engineering of Microelectronic Fabrication. Oxford series in electrical engineering*. Oxford University Press, 1996.

[20] J. Cao, S. Shi, Y. Zhu, and J. Chen. An overview of ferroelectric hafnia and epitaxial growth. *physica status solidi (RRL) – Rapid Research Letters*, 15(5):2100025, 2021.

[21] R. Cao, B. Song, D. Shang, Y. Yang, Q. Luo, S. Wu, Y. Li, Y. Wang, H. Lv, Q. Liu, and M. Liu. Improvement of Endurance in HZO-Based Ferroelectric Capacitor Using Ru Electrode. *IEEE Electron Device Letters*, 40(11):1744–1747, 2019.

[22] R. Cao, B. Song, D. Shang, Y. Yang, Q. Luo, S. Wu, Y. Li, Y. Wang, H. Lv, Q. Liu, and M. Liu. Improvement of endurance in hzo-based ferroelectric capacitor

using ru electrode. *IEEE Electron Device Letters*, 40(11):1744–1747, 2019. doi: 10.1109/LED.2019.2944960.

[23] G. Catalan and J. F. Scott. Physics and applications of bismuth ferrite. *Advanced Materials*, 21(24):2463–2485, 2009.

[24] C.-H. Choi, Y.-K. Park, S.-H. Lee, and K.-H. Kim. Novel esd protection transistor including sige buried layer to reduce local temperature overheating. *IEEE Transactions on Electron Devices*, 43(3):479–489, 1996.

[25] C.-G. Duan, S. S. Jaswal, and E. Y. Tsymbal. Predicted Magnetoelectric Effect in Fe/$BaTiO_3$ Multilayers: Ferroelectric Control of Magnetism. *Phys. Rev. Lett.*, 97: 047201, 2006.

[26] C.-G. Duan, J. P. Velev, R. F. Sabirianov, W. N. Mei, S. S. Jaswal, and E. Y. Tsymbal. Tailoring magnetic anisotropy at the ferromagnetic/ferroelectric interface. *Applied Physics Letters*, 24, 2008.

[27] I. E. Dzyaloshinskiĭ. On the magneto-electrical effects in antiferromagnets. *Soviet physics, JETP*, 10:628–629, 1960.

[28] G. Fantner. A brief introduction to error analysis and propagation. Technical report, EPFL, 2013.

[29] M. Fiebig. Revival of the magnetoelectric effect. *Journal of Physics D: Applied Physics*, 38:123–152, 2005.

[30] S. Foner. Versatile and Sensitive Vibrating-Sample Magnetometer. *Review of Scientific Instruments*, 30(7):548–557, 07 1959.

[31] M. J. Freiser. A survey of magnetooptic effects. *IEEE Transactions on Magnetics*, 4, 1968.

[32] J.-M. Hu and C.-W. Nan. Opportunities and challenges for magnetoelectric devices. *APL Materials*, 7:080905, 2019.

[33] J. Hutchby, G. Bourianoff, V. Zhirnov, and J. Brewer. Extending the road beyond cmos. *IEEE Circuits and Devices Magazine*, 18(2):28–41, 2002. doi: 10.1109/101.994856.

[34] M. T. Johnson, P. J. H. Bloemen, F. J. A. den Broeder, and J. J. de Vries. Magnetic anisotropy in metallic multilayers. *Report on Progress in Physics*, 59:1409–1458, 1996.

[35] J. Judy. Variation of longitudinal kerr and faraday effects with angle of incidence in thin iron films. *IEEE Transactions on Magnetics*, 6(3):563–569, 1970.

[36] J. H. Judy, J. K. Alstad, Geoffrey, and J. R. Wiitala. Large longitudinal kerr rotations and figures of merit in thin iron films. *IEEE Transactions on magnetics*, 1968.

[37] J. H. Judy, J. K. Alstad, Geoffrey, and J. R. Wiitala. Large longitudinal kerr rotations and figures of merit in thin iron films. *IEEE Transactions on magnetics*, 1968.

[38] A. Kashir, S. Oh, and H. Hwang. Defect Engineering to Achieve Wake-up Free $HfO_2$-Based Ferroelectrics. *Advanced Engineering Materials*, 23(1):2000791.

[39] A. I. Khan, A. Keshavarzi, and S. Datta. The future of ferroelectric field-effect transistor technology. *Nat Electron*, 3:38–43, 2020. ISSN 588–597.

[40] S. J. Kim, J. Mohan, S. R. Summerfelt, and J. Kim. Ferroelectric $Hf_0.5Zr_0.5O_2$ Thin Films: A Review of Recent Advances. *JOM*, 71:246–255, 2018.

[41] T. Kim, J. Park, B.-H. Cheong, and S. Jeon. Effects of high pressure nitrogen annealing on ferroelectric $Hf_{0.5}Zr_{0.5}O_2$ films. *Applied Physics Letters*, 112(9):092906, 03 2018. ISSN 0003-6951.

[42] Z. Kugler, J.-P. Grote, V. Drewello, O. Schebaum, G. Reiss, and A. Thomas. Co/Pt multilayer-based magnetic tunnel junctions with perpendicular magnetic anisotropy. *Journal of Applied Physics*, 111(7):07C703, 02 2012.

[43] W. Liang, G. Ya, and M. Jing. Recent progress in multiferroic materials. *Science China Technological Sciences*, 58:2207–2209, 2009.

[44] J. Lindemuth. *Hall Effect Measurement Handbook*. Lake Shore Cryotronics.

[45] B. Lojek. *History of Semiconductor*. Springer, 2006.

[46] J. Ma, J. Hu, Z. Li, and C.-W. Nan. Recent progress in multiferroic magnetoelectric composites: from bulk to thin films. *Advanced Materials*, 23(9):1062–1087, 2011.

[47] Z. Ma, W. Zhu, G. Lin, Y. Liu, F. Jin, Y. Yang, T. Wu, X. Luo, Y. Sun, J. Chen, Y. Sun, C. Zhou, and Z. Sheng. Micro-MOKE with optical interference in the study of 2D Cr2Ge2Te6 nanoflake based magnetic heterostructures. *AIP Advances*, 9(12): 125116, 12 2019.

[48] S. Manipatruni, D. E. Nikonov, C.-C. Lin, T. A. Gosavi, H. Liu, B. Prasad, Y.-L. Huang, E. Bonturim, R. Ramesh, and I. A. Young. Scalable energy-efficient magnetoelectric spin-orbit logic. *Nature*, 565(7737):35–42, 2019.

[49] M. Martinelli. Lezioni sulla polarizzazione per il corso di "onde ed ottica". Technical report, Politecnico di Milano, 2010.

[50] C. Mencuccini and V. Silvestrini. *Fisica II*. Liguori Editore, 2010.

[51] I. M. Miron, K. Garello, G. Gaudin, P.-J. Zermatten, M. V. Costache, S. Auffret, S. Bandiera, B. Rodmacq, A. Schuhl, and P. Gambardella. Perpendicular switching of a single ferromagnetic layer induced by in-plane current injection. *Nature*, 476: 189–193, 1996.

[52] J. Mohapatra, M. Xing, J. Elkins, and J. P. Liu. Hard and semi-hard magnetic materials based on cobalt and cobalt alloys. *Journal of Alloys and Compounds*, 824: 153874, 2020. ISSN 0925-8388.

[53] J. S. Moodera, L. R. Kinder, T. M. Wong, and R. Meservey. Large magnetoresistance at room temperature in ferromagnetic thin film tunnel junctions. *Phys. Rev. Lett.*, 74:3273–3276, Apr 1995.

[54] G. E. Moore. Cramming more components onto integrated circuits, reprinted from electronics, volume 38, number 8, april 19, 1965, pp.114 ff. *IEEE Solid-State Circuits Society Newsletter*, 11(3):33–35, 2006.

[55] J. Muller, T. S. Boscke, U. Schroder, S. Mueller, D. Brauhaus, U. Bottger, L. Frey, and T. Mikolajick. Ferroelectricity in Simple Binary $ZrO_2$ and $HfO_2$. *Nano Letters*, 12, 2012.

[56] C. Murer. *Thermal and electrical generation of spin currents investigated by magneto-optics*. PhD thesis, ETH Zurich, 2020.

[57] D. E. Nikonov and I. A. Young. Overview of beyond-cmos devices and a uniform methodology for their benchmarking. *Proceedings of the IEEE*, 101(12):2498–2533, 2013.

[58] L. Néel. Anisotropie magnétique superficielle et surstructures d'orientation. *J. Phys. Radium*, 15:225–239, 1954.

[59] T. C. Oakberg. *Magneto-Optic Kerr effect - Application Note*. HINDS Instruments.

[60] I. I. Oleinik, E. Y. Tsymbal, and D. G. Pettifor. Structural and electronic properties of $Co/al_2o_3/Co$ magnetic tunnel junction from first principles. *Phys. Rev. B*, 62: 3952–3959, Aug 2000.

[61] K. Postava, J. Bobo, M. Ortega, B. Raquet, H. Jaffres, E. Snoeck, M. Goiran, A. Fert, J. Redoules, J. Pistora, and J. Ousset. Magneto-optical measurements of magnetiza-

tion reversal in nanometer scale sputtered Fe thin films. *Journal of Magnetism and Magnetic Materials*, 163, 1995.

[62] K. M. Rabe, C. H. Ahn, and J.-M. Triscone. *Modern Physics of Ferroelectrics: Essential Background*. Springer, 2007. ISBN 9783540345909.

[63] B. Rodmacq, A. Manchon, C. Ducruet, S. Auffret, and B. Dieny. Influence of thermal annealing on the perpendicular magnetic anisotropy of $Pt/Co/AlO_x$ trilayers. *Physics Review B*, 79, 2009.

[64] J. M. Rondinelli, M. Stengel, and N. A. Spaldin. Carrier-mediated magnetoelectricity in complex oxide heterostructures. *Nature Nanotechnology*, 3(1):46–50, 2007. ISSN 1748-3395.

[65] S. Sahoo, S. Polisetty, C.-G. Duan, S. Jaswal, E. Tsymbal, and C. Binek. Ferroelectric control of magnetism in $BaTiO_3/Fe$ heterostructures via interface strain coupling. *Physical Review B*, 76:092108, 2007.

[66] M. Sawicki, W. Stefanowicz, and A. Ney. Sensitive squid magnetometry for studying nanomagnetism. *Semiconductor Science and Technology*, 26(6):064006, apr 2011.

[67] J. F. Scott. Room-temperature multiferroic magnetoelectrics. *NPG Asia Materials*, 5(75).

[68] J. Slonczewski. Current-driven excitation of magnetic multilayers. *Journal of Magnetism and Magnetic Materials*, 159(1):L1–L7, 1996. ISSN 0304-8853.

[69] J. Smit. Magnetoresistance of ferromagnetic metals and alloys at low temperatures. *Physica*, 17(6):612–627, 1951.

[70] N. A. Spaldin and M. Fiebig. The Renaissance of Magnetoelectric Multiferroics. *Science*, 309(5733):391–392, 2005.

[71] N. A. Spaldin and R. Ramesh. Multiferroics: progress and prospects in thin films. *Nat Mater.*, 6(1):21–29, 2007.

[72] M. C. Sulzbach. *Resistive Switching in $Hf_{0.5}Zr_{0.5}O_2$ ferroelectric tunnel junction memristors*. PhD thesis, Institut de Ciència de Materials de Barcelona ICMAB-CSIC, 2021.

[73] Y. Taur, D. Buchanan, W. Chen, D. Frank, K. Ismail, S.-H. Lo, G. Sai-Halasz, R. Viswanathan, H.-J. Wann, S. Wind, and H.-S. Wong. Cmos scaling into the nanometer regime. *Proceedings of the IEEE*, 85(4):486–504, 1997.

[74] *LDC202C-Manual*. Thorlabs, .

[75] *LDM9T-Manual*. Thorlabs, .

[76] *PDB210A-Manual*. Thorlabs, .

[77] B. Tudu, K. Tian, and A. Tiwari. Effect of composition and thickness on the perpendicular magnetic anisotropy of (co/pd) multilayers. *Sensors*, 17(12), 2017. ISSN 1424-8220.

[78] C. A. F. Vaz. Electric field control of magnetism in multiferroic heterostructures. *Journal of Physics D: Applied Physics*, 24(33):333201, 2012.

[79] B. F. Vermeulen, F. Ciubotaru, M. I. Popovici, J. Swerts, S. Couet, I. P. Radu, A. Stancu, K. Temst, G. Groeseneken, C. Adelmann, and K. M. Martens. Ferroelectric Control of Magnetism in Ultrathin HfO2/Co/Pt Layers. *ACS Applied Materials & Interfaces*, 11(37):34385–34393, 2019.

[80] H. Vélez, J. Schaab, M. S. Wörnle, M. Müller, E. Gradauskaite, P. Welter, C. Gutgsell, C. L. D. Corneliu Nistor, M. Trassin, M. Fiebig, and P. Gambardella. High-speed domain wall racetracks in a magnetic insulator. *Nature comunications*, 10(1): 4750, 2019.

[81] K. F. Wang, J. M. Liu, and Z. F. Ren. Multiferroicity: the coupling between magnetic and polarization orders. *Advances in Physics*, 58:321–448, 2009.

[82] P. Warnicke. *Tailored properties of ferromagnetic thin films*. PhD thesis, Uppsala Universitet, 2008.

[83] W. Wei, X. Ma, J. Wu, F. Wang, X. Zhan, Y. Li, and J. Chen. Spontaneous polarization enhancement in ferroelectric Hf0.5Zr0.5O2 using atomic oxygen defects engineering: An ab initio study. *Applied Physics Letters*, 115(9):092905, 08 2019.

[84] H.-S. Whang, S.-J. Yun, J. Moon, and S.-B. Choe. Optical Measurement of Magnetic Anisotropy Field in Nanostructured ferromagnetic Thin Films. *Journal of Magnetics*, 20(1):8–10, 2015.

[85] H. X. Yang, M. Chshiev, B. Dieny, J. H. Lee, A. Manchon, and K. H. Shin. First-principles investigation of the very large perpendicular magnetic anisotropy at fe/mgo and co/mgo interfaces. *Physics Review B*, 84, 2011.

[86] C. You and S. Shin. Derivation of simplified analytic formulae for magneto-optical kerr effects. *Applied Physics Letters*, 69, 1968.

[87] F. Zavaliche, T. Zhao, H. Zheng, F. Straub, M. P. Cruz, P. L. Yang, D. Hao, and

R. Ramesh. Electrically assisted magnetic recording in multiferroic nanostructures. *Nano Letters*, 7:1586–1590, 2007.

# A | Kerr rotation evaluation for the $\mu$MOKE setup

In this appendix, we show the mathematical calculations from which we retrieved the relation (6.17) to directly evalue the Kerr rotation from a $\mu$MOKE signal.

By referring to the $\mu$MOKE setup scheme shown in figure A.1, assuming to have total intensity reflectivity and transmission equal to 1 respectively from the dicroic mirror $M_2$ and the objective lens $OL$, the light power $P_S$ entering the beam splitter $BS^2$ is described by the relation (A.1):

$$P_S = T_1 R_S R_1 P_0 \tag{A.1}$$

where $P_0$ is the laser intensity coming out of the polarizer $P$; $T_1$ and $R_1$ the intensity trasmittivity and reflectivity of the beam splitter $BS^1$; and $R_S$ is the intensity reflectivity of the magnetic sample S. $P_S$ is transmitted by $BS^2$ by a fraction $T_2$ to the photodiode $PD$, which generates the output voltage signal $V_{DC}$ (A.2):

$$V_{DC} = T_2 P_S r_L \Re_{PD}(\lambda) \tag{A.2}$$

where $r_L$ $[\Omega]$ and $\Re_{PD}(\lambda)$ $[A/W]$ are the load resistance and the photodiode responsivity. In the subsection 6.1.4, we found that the intensity $P_{BD}$ measured by the balanced photodiode $BD$ is given by (A.3):

$$P_{BD} = 2R_1 T_1 R_2 R_S P_0 \theta_K = 2P_S R_2 \theta_K \tag{A.3}$$

Then, the balanced photodiode $BD$ generates the voltage signal $V_{BD}$ (A.4):

$$V_{BD} = P_{BD} G \Re_{BD}(\lambda) = 2P_S R_2 G \Re_2(\lambda) \theta_K \tag{A.4}$$

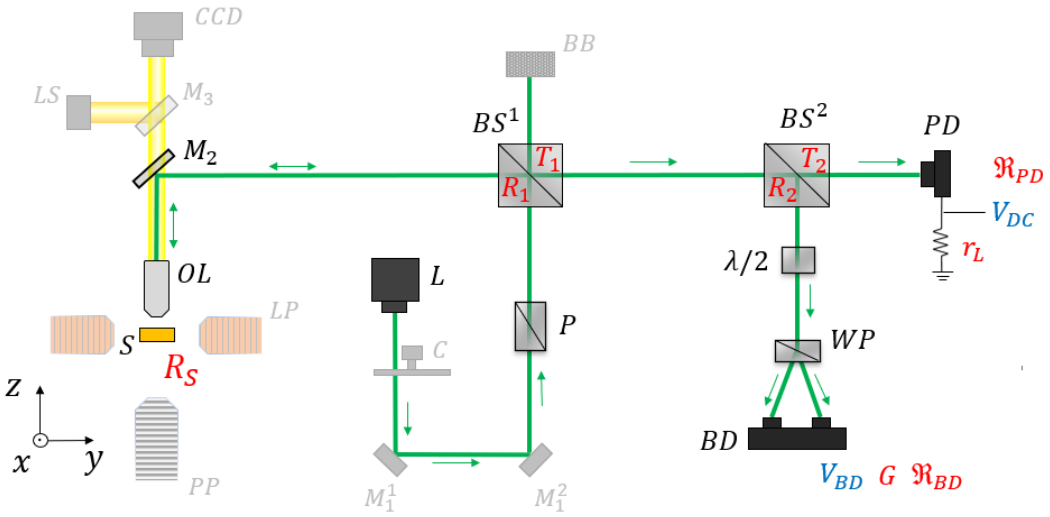


Figure A.1: Optical path and detection setup for the laser light in the $\mu$MOKE scheme.

where $\Re_{BD}(\lambda)$ $[A/W]$ is the balanced photodiode responsivity and $G$ $[V/A]$ balanced photodiode transimpedance gain. Finally, by combining the relations (A.2) and (A.4) is possible to retrieve the expression for the Kerr rotation $\theta_K$ (A.5):

$$\theta_K = \frac{\Re_{PD}(\lambda)}{\Re_{BD}(\lambda) \cdot G} \frac{T_2}{R_2} \frac{r_L}{2V_{DC}} V_{BD} \tag{A.5}$$

# B | Nanofabrication methods

In this appendix, we will go through the fundamental nanofabrication procedures involved to realize the Hall bar and microcapacitors devices presented in the chapter 6.

Nanofabrication is based on three fundamental steps:

- **Lithography**: the term lithography refers to a whole category of different processing used to transfer a desired pattern onto a substrate. The main characteristic all these processes share is the use of o a resist as a basis to pattern the layer and a development step to obtain the pattern. The resist is typically a polymeric or organic material which can be dissolved using an apposite developer.

  In general, a lithography process presents the following steps:

  1. the liquid resist is poured onto the substrate, then the sample is spinned to distribute the resist in a thin layer of few micrometers;
  2. the sample is heated to a fixed temperature to evaporate the resist solvent, leaving a uniform solid layer on the substrate:
  3. with an energy source such as light (in the UV range) or electrons, the solubility characteristic of the resist can be locally modified to obtain the spatial profile of the specific pattern;
  4. the resist is immersed in a specific developer, which causes the selective removal of the exposed resist, resulting in the transfer of the design onto the substrate.

  Optical lithography was the type of lithography used for the fabrication of the devices described in the chapter 6. Optical lithography is often used as:

  – it can create patterns with minimal features down to a few tens of nanometers, while also enabling incredibly precise control over feature geometry;
  – it is also comparatively fast, capable of creating patterns over an entire silicon wafer with relatively low cost;

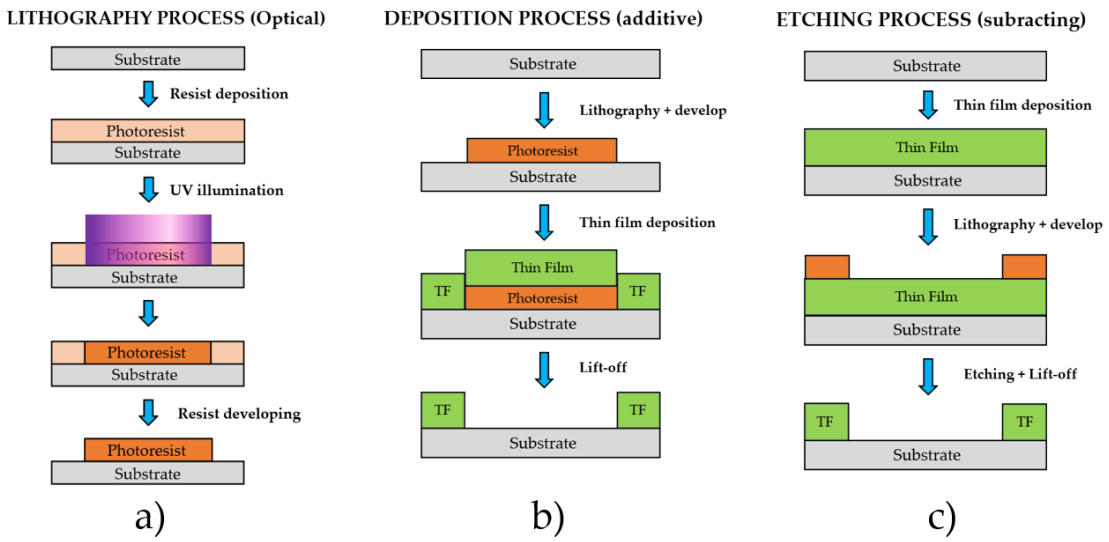


Figure B.1: The sketch (not in scale) of (a) optical lithography, (b) deposition process, (c) etching process for nanofabrication

  - is also versatile: it's commonly used to pattern various materials, including glass, silicon, and even flexible substrates [2].

  The maximum resolution of optical lithography is limited by the diffraction's wavelength of the light used to transfer the pattern. The conventional optical lithography based on UV light, such as the one performed in PoliFab, can reach a resolution of the order of 1 $\mu$m. The (optical) lithography procedure is shown in the figure B.1a.

- **Deposition**: a film of a given material is deposited on a substrate or underlayer. The most commonly used deposition techniques are:

  - *Sputtering*: a technique that involves the atomization of a target material and its subsequent deposition onto the sample. The technique is based on the use of high-energy electrons generated in a plasma which is directed towards the target material chosen for deposition [19];

  - *Evaporation*: this method exploits the melting or sublimation of various materials and the vapor pressure, leading to their deposition on the sample [19];

  Upon immersion in an organic solvent (usually acetone) it is possible to locally remove the remaining resist and the overlying deposition, thus leaving the desired pattern onto the substrate (lift-off). An example of lithography and deposition process is sketched in the figure B.1b.

- **Etching**: etching is a technique used to selectively remove material (or portion of it)

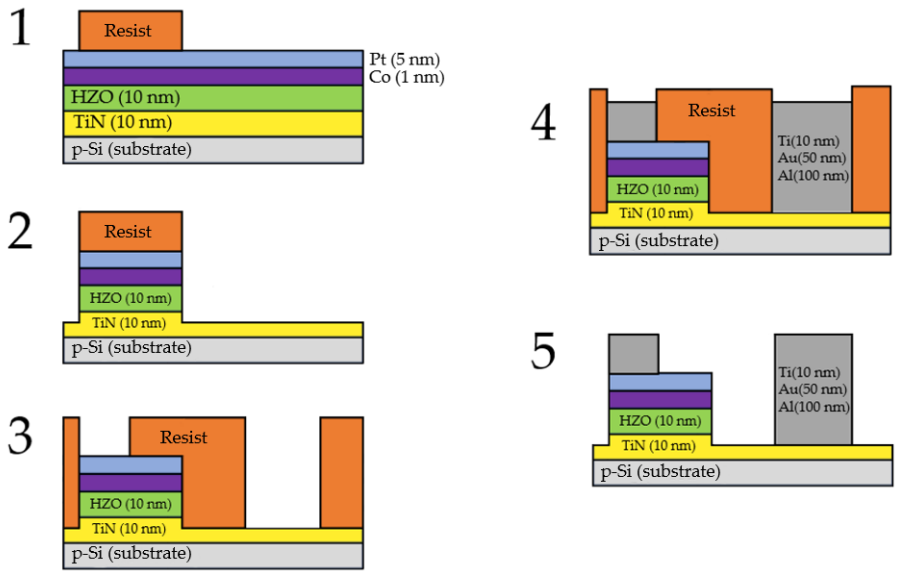


Figure B.2: Sketch (not in scale) of the nanofabrication steps to realize the capacitor devices

from the sample. When etching is done, the resist role is to act as a protective mask to allow the removal of the uncovered regions of the substrate. Upon immersion of the sample in an organic solvent (usually acetone) it is possible to remove the remaining resist that was not removed by the etching process (lift-off process). After resist removal, the desired pattern is left on the substrate. An example of lithography and etching process is sketched in the figure B.1c;

In the figure B.2, we sketched the nanofabrication steps required to fabricate the microcapacitors system. The p-Si/TiN(10)/HZO(10)/Co(1)/Pt(5) stack was provided by Fraunhofer Institute as part of a scientific collaboration. To realize the capacitor, we proceeded as follows:

1. we deposited a 200 $\times$ 200 $\mu$m resist mask;
2. to transfer the resist mask pattern to the material stack, we etched the sample, removing material down to the TiN layer in all regions apart from the square covered by resist. Then, the resist mask on top of the turret structure was removed with an organic solvent;
3. to prepare the sample for electrical contacts deposition, a new lithography step was done, leaving uncovered the sample regions in which the contact materials had to be deposited;
4. by *evaporation* technique, we proceed with contact material deposition made of:

- 100 nm of Al;
- 50 nm of Au;
- 10 nm of Ti.

5. to complete the microcapacitor device, the remaining resist was removed by immersing the sample in an acetone solution.

# Acknowledgements

I want to especially thank prof. Matteo Cantoni, Christian Rinaldi, Giovanni Gandini, Federico Fagiani and all the people working with me in PoliFab. I also thank my wonderful family who have stayed by my side in all these years.